Spatial Profiles in the Singular Solutions of the 3D Euler Equations and Simplified Models

Thesis by
Pengfei Liu

In Partial Fulfillment of the Requirements for the
degree of
Doctor of Philosophy

CALIFORNIA INSTITUTE OF TECHNOLOGY
Pasadena, California

2017
Defended August 22, 2016

Pengfei Liu
ORCID: 0000-0002-6714-7387

ACKNOWLEDGEMENTS

I would like to extend my deepest gratitude to my thesis adviser, Prof. Thomas Yizhao Hou, for his continuous support, guidance and encouragement. Prof. Hou introduced me to the field of mathematical fluid mechanics, and I have truly enjoyed my research in this fascinating area. Prof. Hou dedicates to work on hard and impactful research problems, which deeply influenced me and shaped my view of scientific research. I benefited tremendously from his deep mathematical insight and broad vision of science. Moreover, Prof. Hou also gives me a lot of help in my personal life, and I could not have imagined having a better mentor.

I also want to thank Profs. Oscar Bruno, Dan Meiron and Houman Owhadi for kindly serving in my thesis committee. I took Prof. Bruno's courses on PDE, and what I learned in that class prepared me for my research on fluid equations. I got several opportunities to talk with Prof. Owhadi on multi-scale analysis and uncertainty quantification, and benefited a lot from his expertise.

I feel honored to have had some stimulating discussions with many brilliant mathematicians, especially Prof. Tianling Jin from HKUST, Prof. Zhiwen Zhang from HKU, Prof. Yao Yao from GaTech, Prof. Kiselev from Rice University, Prof. Qin Li and Dr. Xiaoqian Xu from University of Wisconsin, Mr. Pengchuan Zhang and Dr. Maolin Ci from Caltech, and more. Their knowledge truly inspired me.

The Computing+Mathematical Sciences department at Caltech provides an extremely cozy environment for studying and research. I want to thank the CMS staff members, especially Carmen Sirois and Sydney Garstang, for their help.

I have been fortunate enough to make some very good friends, and without their help I would have never reached this point. I would like to thank their accompany and support, especially Ting Jiang, Chengdi Lai, Yong Huang, Yilin Mo, Niangjun Chen, Lingwen Gan, Qiong Zhang, Duo Han, Xiaoqi Ren, and more.

This thesis is dedicated to my parents, Mr. Zhengang Liu and Ms. Jinfang Xu for their endless love. My parents raised me under some difficult conditions, but they provided me the best education opportunity that they could afford, without which I could never be who I am today. I hope that my effort and achievement can make them feel proud from thousands of miles away. The inspiration that I drew from their courage when facing difficulties will keep leading me forward.

ABSTRACT

The partial differential equations (PDE) governing the motions of incompressible ideal fluid in three dimensional (3D) space are among the most fundamental non-linear PDEs in nature and have found a lot of important applications. Due to the presence of super-critical non-linearity, the fundamental question of global well-posedness still remains open and is generally viewed as one of the most outstanding open questions in mathematics. In this thesis, we investigate the potential finite-time singularity formation of the 3D Euler equations and simplified models by studying the self-similar spatial profiles in the potentially singular solutions.

In the first part, we study the self-similar singularity of two 1D models, the CKY model and the HL model, which approximate the dynamics of the 3D axisymmtric Euler equations on the solid boundary of a cylindrical domain. The two models are both numerically observed to develop self-similar singularity. We prove the existence of a discrete family of self-similar profiles for the CKY model, using a combination of analysis and computer-aided verification. Then we employ a dynamic rescaling formulation to numerically study the evolution of the spatial profiles for the two 1D models, and demonstrate the stability of the self-similar singularity. We also study a singularity scenario for the HL model with multi-scale feature.

In the second part, we study the self-similar singularity for the 3D axisymmetric Euler equations. We first prove the local existence of a family of analytic self-similar profiles using a modified Cauchy-Kowalevski majorization argument. Then we use the dynamic rescaling formulation to investigate two types of initial data with different leading order properties. The first initial data correspond to the singularity scenario reported by Luo and Hou. We demonstrate that the self-similar profiles enjoy certain stability, which confirms the finite-time singularity reported by Luo and Hou. For the second initial data, we show that the solutions develop singularity in a different manner from the first case, which is unknown previously. The spatial profiles in the solutions become singular themselves, which means that the solutions to the Euler equations develop singularity at multiple spatial scales.

In the third part, we propose a family of 3D models for the 3D axisymmetric Euler and Navier-Stokes equations by modifying the amplitude of the convection terms. The family of models share several regularity results with the original Euler and Navier-Stokes equations, and we study the potential finite-time singularity of the

models numerically. We show that for small convection, the solutions of the inviscid model develop self-similar singularity and the profiles behave like travelling waves. As we increase the amplitude of the velocity field, we find a critical value, after which the travelling wave self-similar singularity scenario disappears. Our numerical results reveal the potential stabilizing effect the convection terms.

TABLE OF CONTENTS

LIST OF ILLUSTRATIONS

LIST OF TABLES

Chapter 1

INTRODUCTION

1.1 The Regularity Problem for the 3D Euler and Navier-Stokes Equations

The grand open question

The study of fluid has a long history, and dates back to the works of Leonardo Da Vinci, who made an attempt at studying turbulence, Isaac Newton, who derived the formula for drag force, and Jean le Rond d'Alembert, who is famous for his paradox that drag force is zero in ideal fluid. The classical equations of fluid dynamics are among the most fundamental partial differential equations, which have found a lot of important applications but are still far from being fully understood.

The 3D incompressible Euler (inviscid) and Navier-Stokes (viscous) equations are the governing equations for the motions of incompressible ideal fluid in 3D space, and take the following simple form,

$$u_t + u \cdot \nabla u = -\nabla p + \nu \Delta u, \tag{1.1.1a}$$

$$\nabla \cdot u = 0, \tag{1.1.1b}$$

where

$$u(x,t) : R^3 \times [0,T) \to R^3$$

describes the velocity field of the fluid, and

$$p(x,t) : R^3 \times [0,T) \to R$$

is the pressure field in the fluid. The diffusion term

$$\nu \Delta u$$

models the viscosity, and is derived from the Stokes' stress constitutive equation

$$\nabla \cdot \tau, \quad \tau = 2\nu\varepsilon,$$

where

$$\varepsilon = \frac{1}{2}(\nabla u + \nabla u^T).$$

For $\nu = 0$, equations (1.1.1) are called the Euler equations (inviscid), and for $\nu > 0$, equations (1.1.1) are called the Navier-Stokes equations (viscous).

Equation (1.1.1a) is Newton's second law of motion applied to fluid. The divergence free condition (1.1.1b) guarantees the incompressibility of the fluid.

Note that we do not have an evolution equation for the pressure field $p(x,t)$ in (1.1.1). The pressure $p(x,t)$ can indeed be viewed as a Lagrange multiplier, and recovered based on the divergence free constraint (1.1.1b). Taking the divergence of equation (1.1.1a), one can get the following representation for the pressure $p(x,t)$,

$$p(x,t) = (-\Delta)^{-1}\partial_i\partial_j u_i u_j. \tag{1.1.2}$$

Equations (1.1.1) can also be written as

$$u_t = B(u,u) + \nu\Delta u, \tag{1.1.3}$$

where the nonlinear term $B(u,u)$ is defined as

$$B(u,u) = -u\cdot\nabla u - \nabla p = P(-u\cdot\nabla u). \tag{1.1.4}$$

Here P is the Leray projection operator onto divergence-free vector field,

$$Pu_i = u_i - \Delta^{-1}\partial_i\partial_j u_j.$$

The Euler equations enjoy the following scaling invariant property

$$u(x,t) \to \frac{\lambda}{\tau}u\left(\frac{x}{\lambda},\frac{t}{\tau}\right), \quad p(x,t) \to \frac{\lambda^2}{\tau^2}p\left(\frac{x}{\lambda},\frac{t}{\tau}\right). \tag{1.1.5}$$

And for the Navier-Stokes equations, we have the following scaling-invariance,

$$u(x,t) \to \tau^{-1/2}u\left(\frac{x}{\tau^{1/2}},\frac{t}{\tau}\right), \quad p(x,t) \to \tau^{-1}p\left(\frac{x}{\tau^{1/2}},\frac{t}{\tau}\right). \tag{1.1.6}$$

Note that the scaling transformations determine the two-parameter symmetry group in (1.1.5) for the Euler equations, and the introduction of viscosity $\nu > 0$ restricts this symmetry group to the one-parameter group given in (1.1.6) for Navier-Stokes.

Smooth solutions to (1.1.1) conserve the kinetic energy $\|u\|_{L^2(R^3)}$, and we have

$$\frac{1}{2}\|u(x,t)\|^2_{L^2(R^3)} + \nu\int_0^t \|\nabla u(x,s)\|^2_{L^2(R^3)} = \frac{1}{2}\|u(x,0)\|^2_{L^2(R^3)}. \tag{1.1.7}$$

The local well-posedness of the Euler and Navier-Stokes equations (1.1.1) is well-known. To be specific, given smooth initial data

$$u(x,0) \in C^\infty(R^3)$$

with rapid decay at infinity, for example,

$$|\partial_x^\alpha u(x,0)| \le C_{\alpha K}(1+|x|)^{-K} \quad \text{on } R^3, \text{ for any } \alpha, K,$$

one has a time interval $[0,T)$, on which unique solutions $u(x,t)$ exist and satisfy,

$$u(x,t) \in C^\infty(R^3 \times [0,T)), \quad \|u(x,t)\|_{L^2(R^3)} \le \|u(x,0)\|_{L^2(R^3)}. \tag{1.1.8}$$

The classical results regarding the local-wellposedness for the 3D Euler and Navier-Stokes equations are covered very well in the book [59].

However, the question of global well-posedness of the 3D Euler and Navier-Stokes equations (1.1.1) remains open. Namely, it is not known whether the existence time-interval $[0,T)$ in (1.1.8), on which the solutions are unique and remain smooth, can be extended to $[0,+\infty)$ or not. The global well-posedness of the 3D Navier-Stokes equations ($\nu > 0$) is generally viewed as one of the most important open problems in mathematics, and listed in the millennium problems by the Clay Institute[1].

The major difficulty for the global regularity of the 3D Navier-Stokes equations lies in the supercritical nature of the nonlinearity, see [74]. To be specific, the *a priori* estimate (1.1.7) of the solutions, namely, $\|u\|_{L^2(R^3)}$, gets worse when we zoom in the solutions according to the invariant scaling of the equations (1.1.6),

$$\|\tau^{-1/2} u\left(\frac{x}{\tau^{1/2}}, \frac{t}{\tau}\right)\|_{L^2(R^3)} > \|u\left(x, \frac{t}{\tau}\right)\|_{L^2(R^3)}, \quad \text{for} \quad \tau > 1.$$

In another word, with only the *a priori* estimate (1.1.7), one cannot use the diffusion term $\nu\Delta u$ to control the nonlinear term $B(u,u)$ based on scaling argument.

The potential finite-time singularity of the 3D Euler and Navier-Stokes equations (1.1.1) can be more clear when written in the vorticity form,

$$\omega_t + u \cdot \nabla\omega = \omega \cdot \nabla u + \nu\Delta\omega, \tag{1.1.9a}$$

$$u = \nabla \times \Delta^{-1}\omega, \tag{1.1.9b}$$

where the vorticity ω is the curl of the velocity, $\omega(x,t) = \nabla \times u(x,t)$.

The first term on the RHS of (1.1.9a) is called the vortex stretching term, which is absent in the 2D setting. Note that ∇u is of the same order as ω, and thus the vortex stretching term has a formal quadratic scaling with respect to the vorticity ω, and can lead to potential formation of a finite-time singularity for ω.

[1] www.claymath.org/millennium-problems/navier-stokes-equation

For the 3D Euler equations (1.1.1), namely the case that $\nu = 0$, due to the lack of regularizing mechanism (viscosity), even the local well-posedness of equations can only be obtained with regular enough initial data [44].

See the surveys [31, 17] for more background about this outstanding open question.

Partial Results Concerning the Regularity of Euler and Navier-Stokes

A lot of effort has been devoted to the regularity problem of Euler and Navier-Stokes equations, and we list a few of these results below.

For smooth enough initial data, the Euler and Navier-Stokes equations in the 2D setting are globally well-posed. This is because in the 2D setting, the vortex stretching term in (1.1.9) vanishes, and one can get *a priori* global estimate for the maximal vorticity $\|\omega\|_{L^\infty}$. Then the global regularity of the solutions follows.

For the 3D Euler equations, the celebrated Beale-Kato-Majda (BKM) criterion [6, 26] asserts that the solutions develop finite-time singularity at time T if and only if

$$\int_0^T \|\omega(\cdot,t)\|_{L^\infty} dt = +\infty. \tag{1.1.10}$$

The BKM criterion imposes certain constraint on the blow up rate of the maximal vorticity. For example, $\|\omega\|_\infty$ cannot blow up as $(T-t)^\beta$ with some $\beta > -1$.

The non-blowup criterion of Constantin, Fefferman and Majda [18] focuses on the geometric aspects of 3D Euler flows instead and asserts that there can be no blowup if the velocity field u is uniformly bounded and the vorticity direction $\xi = \omega/|\omega|$ is sufficiently "well-behaved" near the point of maximum vorticity.

The theorem of Deng, Hou and Yu [19, 20] for the 3D Euler equations is similar in spirit to the Constantin-Fefferman-Majda criterion, but confines the analysis to localized vortex line segments. They assert that if the vorticity direction is "well-behave" on a local region near maximum vorticity, then the solutions remain regular. To be specific, their theorems allow the area of the region converges to zero.

For the 3D Navier-Stokes equations, if the initial data is small enough in certain critical norm, namely invariant under the scaling (1.1.6), say

$$\|u\|_{L^2}\|\nabla u\|_{L^2},$$

then the solutions will remain bounded and smooth for all time. See [49] for an essentially optimal result in this direction.

The criterion of Prodi [67] and Serrin [71] claims that for

$$\frac{2}{p}+\frac{3}{q}=1, \quad 3<q\leq+\infty, \tag{1.1.11}$$

if

$$\|u(x,t)\|_{L^p(L^q(R^3),[0,T))}<+\infty,$$

then the solutions can be extended smoothly beyond time T, where

$$\|u(x,t)\|_{L^p(L^q(R^3),[0,T))}=(\int_0^T\|u(x,t)\|^p_{L^q(R^3)})^{1/p}.$$

The condition with $p=+\infty$, $q=3$ in (1.1.11) also implies regularity but is essentially different from (1.1.11). It is proved in [24] by Escauriaza, Seregin and Sverak, which relies on a unique continuation property for backwards heat equations.

Important progress has been made in understanding weak solutions of the Navier-Stokes equations, namely solutions satisfy (1.1.1) in distribution. Leray [55] showed the existence of weak solution with suitable growth properties, while the uniqueness of weak solutions for Navier-Stokes equations is still unknown.

Scheffer [69] proved a partial regularity theorem for suitable weak solutions of the Navier-Stokes equations. Caffarelli-Kohn-Nirenberg [9] improved Scheffer's results, and Lin [57] simplified the proofs of the results in Caffarelli-Kohn-Nirenberg. The partial regularity result asserts that for suitable weak solution of the Navier-Stokes equations, the one-dimensional Hausdorff measure of the singular set has to vanish. In the case of Navier-Stokes equations with axial symmetry, this result implies that singularity can only take place on the symmetric axis.

Due to the lack of analytical tools for super-critical nonlinearity, major breakthrough in analysis is needed to resolve this open problem. T. Tao [73] formalized this super-critical barrier by proposing a 3D model, where the nonlinearity term $B(u,u)$ in (1.1.4) is replaced by an averaging term $\tilde{B}(u,u)$, and one gets

$$u_t=\tilde{B}(u,u)+\Delta u. \tag{1.1.12}$$

The averaged bilinear operator $\tilde{B}(\cdot,\cdot)$ shares several estimates as (1.1.4), and (1.1.12) shares the same energy equality (1.1.7). It is proved in [73] that the averaged model can develop finite-time singularity, which implies that to resolve the Navier-Stokes regularity problem, one has to exploit the fine structure of the nonlinearity.

Numerical Search of Potential Finite-time Singularity

Besides the analytical results mentioned in the previous subsection, there also exists a sizable literature focusing on the numerical search of a finite-time singularity for the 3D Euler equations. These numerical computations have led to improved understanding about the vortex stretching or depletion of nonlinearity.

Representative work in this direction includes the result by Grauer and Sideris [33], and the result by Pumir and Siggia [68] on the 3D axisymmetric Euler equations. Finite-time singularity was reported in those numerical computations. However, by exploiting the analogy between 3D axisymmetric Euler equations and 2D Boussinesq system, E and Shu [22] studied the potential development of finite-time singularity for the 2D Boussinesq system with higher resolution and initial data completely similar to those in [33, 68]. No finite-time singularity was observed, indicating that the finite singularity reported in [33, 68] was likely numerical artifact.

Kerr and his collaborators [47] studied Euler flows generated by a pair of perturbed anti-parallel vortex tubes, and a finite-time singularity was reported. Hou and Li [39] repeated the computation in [47] with higher resolutions to reproduce the singularity scenario, and no finite-time singularity was observed. By using newly developed analytic tools based on rescaled vorticity moments, Kerr also confirmed in [46] that the solutions computed from initial data in [47] eventually converge to superexponential growth and are unlikely to lead to a finite-time singularity.

Other interesting pieces of work are [10, 72], which studied axisymmetric Euler flows with complex initial data and reported singularities in the complex plane. In [8], the Navier-Stokes equations were numerically solved using Kida's high-symmetry initial data, where rapid growth of the solution was observed, but no conclusion could be made regarding singularity formation in finite time.

See the review paper [31] for a more comprehensive list of numerical results.

The previously mentioned numerical results have been non-conclusive since there is no stable structure in the potentially singular solutions. In a recent numerical computation by Luo and Hou [58] for 3D axisymmetric Euler equations, the solutions were observed to develop self-similar structure in the meridian plane. The first two parts of this thesis are related to this new singularity formation scenario, and a more detailed description of the singular solutions will be given there.

1.2 The Role of Self-similarity in Nonlinear PDEs

Self-similar Singularities

Self-similarity plays an important role in the singularity formation of nonlinear PDEs. Consider the following nonlinear evolution PDE

$$u_t = N(u), \tag{1.2.1}$$

where $N(\cdot)$ is a nonlinear term. Assume that the solution to (1.2.1) develops finite-time singularity at a single space time point $(x,t) = (x_0,t_0)$. We shift the singularity point to the origin, and denote x' and t' as shifted variables

$$x' = x - x_0, \quad t' = t - t_0.$$

Then if the local solution of (1.2.1) develops asymptotic structure

$$u(x,t) \approx (t')^{c_u} U(\frac{x'}{(t')^{c_l}}), \tag{1.2.2}$$

with some c_u and c_l, we say the solution develops self-similar singularity. Scaling invariant property of the equation is necessary for self-similar singularity.

Self-similar singularities arise in a lot of nonlinear PDEs governing natural phenomenon. A finite time singularity signals certain physical events such as the solutions change topology, or the emergence of a new structure. Self-similar singularity reveals the universal law and scaling in the corresponding process.

Examples of self-similar singularities arise in free surface flows [76, 75, 7], reaction diffusion equations [32, 35, 63, 29], nonlinear Schödinger equations [21, 65, 62, 61, 27, 60, 51, 54, 52, 64]. See [23] for a survey of self-similar singularity.

Plugging the self-similar ansatz (1.2.2) into equation (1.2.1), if the scaling of the nonlinear terms match each other, we can get the following self-similar equation governing the self-similar profile $U(\xi)$ in the ansatz (1.2.2),

$$c_l \xi \cdot \nabla U(\xi) = N(U(\xi)) + c_u U(\xi). \tag{1.2.3}$$

In the literature [5, 70, 4], self-similar similar singularities are classified into two types, the first kind and the second kind. If the scaling exponents c_u and c_l can be simply determined by dimensional analysis, then the self-similarity is called of the first kind. The exponents often assume rational numbers in the first kind of self-similarity. Self-similar solutions are of the second kind if the solutions exist locally

for a continuous set of scaling exponents c_u, c_l. These local solutions are in general inconsistent with the boundary or initial conditions of the nonlinear PDE (1.2.1), and imposing these boundary conditions leads to a nonlinear eigenvalue problem, whose solution yields irrational scaling exponents in general.

Major Difficulties for Second Kind Self-similar Singularities

We study the self-similar singularity of the Euler equations and related models in this thesis. Plugging the ansatz (1.2.2) into the Euler equations (1.1.1) with $\nu = 0$, and matching the scaling of nonlinear terms, one can get the following condition

$$c_u = c_l - 1,$$

and the exponent c_l cannot be determined by a simple dimensional analysis. Thus the singularity scenarios that we investigated are of the second kind.

Since the self-similar ansatz approximates the singular solutions locally on a region close to the singular point, the self-similar profiles do not necessarily have finite energy, even though the solutions to the Euler equations enjoy energy conservation. For the Euler singularity scenario that we consider in this thesis, the self-similar profiles U are actually increasing with a fractional power at infinity, which makes it hard to find an appropriate function space to study the self-similar profiles.

For the 3D axisymmetric Euler equations that we consider in this thesis, the solutions do not enjoy a perfect scaling invariance centered at the singularity point on the solid boundary, and in deriving the self-similar equations (1.2.3), one needs to discard some lower order terms. In this case one needs certain stability of the self-similar profiles to justify the neglecting of low order terms.

Besides the nonlinear terms in the self-similar equations, the equations are also non-local in nature, since to recover the pressure field in (1.1.2), one needs the velocity field on the whole domain to invert the Laplace operator. The non-locality makes solving the self-similar equations even more challenging.

There exist little analytical results concerning the self-similarity of the second kind in the literature due to the difficulties mentioned above, and in this thesis we study the self-similar singularity of the second kind for the axisymmetric Euler equations and several simplified models both analytically and numerically.

1.3 Summary of the Thesis

Self-similar Singularity of 1D Models of the 3D Axisymmetric Euler Equations

We first consider two 1D models approximating the dynamics of the 3D axisymmetric Euler equations on the solid boundary of a periodic cylinder, the CKY model, and the HL model. The HL model is motivated by the recent finite-time singularity scenario reported by Hou and Luo, and the CKY model is derived as a further approximation of the HL model by simplifying the Biot-Savart law.

For the CKY model, we proved that there exists a discrete family of analytic self-similar profiles corresponding to different leading orders of the profiles at the origin. In the proof, we first construct local self-similar profiles using the power series method, and then extend the local profiles to infinity by solving a nonlinear ODE system. We use computer-aided verification technique to prove the existence of c_l that makes the profiles satisfy the required decay condition at infinity. Some asymptotic properties of the self-similar profiles at infinity are also proved.

Then we use the dynamic rescaling formulation to study the self-similar profiles of the two 1D models numerically. In the dynamic rescaling formulation, scaling terms are added to the equations based on the scaling-variant properties of the solutions, and the resecaling equations govern the evolution of the spatial profiles of the singular solutions. We use the dynamic rescaling formulation to demonstrate the stability of the self-similar singularity. To be specific, starting from initial data sufficiently close to the self-similar profiles, the solutions will also develop singularity with the same asymptotic structure as the self-similar ansatz.

For the HL model, we also show that the solutions can develop singularity at multiple scales for certain initial data, which is different from the CKY model.

Two Types of Singular Behaviors for the 3D Axisymmetric Euler Equations

The 3D Euler axisymmetric equations away from the axis are qualitatively similar to the 2D Boussinesq system. In the finite-time singularity scenario reported by Luo and Hou [58], the leading order terms in the 3D axisymmetric Euler equations are exactly the same as the 2D Boussinesq system, and we use the dynamic rescaling formulation for the 2D Boussinesq system to study the self-similar singularity reported in [58]. The dynamic rescaling equations of the 3D axisymmetric Euler equations can be viewed as a perturbation to that of the 2D Boussinesq system with the perturbation term converging to zero exponentially fast in time.

With appropriate local analytic boundary conditions, we prove the existence of a

family of local self-similar profiles for the 2D Boussinesq system. The proof needs a modification of the Cauchy-Kowalevski majorization argument [50] due to the existence of a formal singularity of the self-similar equations at the origin.

We consider two types of initial data with different leading order properties. The first initial data correspond to the singular solutions reported by Luo and Hou, where self-similar singularity is observed. Our numerical study suggests that the 2D Boussinesq system develops stable self-similar singularity, and the stability of profiles confirms the singularity for 3D axisymmetric Euler reported in [58].

For our second choice of initial data for the dynamic rescaling equations, the solutions develop a singularity themselves. In another word, there is a smaller scale generated, and correspondingly the solutions of the original Euler equations develop finite-time singularity at multiple scales, which is very different from the behavior of the singular solutions reported by Luo and Hou in [58]. This result agrees with our direct numerical simulation of the 2D Boussinesq system.

The stability studies for the self-similar profiles may help to get better understanding about the singularity formation mechanism for the 3D Euler equations.

A Family of 3D Models of the 3D Axisymmetric Euler Equations

For the axisymmetric Euler and Navier-Stokes equations written in cylindrical coordinates, Hou and Lei [37] removed the convection terms and obtained a 3D model of the Euler and Navier-Stokes equations. This model enjoys a similar energy identity and shares several non-blowup criteria with the 3D Euler and Navier-Stokes equations [37]. The partial regularity result for the Navier-Stokes equations also holds for this new viscous 3D model [36]. Moreover, the inviscid 3D model can develop finite-time singularity under certain Dirichlet-Robin boundary conditions [43]. The numerically observed finite-time singularity will be destroyed if the convection is added back, which reveals the stabilizing effect of convection.

In this thesis, we consider a family of models obtained by applying a factor ϵ to the convection terms of the axisymmetric Euler and Navier-Stokes equations. The case $\epsilon = 1$ corresponds to the original Euler and Navier-Stokes equations, and the case $\epsilon = 0$ corresponds to the models of Hou and Lei [37]. The family of models share a similar energy identity and several regularity results with the Euler and Navier-Stokes equations. Our numerical results suggest that the inviscid models develop singularity for small ϵ, and the singular solutions develop self-similar structure with the singularity region non-stationary but travelling. The dynamic rescaling forma-

tion demonstrates that the travelling self-similar singularity scenario is stable.

As we increase the amplitude of the convection, the self-similar singularity scenario disappears. This numerical result demonstrates the stabilizing effect of convection.

Chapter 2

SELF-SIMILAR SINGULARITY OF TWO 1D MODELS

In this chapter, we consider two 1D models of the 3D axisymmetric Euler equations, and investigate the stability of the spatial profiles in their singular solutions.

2.1 Derivation of the Two 1D Models

The two 1D models are motivated by the recent numerical computation of Luo and Hou in [58], and they approximate the dynamics of the axisymmetric Euler equations on the solid boundary of a cylindrical domain.

Let e_r, e_θ and e_z be the standard vectors defining the cylindrical coordinate system,

$$e_r = (\frac{x_1}{r}, \frac{x_2}{r}, 0)^T, \quad e_\theta = (\frac{x_2}{r}, -\frac{x_1}{r}, 0)^T, \quad e_z = (0,0,1)^T,$$

where $r = \sqrt{x_1^2 + x_2^2}$. Then the velocity field is called axisymmetric if

$$u = u^r(r, x_3, t)e_r + u^\theta(r, x_3, t)e_\theta + u^z(r, x_3, t)e_z,$$

namely, u^r, u^θ and u^z do not depend on the θ coordinate. The axisymmatric Euler equations can be written in cylindrical coordinates with $z = x_3$ as

$$u_t^\theta + u^r u_r^\theta + u^z u_z^\theta = -\frac{1}{r} u^r u^\theta, \tag{2.1.1a}$$

$$\omega_t^\theta + u^r \omega_r^\theta + u_z \omega_z^\theta = \frac{2}{r} u^\theta u_z^\theta + \frac{1}{r} u^r \omega^\theta, \tag{2.1.1b}$$

$$-[\Delta - \frac{1}{r^2}]\phi^\theta = \omega^\theta, \tag{2.1.1c}$$

where the radial and angular velocity fields u^r and u^θ are recovered as

$$u^r = -\partial_z \phi^\theta, \quad u^z = r^{-1}\partial_r(r\phi^\theta).$$

Note that equations (2.1.1) have a formal singularity at the axis $r = 0$ due to the $\frac{1}{r}$ terms, and it can be removed by introducing the transformed variables

$$u_1 = u^\theta / r, \quad w_1 = w^\theta / r, \quad \phi_1 = \phi^\theta / r. \tag{2.1.2}$$

One can get the equations for u_1 and ω_1 as the following,

$$u_{1,t} + u^r u_{1,r} + u^z u_{1,z} = 2u_1 \phi_{1,z}, \tag{2.1.3a}$$

$$w_{1,t} + u^r w_{1,r} + u^z w_{1,z} = (u_1^2)_z, \tag{2.1.3b}$$

$$-[\partial_r^2 + (3/r)\partial_r + \partial_z^2]\phi_1 = w_1, \tag{2.1.3c}$$

with Boit-Savart law

$$u^r = -r\phi_{1,z}, \quad u^z = 2\phi_1 + r\phi_{1,r}. \tag{2.1.3d}$$

In the numerical computation [58], (2.1.3) were numerically solved in a periodic cylinder $(r,z) \in [0,1] \times S^1$. It is reported that with initial data

$$w_1(r,z,0) = 0, \quad u_1(r,z,0) = 100e^{-30(1-r^2)^4} \sin(2\pi z),$$

the numerical solutions to (2.1.3) develop finite-time singularity on the boundary $(r,z) = (1,0)$. The vorticity and velocity fields of the potentially singular solutions roughly take the configuration illustrated in Figure 2.1.

The no-flow boundary condition and the symmetry of the data in the axial direction create a compressing flow along the solid boundary of the cylinder, which seems responsible for the numerically observed finite-time singularity.

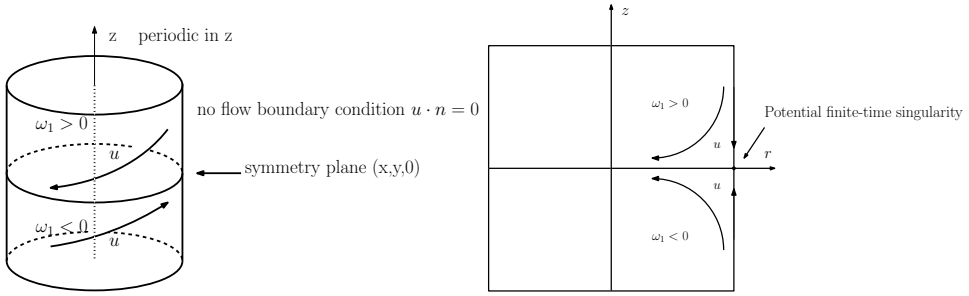

(a) In the 3D space. (b) In the meridian plane.

Figure 2.1: Vorticity and velocity fields in the numerical computation [58].

Motivated by this new finite-time singularity formation scenario in Figure 2.1, Kiseleve and Sverak in [48] constructed an example of 2D Euler solutions in a similar setting, and proved that the maximal gradient of the vorticity field in that example exhibits double exponential growth in time, which is known as the fastest possible rate of growth for the 2D Euler equations. This example provides further evidence that this new finite-time singularity formation scenario reported in [58] is an interesting candidate to investigate the potential 3D Euler singularity.

Because of the no-flow boundary condition, we have $u^r = 0$, $\phi_{1,z} = 0$ on the boundary $r = 1$. Restricting equations (2.1.3) on $r = 1$ gives the following 1D system,

$$w_t(x,t) + u(x,t)w_x(x,t) = \theta_x(x,t), \tag{2.1.4a}$$

$$\theta_t(x,t) + u(x,t)\theta_x(x,t) = 0, \tag{2.1.4b}$$

where $u(x,t)$ $w(x,t)$ and $\theta(x,t)$ correspond to u^z, w^1 and u_1^2 in (2.1.3).

The 1D model system (2.1.4) is exact in the sense that it is obtained as the restriction of the 3D axisymmetric Euler equations on the solid boundary without any approximation. To close the above 1D system (2.1.4), one needs an appropriate Biot-Savart law connecting the velocity field $u(x,t)$ with the vorticity field $w(x,t)$.

In [41], Hou and Luo proposed and investigated the following model,

$$u_x = \mathcal{H} w, \quad x \in [-1,1], \tag{2.1.5a}$$

where $\mathcal{H}$ is the periodic Hilbert transform. Namely,

$$u_x(x) = \text{P.V.}\frac{1}{2}\int_{-1}^{1} w(y)\cot[\frac{\pi}{2}(x-y)]dy, \quad x \in [-1,1]. \tag{2.1.5b}$$

For odd vorticity field w, we can derive by direct integration that

$$u_{\text{HL}}(x) = \frac{1}{\pi}\int_0^1 w(y)\log\left|\frac{\tan(\frac{\pi}{2}x)-\tan(\frac{\pi}{2}y)}{\tan(\frac{\pi}{2}x)+\tan(\frac{\pi}{2}y)}\right|dy, \quad x \in [0,1]. \tag{2.1.5c}$$

We refer to the above model (2.1.5) together with (2.1.4) as the HL-model. The HL-model preserves the odd and even properties of w^1 and u^z in the axisymmetric Euler equations (2.1.3), and can be derived by assuming that the vorticity w^1 in (2.1.3) is constant in the r direction near the boundary, see [41, 15]. The finite-time singularity of the HL-model from smooth initial data is proved in [15].

In [14], Choi, Kiselev and Yao proposed the following model,

$$u_{\text{CKY}}(x) = -x\int_x^1 \frac{w(y)}{y}dy, \quad x \in [0,1], \tag{2.1.6}$$

with boundary conditions

$$w(0,t) = 0, \quad \theta(0,t) = \theta_x(0,t) = 0,$$

to close the system (2.1.4). We refer to model (2.1.6) together with (2.1.4) as the CKY-model, whose finite time singularity is proved in [14]. The CKY-model is proposed as a further simplification of the HL-model. One can show that the CKY-model is a leading order approximation to the HL-model at the origin,

$$u_{\text{HL}}(x) - \frac{\pi}{2}u_{\text{CKY}}(x) = O(x^2), \quad x \to 0.$$

More discussions about the derivation of the two models can be found in [15].

The mechanism of the finite-time singularity for the two 1D models is the following: the positive $w(x,t)$ near the origin creates a compressing flow $u(x,t) < 0$ according to the Biot-Savart laws (2.1.5), (2.1.6); this compressing flow produces a larger $\theta_x(x,t)$ near the origin according to equation (2.1.4b), since $\theta(x,t)$ is convected by the velocity field $u(x,t)$; according to equation (2.1.4a), $\theta_x(x,t)$ is the time derivative of w along characteristics, and thus $w(x,t)$ will in turn get larger; this nonlinear amplification mechanism finally leads to finite-time singularity.

2.2 The Self-similar Equations Governing the Self-similar Profiles

One can easily verify that the 1D models (2.1.5) and (2.1.6) both enjoy the following scaling invariant property for $\lambda > 0$, $\mu > 0$,

$$w(x,t) \to \frac{1}{\mu} w(\frac{x}{\lambda}, \frac{t}{\mu}), \quad u(x,t) \to \frac{\lambda}{\mu} u(\frac{x}{\lambda}, \frac{t}{\mu}), \quad \theta(x,t) \to \frac{\lambda}{\mu^2} \theta(\frac{x}{\lambda}, \frac{t}{\mu}). \tag{2.2.1}$$

The singular solutions to the two models both develop local self-similar structure around the origin, so we make the following ansatz to the local solutions,

$$\theta(x,t) = (T-t)^{c_\theta} \Theta\left(\frac{x}{(T-t)^{c_l}}\right), \tag{2.2.2a}$$

$$w(x,t) = (T-t)^{c_w} W\left(\frac{x}{(T-t)^{c_l}}\right), \tag{2.2.2b}$$

$$u(x,t) = (T-t)^{c_u} U\left(\frac{x}{(T-t)^{c_l}}\right). \tag{2.2.2c}$$

Plugging the ansatz into equations (2.1.4), (2.1.5) and (2.1.6), and matching the exponents of $(T-t)$, we get the following relation of the scaling exponents,

$$c_w = -1, \quad c_u = c_l - 1, \quad c_\theta = c_l - 2. \tag{2.2.3}$$

The self-similar profiles $U(\xi)$, $W(\xi)$, $\Theta(\xi)$ satisfy the following equations, which are defined on $\xi \in R^+$ and will be referred to as the self-similar equations,

$$W(\xi) + c_l \xi W'(\xi) + U(\xi) W'(\xi) - \Theta'(\xi) = 0, \tag{2.2.4a}$$

$$(2 - c_l)\Theta(\xi) + c_l \xi \Theta'(\xi) + U(\xi)\Theta'(\xi) = 0. \tag{2.2.4b}$$

The Biot-Savart laws of the HL-model (2.1.5) and the CKY-model (2.1.6) become

$$U_{HL} = \frac{1}{\pi} \int_0^\infty \ln \left| \frac{\xi - \eta}{\xi + \eta} \right| W(\eta) d\eta, \tag{2.2.5a}$$

$$U_{CKY} = -\xi \int_\xi^\infty \frac{W(\eta)}{\eta} d\eta. \tag{2.2.5b}$$

Note that $\|\theta\|_{L^\infty}$ is conserved for the two 1D models, and thus we require that

$$c_\theta = c_l - 2 \geq 0.$$

The singularity of the two models are both point singularity, namely, $w(x,t)$ and $\theta(x,t)$ remain bounded away from the origin up to the singularity time. This requires us to impose the following decay condition at infinity,

$$\Theta(\xi) = O(\xi^{1-2/c_l}),\ W(\xi) = O(\xi^{-1/c_l}),\ U(\xi) = O(\xi^{1-1/c_l}), \quad \xi \to +\infty. \quad (2.2.6)$$

The self-similar equations (2.2.4) enjoy the following scaling-invariant property,

$$W(\xi) \to W(\frac{\xi}{\lambda}), \quad \Theta(\xi) \to \lambda\Theta(\frac{\xi}{\lambda}), \quad U(\xi) \to \lambda U(\frac{\xi}{\lambda}). \quad (2.2.7)$$

The self-similar singularity for the two 1D models are of the second kind, since the scaling exponent c_l cannot be determined from dimensional analysis. And to solve the self-similar equations (2.2.4), one needs to find c_l such that (2.2.4) have non-trivial solutions, which is essentially a nonlinear eigenvalue problem.

2.3 Existence of Self-similar Profiles for the CKY Model

In this section, we prove the existence of a family of self-similar profiles for the CKY model. The Biot-Savart law of the CKY model

$$U(\xi) = -\xi \int_\xi^{+\infty} \frac{W(\eta)}{\eta} d\eta$$

can be rewritten as a local relation (2.3.1a) with a global constraint (2.3.1b),

$$\left(\frac{U(\xi)}{\xi}\right)' = \frac{W(\xi)}{\xi}, \quad (2.3.1a)$$

$$\lim_{\xi\to+\infty} \frac{U(\xi)}{\xi} = 0. \quad (2.3.1b)$$

We first ignore the decay condition (2.3.1b), then the self-similar equations with (2.2.5b) replaced by (2.3.1a) become a nonlinear ODE system with singular RHS at $\xi = 0$, i.e., the RHS does not satisfy the Lipschitz condition at the origin. We construct local solutions to this ODE system near $\xi = 0$ using a power series method, which can naturally overcome the formal singularity of the RHS at $\xi = 0$. The power series are unique up to a rescaling parameter for fixed c_l and leading order of $\Theta(\xi)$ at $\xi = 0$, and they can be extended to the whole $\mathbf{R}^+$ by solving the ODE

system. Then we prove that the decay condition (2.3.1b) determines the scaling exponents, and there exists a discrete family of c_l, corresponding to different leading orders of $\Theta(\xi)$, such that the decay condition (2.3.1b) holds for the self-similar profiles that we construct. We prove this part with the assistance of numerical computation and rigorous error control. With the decay condition (2.3.1b), we further analyze the far-field properties of these self-similar profiles and prove that the profiles satisfy condition (2.2.6) at $\xi = +\infty$. We have the following theorem.

Theorem 2.3.1. *There exist a discrete family of scaling exponent c_l and analytic solutions to the self-similar equations* (2.2.4)*, corresponding to different leading orders of the self-similar profile $\Theta(\xi)$ at the origin $\xi = 0$,*

$$s = \min\{k \in N^+ | \ \frac{d^k}{d\xi^k}\Theta(0) \neq 0\}. \tag{2.3.2}$$

And in the far-field, $W(\xi)$, $U(\xi)\xi^{-1}$, $\Theta(\xi)\xi^{-1}$ are analytic with respect to a transformed variable $\zeta = \xi^{-1/c_l}$ at $\zeta = 0$.

Remark 2.3.1. The self-similar profiles that we construct are non-conventional since the velocity $U(\xi)$ does not decay to zero at infinity but grows as

$$U(\xi) = O(\xi^{\frac{c_l-1}{c_l}}), \quad \xi \to +\infty.$$

Correspondingly, the velocity field at the singularity time is Hölder continuous

$$U(x,T^-) = \lim_{t\to T^-}(T-t)^{c_u}U(\frac{x}{(T-t)^{c_l}}) = Cx^{\frac{c_l-1}{c_l}}.$$

Such behavior is also observed in the numerical simulation of the 3D Euler equations in [41]. The far field property of our constructed self-similar profiles is very different from the Leray type of self-similar solutions, whose existence has been ruled out under certain decay assumptions on the self-similar profiles [12, 11, 13].

Construction of the Near-field Solutions

The use of power series method to analyze analytic differential equations is classical, and can be traced back to the Cauchy-Kowalevski Theorem [50, 28]. At a regular point of an ODE system, the manifold of local solutions can be parametrized by the initial values of the solutions [16]. For the self-similar ODE system (2.2.4) and (2.3.1a), we consider its local analytic solutions near a singular point and show that they can be parameterized by the leading order of $\Theta(\xi)$.

Lemma 2.3.1. *For fixed $c_l > 2$, and the leading order of $\Theta(\xi)$ at the origin, $s \geq 2$, there exist unique (up to the scaling-invariance* (2.2.7)*) local analytic solutions to equations* (2.2.4) *and* (2.3.1a)*, with boundary conditions,*

$$W(0) = 0, \quad \Theta^{(k)}(0) = 0, \quad \textit{for} \quad k < s. \tag{2.3.3}$$

Proof. According to the boundary conditions (2.3.3), we assume that

$$\Theta(\xi) = \sum_{k=2}^{\infty} \Theta_k \xi^k, \quad U(\xi) = \sum_{k=1}^{\infty} U_k \xi^k, \quad W(\xi) = \sum_{k=1}^{\infty} W_k \xi^k. \tag{2.3.4a}$$

Based on the local relation in the Biot-Savart law (2.3.1a), we have

$$W_k = k U_{k+1}. \tag{2.3.4b}$$

Plugging (2.3.4) into (2.2.4) and matching the k-th ($k \geq 1$) order term ξ^k, we get

$$(2 - c_l)\Theta_k + k c_l \Theta_k + \sum_{m=1}^{k-1} (k - m + 1)\Theta_{k-m+1} U_m = 0, \tag{2.3.5a}$$

$$(k-1)U_k + c_l (k-1)^2 U_k + \sum_{m=1}^{k-1} U_m (k-m)^2 U_{k-m+1} - k\Theta_k = 0. \tag{2.3.5b}$$

Let $s \geq 2$ (2.3.2) be the leading order of $\Theta(\xi)$ at the origin. Recall that we need $\theta_x > 0$ locally to produce the finite-time singularity, so we require that

$$\Theta_i = 0 \text{ for } i < s, \quad \Theta_s > 0, \ \ s \geq 2. \tag{2.3.6}$$

To make (2.3.5a) hold for $1 \leq k \leq s$, we require

$$(2 - c_l + s c_l + s U_1)\Theta_s = 0. \tag{2.3.7}$$

Since $\Theta_s \neq 0$, we require

$$U_1 = \frac{(1-s)c_l - 2}{s}. \tag{2.3.8}$$

To make (2.3.5b) hold for $2 \leq k < s$, we require

$$[(k-1) + c_l (k-1)^2 + U_1 (k-1)^2] U_k = 0. \tag{2.3.9}$$

Since $c_l > 2$, and $[(k-1) + c_l (k-1)^2 + U_1 (k-1)^2] > 0$, we require

$$U_k = 0, \quad 1 < k < s. \tag{2.3.10}$$

And to make (2.3.5b) hold for $k = s$, we require

$$U_s = \frac{s^2\Theta_s}{(sc_l - c_l - s + 2)(s-1)} > 0. \tag{2.3.11}$$

For $k > s$, to make (2.3.5) hold, the coefficients Θ_k and U_k should satisfy

$$\Theta_k = \frac{-\sum_{m=s}^{k-1} U_m(k-m+1)\Theta_{k-m+1}}{(k/s-1)(c_l-2)}, \tag{2.3.12a}$$

$$U_k = \frac{k\Theta_k - \sum_{m=s}^{k-1} U_m(k-m)^2 U_{k-m+1}}{(k-1) + (c_l/s - 2/s)(k-1)^2}, \tag{2.3.12b}$$

which means the power series (2.3.4) can be determined inductively.

To complete the proof, we need the constructed power series (2.3.4) converge for $|\xi|$ small enough. We choose $u^0, \theta^0, r > 0$ such that the following condition holds

$$|U_s| \le \frac{1}{s^2}u^0 r^s, \quad |\Theta_s| \le \frac{1}{s}\theta^0 r^s, \quad \frac{(s+1)u^0 r}{c_l/s - 2/s} \le 1, \quad \frac{9}{4}\frac{\theta^0/u^0 + u^0 r}{c_l/s - 2/s} < 1. \tag{2.3.13}$$

We can achieve this by choosing $u_0 r$ and θ_0/u_0 small enough to make the last two hold, and then choosing r large enough to make the first two hold. For example, let

$$A = \min\{\frac{c_l - 2}{s(s+1)}, \frac{2(c_l-2)}{9s}\},\ B = \frac{2(c_l-2)}{9s},\ C = \max\{\frac{s\Theta_s}{AB}, \frac{s^4\Theta_s}{A(sc_l - c_l - s + 2)}\}.$$

Then the choice of

$$u^0 = \frac{A}{C^{1/(s-1)}}, \quad \theta^0 = u^0 B, \quad r = C^{1/(s-1)},$$

will satisfy (2.3.13). And we will use induction to prove that for all $k \ge s$,

$$|U_k| \le \frac{1}{k^2}u^0 r^k, |\Theta_k| \le \frac{1}{k}\theta^0 r^k. \tag{2.3.14}$$

For $k = s$, (2.3.14) holds by (2.3.13). Assume now that for $s \le k < n$, (2.3.14) holds, then for $k = n \ge s+1$, based on (2.3.12a) we have

$$|\Theta_n| \le \frac{\sum_{m=s}^{n-1} |U_m||(n-m+1)||\Theta_{n-m+1}|}{(n-s)(c_l/s - 2/s)}.$$

Using the induction assumption and the fact that $\sum_{m=2}^{\infty} \frac{1}{m^2} \le 1$, we have

$$|\Theta_n| \le \frac{\theta^0 u^0 r^{n+1}}{(n-s)(c_l/s - 2/s)} \le \frac{\theta^0 r^n}{n} \times \frac{(s+1)u^0 r}{c_l/s - 2/s} \le \frac{\theta^0 r^n}{n},$$

where we have used the fact $n \ge s+1$ in the second inequality and (2.3.13) in the third inequality. Thus (2.3.14) holds for Θ_n. Based on (2.3.12b), we have

$$|U_n| \le \frac{|n\Theta_n| + \sum_{m=s}^{n-1} |U_m(n-m)^2||U_{n-m+1}|}{(c_l/s - 2/s)(n-1)^2}. \tag{2.3.15}$$

Using the induction assumption and the fact that $\sum_{m=2}^{\infty} \frac{1}{m^2} \leq 1$, we get

$$|U_n| \leq \frac{\theta^0 r^n + (u^0)^2 r^{n+1}}{(c_l/s - 2/s)(n-1)^2} \leq \frac{u_0 r^n}{n^2} \times \frac{\theta_0/u_0 + u_0 r}{c_l/s - 2/s} \times \frac{n^2}{(n-1)^2} \leq \frac{u_0 r^n}{n^2},$$

where we have used (2.3.13) and the fact that $n \geq 3$, $n^2/(n-1)^2 \leq 9/4$.

So we get that (2.3.14) holds by induction, which implies that the power series (2.3.4) converge in some interval $[0, 1/r)$. Note that we have one degree of freedom Θ_s (2.3.7) in constructing the power series solutions, which plays the same role as the rescaling parameter (2.2.1). With this we complete the proof of Theorem 2.3.1.

□

The power series (2.3.4) that we construct only converge in a short interval near $\xi = 0$. However, these local self-similar profiles can be extended to $+\infty$.

Lemma 2.3.2. *For $c_l > 2$, the analytic solutions* (2.3.4) *that we construct in Theorem 2.3.1 can be extended to the whole $\mathbf{R}^+$, resulting in global solutions to equations* (2.2.4) *and* (2.3.1a)*. Moreover, we have that for $\xi > 0$,*

$$W(\xi) > 0, \quad \Theta(\xi) > 0. \tag{2.3.16}$$

Proof. Since $U_1 = \frac{(1-s)c_l - 2}{s}$ according to (2.3.8), we have

$$c_l + U_1 = (c_l - 2)/s > 0.$$

Moreover, according to (2.3.11), we have

$$\Theta_s > 0, \quad W_s = (s-1)U_s > 0.$$

Based on the leading orders of the power series (2.3.4), we can choose $\epsilon < \frac{1}{r}$ small enough such that

$$c_l \epsilon + U(\epsilon) > 0, \quad W(\epsilon) > 0, \quad \Theta(\epsilon) > 0.$$

Then we consider extending the self-similar profiles from $\xi = \epsilon$ to $+\infty$ by solving the ODE system with initial data given by the power series (2.3.4).

Let $\tilde{U}(\xi) = c_l \xi + U(\xi)$, and then according to (2.2.4), $\tilde{U}(\xi)$, $\Theta(\xi)$ and $W(\xi)$ satisfy

$$\Theta'(\xi) = \frac{(c_l - 2)\Theta(\xi)}{\tilde{U}(\xi)}, \tag{2.3.17a}$$

$$W'(\xi) = \frac{(c_l - 2)\Theta(\xi)}{\tilde{U}(\xi)^2} - \frac{W(\xi)}{\tilde{U}(\xi)}, \tag{2.3.17b}$$

$$\left(\frac{\tilde{U}(\xi)}{\xi}\right)' = \frac{W(\xi)}{\xi}. \tag{2.3.17c}$$

The right hand side of (2.3.17) is locally Lipschitz continuous for $\tilde{U}(\xi) \neq 0$, $\xi \neq 0$, so we can solve the ODE system from ϵ and get its solutions on interval $[\epsilon, T)$.

We first prove that $W(\xi)$ is positive on $[\epsilon, T)$.

Otherwise denote $\xi = t$ as the first time $W(\xi)$ reaches 0, i.e.

$$t = \inf\{s \in [\epsilon, T) : W(s) \leq 0\}.$$

Then we have $W(\xi)$ is positive on $[\epsilon, t)$, and

$$W'(t) \leq 0. \tag{2.3.18}$$

Based on (2.3.17c), $\frac{\tilde{U}(\xi)}{\xi}$ is increasing on $[\epsilon, t)$, and thus $\tilde{U}(\xi) > \tilde{U}(\epsilon) > 0$ for $\xi \in [\epsilon, t]$. Then based on (2.3.17a), $\Theta(\xi)$ is increasing on $[\epsilon, t]$, and $\Theta(t) > 0$.

Evaluating (2.3.17b) at $\xi = t$, we get

$$W'(t) = \frac{(c_l - 2)\Theta(t)}{\tilde{U}(t)^2} > 0,$$

which contradicts with (2.3.18). So $W(\xi) > 0$ and consequently $\Theta(\xi) > 0$.

Using the fact that $W(\xi) > 0$ in (2.3.17c), we have that for $\xi > \epsilon$,

$$\tilde{U}(\xi) \geq C_0 \xi. \tag{2.3.19}$$

Using this lower bound in (2.3.17a), we get

$$\Theta'(\xi) \leq \frac{C_1 \Theta(\xi)}{\xi}.$$

This implies that for $\xi > \epsilon$

$$\Theta(\xi) \leq C_2 \xi^{C_1}. \tag{2.3.20}$$

Using (2.3.20), (2.3.19) and the fact that $W(\xi)$ is positive in (2.3.17b), we have

$$W'(\xi) \leq C_3 \xi^{C_1 - 2}.$$

Thus for $\xi > \epsilon$,

$$W(\xi) \leq C_4 \xi^{C_1}. \tag{2.3.21}$$

Finally using (2.3.21) in (2.3.17c), we get that for $\xi > \epsilon$,

$$\tilde{U}(\xi) \leq C_5 \xi^{C_1 + 1}. \tag{2.3.22}$$

The C_0, C_1,... C_5 in the above estimates are positive constants.

These *a priori* estimates (2.3.19), (2.3.22), (2.3.20) and (2.3.21) together imply that we can get solutions to (2.3.17) on $[\epsilon, +\infty)$, i.e., the local self-similar profiles that are constructed using power series can be extended to $+\infty$. □

Determination of the Scaling Exponents

In constructing self-similar profiles in the previous section, we did not consider the decay condition (2.3.1b). In this subsection, we show that the decay condition determines the scaling exponent c_l, i.e. only for certain c_l do the constructed self-similar profiles satisfy the decay condition. Recall that for fixed leading order of $\Theta(\xi)$, s, and the value of the leading order $\Theta_s = 1$, the constructed profiles $U(\xi)$, $\Theta(\xi)$ and $W(\xi)$ depend on c_l only. So we can define a function $G(c_l)$ as

$$G(c_l) = \lim_{\xi \to +\infty} \frac{U(\xi)}{\xi}.$$

We will prove that $G(c_l) < +\infty$ and it is a continuous function of c_l. Then the existence of c_l to make the decay condition (2.3.1b) hold will follow from the Intermediate Value Theorem if we can show that there exist c_l^l and c_l^r such that

$$G(c_l^l) < 0, \quad G(c_l^r) > 0. \tag{2.3.23}$$

Lemma 2.3.3. *For fixed $c_l > 2$ and leading order of $\Theta(\xi)$, $s \geq 2$, construct power series* (2.3.4) *with $\Theta_s = 1$, and extend the profiles to $\mathbf{R}^+$ using* (2.3.17)*. Then*

$$G(c_l) = \lim_{\xi \to \infty} \frac{U(\xi)}{\xi} < +\infty,$$

and $G(c_l)$ is a continuous function of c_l.

For the convenience of analysis, we first make the following change of variables,

$$\eta = \xi^{1/c_l}, \quad \hat{W}(\eta) = W(\xi), \quad \hat{U}(\eta) = U(\xi)\xi^{-1}, \quad \hat{\Theta}(\eta) = \Theta(\xi)\xi^{-1+2/c_l}. \tag{2.3.24}$$

Then we have

$$G(c_l) = \lim_{\eta \to +\infty} \hat{U}(\eta),$$

and the ODE system satisfied by $\hat{U}(\eta), \hat{\Theta}(\eta), \hat{W}(\eta)$ is

$$\hat{\Theta}'(\eta) = \frac{(2/c_l - 1)\hat{\Theta}(\eta)\hat{U}(\eta)}{\eta + 1/c_l\hat{U}(\eta)\eta}, \tag{2.3.25a}$$

$$\hat{W}'(\eta) = \frac{-\hat{W}(\eta)}{\eta + 1/c_l\hat{U}(\eta)\eta} + \frac{(1 - 2/c_l)\hat{\Theta}(\eta)}{(1 + 1/c_l\hat{U}(\eta))^2\eta^3}, \tag{2.3.25b}$$

$$\hat{U}'(\eta) = \frac{c_l\hat{W}(\eta)}{\eta}. \tag{2.3.25c}$$

According to (2.3.8), (2.3.16) and the fact that $\hat{U}(\eta)$ is increasing, we have

$$\hat{U}(\eta) > \hat{U}(0) = \frac{(1 - s)c_l - 2}{s}, \quad \hat{W}(\eta) > 0, \quad \hat{\Theta}(\eta) > 0, \quad \text{for} \quad \eta > 0. \tag{2.3.26}$$

We will first prove the following two supporting lemmas.

Lemma 2.3.4. *For all $c_l > 2$, $G(c_l) > -2$.*

Proof. Assume that for some $c_l > 2$, $G(c_l) \leq -2$. Then, according to (2.3.26) and the fact that $\hat{U}(\eta)$ is increasing, we have that for all $\eta > 0$,

$$\frac{(1-s)c_l - 2}{s} < \hat{U}(\eta) < -2.$$

Then we get

$$\frac{(2/c_l - 1)\hat{U}(\eta)}{1 + 1/c_l\hat{U}(\eta)} \geq 2.$$

It follows from (2.3.25a) that

$$\hat{\Theta}'(\eta) \geq 2\frac{\hat{\Theta}(\eta)}{\eta}.$$

By direct integration and (2.3.26), we have that for η large enough,

$$\hat{\Theta}(\eta) \geq C_1\eta^2.$$

Using this estimate and (2.3.26) in (2.3.25b), we get

$$\hat{W}'(\eta) \geq -\frac{C_2\hat{W}(\eta)}{\eta} + \frac{C_3}{\eta}.$$

This implies

$$(\eta^{C_2}\hat{W}(\eta))' \geq C_3\eta^{C_2-1}.$$

Then we have that for η large enough,

$$\eta^{C_2}\hat{W}(\eta) \geq \frac{C_3}{C_2}\eta^{C_2} - C_4.$$

Using this lower bound in (2.3.25c), we get

$$\hat{U}'(\eta) \geq \frac{C_5}{\eta} - \frac{C_6}{\eta^{C_2+1}}. \tag{2.3.27}$$

The constants C in the above estimates are positive and independent of η. The inequality (2.3.27) implies that $\hat{U}(\eta) \to +\infty$ as $\eta \to +\infty$, which contradicts with $G(c_l) \leq -2$. This completes the proof of Lemma 2.3.4. □

We add a subscript c_l to indicate the dependence of the constructed self-similar profiles on the parameter c_l for the rest part of this subsection:

$$\hat{U}_{c_l}(\eta) = \hat{U}(\eta), \quad \hat{W}_{c_l}(\eta) = \hat{W}(\eta), \quad \hat{\Theta}_{c_l}(\eta) = \hat{\Theta}(\eta).$$

Lemma 2.3.5. *For $s \geq 2$ and $c_l > 2$, choose $\Theta_s = 1$ in constructing the power series* (2.3.4)*, and extend the local profiles to $\mathbf{R}^+$ using* (2.3.17)*. Then for fixed η, $\hat{U}_{c_l}(\eta)$, $\hat{W}_{c_l}(\eta)$ and $\hat{\Theta}_{c_l}(\eta)$ are continuous as functions of c_l.*

Proof. We only need to prove for fixed $c_l^0 > 2$, $\hat{U}_{c_l}(\eta)$, $\hat{\Theta}_{c_l}(\eta)$ and $\hat{W}_{c_l}(\eta)$ as functions of c_l are continuous at $c_l = c_l^0$. In our construction of the power series using (2.3.12), we can easily see that the coefficients U_k and Θ_k depend continuously on c_l. And based on (2.3.13), there exist uniform upper bounds of the coefficients

$$|U_k| \leq \frac{u^0 r^k}{k^2}, \quad |\Theta_k| \leq \frac{\theta^0 r^k}{k},$$

for c_l in a neighborhood of c_l^0. This means there exists a fixed ϵ small enough, such that $\hat{W}_{c_l}(\epsilon)$, $\hat{\Theta}_{c_l}(\epsilon)$ and $\hat{U}_{c_l}(\epsilon)$ as functions of c_l are continuous at c_l^0.

Then we can use the continuous dependence of ODE solutions on initial data and parameters to complete the proof of this lemma. □

Now we begin to prove Lemma 2.3.3. We use an iterative method which enables us to get sharper estimates of the profiles after each iteration. We finally obtain that $\hat{U}_{c_l}(\eta)$ converges uniformly to $G(c_l)$ and complete the proof.

Proof. Consider $c_l^0 > 2$, and it is sufficient to prove that $G(c_l^0) < +\infty$, and $G(c_l)$ as a function is continuous at the point $c_l = c_l^0$.

According to Lemma 2.3.4 and Lemma 2.3.5, there exists η_0 large and a neighborhood of c_l^0, $I_0 = (c_1, c_2)$ with $c_1 > 2, c_2 < +\infty$, such that for $c_l \in I_0$ and $\eta > \eta_0$,

$$\hat{U}_{c_l}(\eta) > \hat{U}_{c_l}(\eta_0) > -2 + \epsilon_1. \tag{2.3.28}$$

Then for $c_l \in I_0$ and $\eta > \eta_0$, there exists $\epsilon_2 > 0$, such that

$$\frac{(2/c_l - 1)\hat{U}_{c_l}(\eta)}{1 + 1/c_l \hat{U}_{c_l}(\eta)} < 2 - \epsilon_2.$$

Using this in (2.3.25a), we have that for $c_l \in I_0$ and $\eta > \eta_0$,

$$\hat{\Theta}'_{c_l}(\eta) \leq \frac{(2 - \epsilon_2)\hat{\Theta}_{c_l}(\eta)}{\eta}.$$

Using direct integration and Lemma 2.3.5, we have that for $c_l \in I_0$, $\eta > \eta_0$,

$$\hat{\Theta}_{c_l}(\eta) \leq C_1 \eta^{2-\epsilon_2}.$$

Using this upper bound of $\hat{\Theta}(\eta)$ in (2.3.25b), we have that for $c_l \in I_0$, $\eta > \eta_0$,

$$\hat{W}'_{c_l}(\eta) \leq \left(\frac{-1}{1 + 1/c_l \hat{U}_{c_l}(\eta)}\right) \frac{\hat{W}_{c_l}(\eta)}{\eta} + C_3 \eta^{-1-\epsilon_2}. \tag{2.3.29}$$

The first term in (2.3.29) is negative according to (2.3.26) and the second term is integrable for $\eta > \eta_0$. Then using Lemma 2.3.5, we have that for $c_l \in I_0$, $\eta > \eta_0$,

$$\hat{W}_{c_l}(\eta) < C_4.$$

Putting this upper bound in (2.3.25c) and using Lemma 2.3.5, we get that

$$\hat{U}_{c_l}(\eta) < C_5 \ln \eta, \quad c_l \in I_0, \quad \eta > \eta_0.$$

Putting this upper bound of $\hat{U}(\eta)$ back in (2.3.25b), we have that

$$\hat{W}'_{c_l}(\eta) < -\frac{C_6 \hat{W}_{c_l}(\eta)}{\eta \ln \eta} + C_3 \eta^{-1-\epsilon_2},$$

which by direct integration gives that for $c_l \in I_0$, $\eta > \eta_0$,

$$\hat{W}_{c_l}(\eta) \exp\Big(\int_{\eta_0}^{\eta} \frac{C_6}{\zeta \ln \zeta} d\zeta\Big) < C_7.$$

Thus we have that for $c_l \in I_0$ and $\eta > \eta_0$,

$$\hat{W}_{c_l}(\eta) < C_8 / \ln \eta.$$

Using this sharper upper bound of $\hat{W}(\eta)$ in (2.3.25c), we get that for $c_l \in I_0$, $\eta > \eta_0$,

$$\hat{U}_{c_l}(\eta) < C_9 \ln \ln \eta.$$

Again putting this sharper upper bound in (2.3.25b), we have that

$$\hat{W}'_{c_l}(\eta) < -\frac{C_{10} \hat{W}_{c_l}(\eta)}{\eta \ln \ln \eta} + C_3 \eta^{-1-\epsilon_2}.$$

By direct integration, we get

$$\hat{W}_{c_l}(\eta) \exp\Big(\int_{\eta_0}^{\eta} \frac{C_{11}}{\zeta \ln \ln \zeta} d\zeta\Big) < C_{12}.$$

Since $\int_{\eta_0}^{\eta} \frac{C_{11}}{\zeta \ln \ln \zeta} d\zeta > C_{13} (\ln \eta)^{\alpha} - C_{14}$ for some $\alpha \in (0, 1)$, we have that,

$$\hat{W}_{c_l}(\eta) < C_{15} \exp\big(-C_{13} (\ln \eta)^{\alpha}\big). \tag{2.3.30}$$

Note that $C_1, C_2, \ldots C_{15}$ in the above estimates are all positive constants independent of η. Using the upper bound of $\hat{W}_{c_l}(\eta)$ (2.3.30) in (2.3.25c), we conclude that $\hat{U}_{c_l}(\eta)$ converges uniformly as $\eta \to +\infty$ for $c_l \in I_0$ and complete the proof. □

To complete the proof of our main result Theorem 2.3.1, we still need to verify condition (2.3.23) for different s. And we leave this part to the next subsection.

Existence of Self-Similar Profiles

In this subsection, we verify condition (2.3.23) for $s = 2$, i.e., there exist $c_l^l, c_l^r > 2$, such that $G(c_l^l) < 0$, $G(c_l^r) > 0$, with which we can complete the proof of the existence of self-similar profiles. The following lemma allows us to verify the conditions (2.3.23) using estimates of the profiles at some finite η_0.

Lemma 2.3.6. *Consider solving equations* (2.3.25) *with initial conditions given by power series* (2.3.4)*. For some $\eta_0 > 0$, let $u_0 = \hat{U}(\eta_0)$, $\theta_0 = \hat{\Theta}(\eta_0)$, $w_0 = \hat{W}(\eta_0)$. If*

$$u_0 > 0, \tag{2.3.31a}$$

then

$$G(c_l) > 0. \tag{2.3.31b}$$

If

$$u_0 > -2, \quad u_0 + c_l w_0 + \frac{(c_l - 2)\theta_0}{(u_0 + 2)(1 + u_0/c_l)\eta_0^2} < 0, \tag{2.3.31c}$$

then

$$G(c_l) < 0. \tag{2.3.31d}$$

Proof. $G(c_l) = \lim_{\eta \to +\infty} \hat{U}(\eta)$, and $\hat{U}(\eta)$ is increasing according to (2.3.25c) and (2.3.16). So if $u_0 > 0$, then $G(c_l) > u_0 > 0$, and we finish the first part (2.3.31b).

We prove the second part (2.3.31d) by contradiction. If $G(c_l) \geq 0$, then there exists $\eta_1 \in (\eta_0, +\infty]$ such that $\hat{U}(\eta_1) = 0$, and for $\eta \in (\eta_0, \eta_1)$, $\hat{U}(\eta) > u_0$.

According to (2.3.25a) we have,

$$\hat{\Theta}'(\eta) \leq \frac{(2/c_l - 1)u_0}{1 + u_0/c_l} \frac{\hat{\Theta}(\eta)}{\eta}. \tag{2.3.32a}$$

By direct integration, we get that for $\eta \in (\eta_0, \eta_1)$,

$$\hat{\Theta}(\eta) \leq \theta_0 \eta_0^{\frac{(1-2/c_l)u_0}{1+u_0/c_l}} \eta^{\frac{(2/c_l-1)u_0}{1+u_0/c_l}}. \tag{2.3.32b}$$

Using this upper bound and the fact $\hat{U}(\eta) < 0$ for $\eta \in (\eta_0, \eta_1)$ in (2.3.25b), we get

$$(\hat{W}(\eta)\eta)' \leq \frac{1 - 2/c_l}{(1 + u_0/c_l)^2} \theta_0 \eta_0^{\frac{(1-2/c_l)u_0}{1+u_0/c_l}} \eta^{\frac{-u_0-2}{1+u_0/c_l}}. \tag{2.3.33a}$$

Since $u_0 > -2$, integrating (2.3.33a) from η_0 to η, we have that for $\eta \in (\eta_0, \eta_1)$,

$$\hat{W}(\eta)\eta \leq w_0\eta_0 + \frac{2/c_l - 1}{(1 + u_0/c_l)(u_0/c_l - u_0 - 1)} \theta_0 (\eta_0^{-1} - \eta_0^{\frac{(1-2/c_l)u_0}{1+u_0/c_l}} \eta^{\frac{-u_0-1+u_0/c_l}{1+u_0/c_l}}). \tag{2.3.33b}$$

Putting this upper bound of $\hat{W}(\eta)$ in (2.3.25c) and integrating from η_0 to η_1, we get

$$0 - u_0 = \hat{U}(\eta_1) - \hat{U}(\eta_0) \leq c_l w_0 + \frac{(c_l - 2)\theta_0}{(u_0 + 2)(1 + u_0/c_l)\eta_0^2},$$

which contradicts (2.3.31c). Then we complete the proof of this lemma. □

Next we use numerical computation together with rigorous error control to verify the condition (2.3.31a) or (2.3.31c) for different c_l

Computer programs have been used to prove several important mathematical theorems including, to name a few, the four color theorem [1], Kepler conjecture [34] and some others [53, 45, 25]. One method of computer-assisted proof is to use the interval arithmetic and inclusion principle to ensure that the output of a numerical program encloses the solution of the original problem. One first reduces the computation to a sequence of the four elementary operations, and then proceeds by replacing numbers with intervals and performing elementary operations between such intervals of representable numbers under appropriate rounding rules.

To be precise, assume that $x \in [x_{\min}, x_{\max}]$, $y \in [y_{\min}, y_{\max}]$, where $x_{\min}$, $x_{\min}$, $y_{\min}$ and $y_{\max}$ are floating point numbers that can be represented exactly on a computer. Then for one of the four elementary operations, $\odot \in \{+, -, *, /\}$, we have

$$x \odot y \in [z_{\min}, z_{\max}], \tag{2.3.34a}$$

where

$$z_{\min} = \min\{x_{\min} \underline{\odot} y_{\min}, x_{\min} \underline{\odot} y_{\max}, x_{\max} \underline{\odot} y_{\min}, x_{\max} \underline{\odot} y_{\max}\}, \tag{2.3.34b}$$

$$z_{\max} = \max\{x_{\min} \overline{\odot} y_{\min}, x_{\min} \overline{\odot} y_{\max}, x_{\max} \overline{\odot} y_{\min}, x_{\max} \overline{\odot} y_{\max}\}, \tag{2.3.34c}$$

and $\underline{\odot}$ and $\overline{\odot}$ refer to standard floating point operations with rounding modes set to 'DOWNWARD' and 'UPWARD' respectively [77]. Namely, $x \underline{\odot} y$ is the largest floating number less than $x \odot y$, and $x \overline{\odot} y$ is the smallest floating number larger than $x \odot y$. For the case that $\odot$ is division we require that $0 \notin [y_{\min}, y_{\max}]$.

The RHS of (2.3.34) involve only floating point operation, so (2.3.34) allows us to track the propagation of numerical errors using computer programs.

Using the above interval arithmetic strategy, we first numerically construct the power series (2.3.4) locally with $\Theta_s = 1$, and then extend them to some η_0 by solving the ODE system (2.3.25) to verify condition (2.3.31a) or (2.3.31c). We only illustrate this computer assisted proof procedure for the case $s = 2$ with

$c_l^l = 3, c_l^r = 8$. But the same process can be applied to other $s > 2$ to verify the existence of self-similar profiles. The computer programs used for this part of proof can be found at `https://sites.google.com/site/pengfeiliuc/home/codes`.

We first consider the case $s = 2$, $c_l = 3$, and verify that for $s = 2$, $G(3) < 0$.

Step 1 We need to control the numerical error in the local power series solutions. To numerically compute (2.3.4), we first truncate the power series to finite terms. For the case $s = 2$, $c_l = 3$, the following choice of θ^0, u^0 and r makes (2.3.13) hold:

$$u^0 = \frac{1}{9 \times 162}, \quad \theta^0 = \frac{1}{9 \times 9 \times 162}, \quad r = 162.$$

Based on (2.3.24), at $\xi = 10^{-3}$, corresponding to $\eta_s = 10^{-1}$, we have

$$\hat{U}(\eta_s) = \sum_{k=1}^{\infty} U_k \eta_s^{3k-3}, \quad \hat{\Theta}(\eta_s) = \sum_{k=2}^{\infty} \Theta_k \eta_s^{3k-1}, \quad \hat{W}(\eta_s) = \sum_{k=1}^{\infty} W_k \eta_s^{3k}. \quad (2.3.35)$$

Using estimates (2.3.14), if we truncate the power series (2.3.35) to $m = 20$ terms, the truncation errors of the three series can be bounded respectively by

$$\frac{u^0 r^{m+1} \eta_s^{3m}}{(m+1)^2(1 - r\eta_s^3)}, \quad \frac{\theta^0 (r\eta_s^3)^{m+1}}{(m+1)(1 - r\eta_s^3)\eta_s}, \quad \frac{u^0 r^{m+2} \eta_s^{3m+2}}{(m+2)(1 - r\eta_s^3)}. \quad (2.3.36)$$

Then we need to estimate the truncated power series

$$\hat{U}(\eta_s) \approx \sum_{k=1}^{20} U_k \eta_s^{3k-3}, \quad \hat{\Theta}(\eta_s) \approx \sum_{k=2}^{20} \Theta_k \eta_s^{3k-1}, \quad \hat{W}(\eta_s) \approx \sum_{k=1}^{20} W_k \eta_s^{3k}. \quad (2.3.37)$$

Using the interval arithmetic (2.3.34) strategy in each elementary operation of (2.3.12), we can inductively get computer representable intervals enclosing the values of U_k and Θ_k for all $k \leq 21$. Then we use these intervals in computing (2.3.37) to get intervals enclosing the values of the truncated power series (2.3.37). Finally we add back the the intervals (2.3.36) enclosing the truncation errors using interval arithmetic, and get intervals strictly enclosing $\hat{U}(\eta_s)$, $\hat{W}(\eta_s)$ and $\hat{\Theta}(\eta_s)$.

We denote them as

$$I^0_{\hat{U}}, \quad I^0_{\hat{W}}, \quad I^0_{\hat{\Theta}}, \quad (2.3.38)$$

and use them as initial conditions to solve (2.3.25).

We use the forward Euler scheme [56] to numerically integrate the ODE system (2.3.25). For a general ODE system with given initial data,

$$y = (y_1(x), y_2(x), \dots y_N(x))^T, \quad y'(x) = f(x, y), \quad x \in [a, b], \quad y(a) = y_0, \quad (2.3.39)$$

the forward Euler scheme discretizes the domain to finite points,

$$a = x_0 < x_1 \cdots < x_m = b$$

with step size $x_i - x_{i-1} = h$, and the numerical solutions $y_n \approx y(x_n)$ are obtained by

$$y_{n+1} = y_n + hf(x_n, y_n). \tag{2.3.40}$$

For the solution of the ODE system (2.3.39), using Taylor expansion, we have

$$y(x_{n+1}) = y(x_n) + hf(x_n, y(x_n)) + 1/2 \left(y_1''(x_1^*), y_2''(x_2^*), \ldots y_N''(x_N^*)\right)^T h^2, \tag{2.3.41}$$

where $x_i^* \in [x_n, x_{n+1}]$, for $i = 1, 2, \ldots N$. Then we have

$$y(x_{n+1}) = y_{n+1} + I_1 + I_2,$$

where

$$I_1 = \nabla_y f(x_n, y^*)(y(x_n) - y_n)h, \tag{2.3.42}$$

$$I_2 = 1/2 \left(y_1''(x_1^*), y_2''(x_2^*), \ldots y_N''(x_N^*)\right)^T h^2, \tag{2.3.43}$$

and y^* lies between y_n and $y(x_n)$. Note that I_1 is the propagation of error from the previous steps and I_2 is the local truncation error of the integration scheme.

We solve (2.3.25) from $\eta_s = 10^{-1}$ to $\eta_0 = 3$ with step size $h = 2.9 \times 10^{-6}$, and denote the node point and solutions at the n-th step as

$$\eta^n = 0.1 + nh, \quad (\hat{U}^n, \hat{W}^n, \hat{\Theta}^n)^T, \quad n = 0, \ldots, 10^6.$$

We already have $I^0_{\hat{U}}$, $I^0_{\hat{W}}$, $I^0_{\hat{\Theta}}$ (2.3.38) that enclose $\hat{U}^0$, $\hat{W}^0$, $\hat{\Theta}^0$. And we will update

$$I^n_{\hat{U}}, \quad I^n_{\hat{W}}, \quad I^n_{\hat{\Theta}}$$

step by step and make sure that they enclose $\hat{U}^n$, $\hat{W}^n$, $\hat{\Theta}^n$.

Step 2 We need to control the roundoff error in computing y_{n+1} (2.3.40). In the n-th step, we have intervals $I^n_{\hat{U}}$, $I^n_{\hat{W}}$ and $I^n_{\hat{\Theta}}$ that enclose the values of the profiles at η^n. To update these intervals, we first choose the middle points of these intervals, and use them as the numerical solution y_n. Then we use interval arithmetic to update (2.3.40) to get intervals enclosing the numerical solutions y_{n+1} at the $n+1$-th step.

Step 3 We need to control the propagation of error from previous steps, I_1. Note that the values of the profiles at η^n are enclosed in intervals $I^n_{\hat{U}}$, $I^n_{\hat{W}}$, $I^n_{\hat{\Theta}}$, and we have used

their middle points as the numerical solution y_n. So we use interval arithmetic to deduct the middle points from these intervals and get intervals enclosing $y(x_n) - y_n$ in (2.3.42). Then we need estimates of the Jacobian matrix of (2.3.25), which is

$$\frac{\partial\left(\hat{W}'(\eta),\hat{U}'(\eta),\hat{\Theta}'(\eta)\right)}{\partial(\hat{W},\hat{U},\hat{\Theta})} = \begin{pmatrix} \frac{-c_l}{c_l\eta+\hat{U}\eta} & \frac{c_l(4\hat{\Theta}-2c_l\hat{\Theta}+(c_l+\hat{U})\eta^2\hat{W})}{(\hat{U}+c_l)^3\eta^3} & \frac{c_l(c_l-2)}{(c_l+\hat{U})^2\eta^3} \\ \frac{c_l}{\eta} & 0 & 0 \\ 0 & \frac{c_l(2-c_l)\hat{\Theta}}{(c_l+\hat{U})^2\eta} & \frac{(2-c_l)\hat{U}}{c_l\eta+\hat{U}\eta} \end{pmatrix}. \tag{2.3.44}$$

Using intervals $I^n_{\hat{U}}, I^n_{\hat{W}}, I^n_{\hat{\Theta}}$ and interval arithmetic in computing (2.3.44), we can get intervals enclosing each entry of $\nabla_y f(x, y^*)$ in (2.3.42). Then using interval arithmetic in computing $\nabla_y f(x, y^*)\ (y(x_n) - y_n)$ gives us intervals enclosing I_1.

Step 4 We need to control the local truncation errors I_2 of the scheme, which are

$$\frac{1}{2}\hat{U}''(\eta_1)h^2, \quad \frac{1}{2}\hat{W}''(\eta_2)h^2, \quad \frac{1}{2}\hat{\Theta}''(\eta_3)h^2, \tag{2.3.45}$$

with $\eta_1, \eta_2, \eta_3 \in [\eta^n, \eta^{n+1}]$. According to (2.3.25), for $c_l = 3$ we have

$$\hat{W}''(\eta) = \frac{3\eta^2(3+\hat{U}(\eta))\hat{W}(\eta)(6+\hat{U}(\eta)+3\hat{W}(\eta)) - 6\hat{\Theta}(\eta)(6+2\hat{U}(\eta)+3\hat{W}(\eta))}{\eta^4(3+\hat{U}(\eta))^3}, \tag{2.3.46a}$$

$$\hat{U}''(\eta) = \frac{9\hat{\Theta}(\eta) - 3\eta^2(3+\hat{U}(\eta))(6+\hat{U}(\eta))\hat{W}(\eta)}{\eta^4(3+\hat{U}(\eta))^2}, \tag{2.3.46b}$$

$$\hat{\Theta}''(\eta) = \frac{\hat{\Theta}(\eta)\hat{U}(\eta)(3+2\hat{U}(\eta)) - 9\hat{\Theta}(\eta)\hat{W}(\eta)}{\eta^2(3+\hat{U}(\eta))^2}. \tag{2.3.46c}$$

To control I_2 (2.3.45), we need the following *a priori* estimates.

Lemma 2.3.7. *Consider the ODE system* (2.3.25) *with* $c_l > 2$ *and initial data given by power series* (2.3.4). *Assuming that at* $\eta^n > 0$, *the solutions are* $\hat{U}^n$, $\hat{W}^n$, $\hat{\Theta}^n$, *then for* $\eta \in [\eta^n, \eta^{n+1}]$, *we have the following* a priori *estimates,*

$$\hat{\Theta}(\eta) \in [\theta_{\min}, \theta_{\max}], \quad \hat{U}(\eta) \in [u_{\min}, u_{\max}], \quad \hat{W}(\eta) \in [w_{\min}, w_{\max}]. \tag{2.3.47a}$$

with

$$\theta_{\max} = \hat{\Theta}^n(\eta^{n+1}/\eta^n)^{2-c_l+sc_l}, \qquad \theta_{\min} = \hat{\Theta}^n(\eta^{n+1}/\eta^n)^{2-c_l}, \tag{2.3.47b}$$

$$u_{\min} = \hat{U}^n, \qquad w_{\max} = \hat{W}^n + \frac{s^2c_l\theta_{\max}h}{(c_l-2)(\eta^n)^3}, \tag{2.3.47c}$$

$$u_{\max} = \hat{U}^n + w_{\max}h/\eta^n, \qquad w_{\min} = \hat{W}^n - h\frac{c_l w_{\max}}{\eta_0(c_l+u_{\min})}. \tag{2.3.47d}$$

Proof. According to (2.3.25a) and the lower bound of $\hat{U}(\eta)$ (2.3.26), we have

$$\hat{\Theta}'(\eta) \leq \frac{\hat{\Theta}(\eta)}{\eta}(sc_l - c_l + 2), \quad \hat{\Theta}'(\eta) \geq \frac{\hat{\Theta}(\eta)}{\eta}(2 - c_l).$$

By direct integration, we can get $\theta_{\max}$ and $\theta_{\min}$.

$\hat{U}(\eta)$ is increasing according to (2.3.25c), so we get the lower bound $u_{\min}$. Then using the upper bound $\theta_{\max}$ and (2.3.26) in (2.3.25b), we get

$$\hat{W}'(\eta) \leq \frac{s^2 c_l \theta_{\max}}{(c_l - 2)(\eta^n)^3}. \tag{2.3.48}$$

By direct integration we get the upper bound $w_{\max}$. Putting the upper bound of $\hat{W}(\eta)$ in (2.3.25c), we get the upper bound of $\hat{U}(\eta)$, $u_{\max}$. Using the upper bound $w_{\max}$ and the lower bound $u_{\min}$ in (2.3.25b), we have

$$\hat{W}'(\eta) \geq -\frac{c_l w_{\max}}{\eta^n (c_l + u_{\min})}.$$

By direct integration we can get the lower bound of $\hat{W}(\eta)$, $w_{\min}$. □

Remark 2.3.2. The *a priori* estimates (2.3.47) that we get are relatively sharp for small h since they deviate from the values of the profiles only by $O(h)$.

We first use intervals $I^n_{\hat{U}}$, $I^n_{\hat{W}}$ and $I^n_{\hat{\Theta}}$ and the interval arithmetic in (2.3.47) to get intervals enclosing the values of the profiles in $[\eta^n, \eta^{n+1}]$. Then we can use these intervals and interval arithmetic in (2.3.46a) to get an interval enclosing the local truncation error (2.3.45), I_2.

Step 5 Finally, adding up the intervals enclosing the numerical solutions y_{n+1} (Step 2), the intervals enclosing the propagation of errors from previous steps I_1 (Step 3), and the intervals enclosing the local truncation error I_2 (Step 4), we get intervals enclosing the values of the profiles at η^{n+1}, $I^{n+1}_{\hat{W}}$, $I^{n+1}_{\hat{U}}$, I^{n+1}_{Θ}. Keep updating these intervals, we finally get estimates of the self-similar profiles at $\eta = 3$:

$$\begin{aligned}
\hat{U}(3) &\in [-1.61167791024607, -1.61167791022341], \\
\hat{W}(3) &\in [0.110808868817194, 1.10808868851010], \\
\hat{\Theta}(3) &\in [0.934100399788941, 9.34100399819680],
\end{aligned}$$

from which (2.3.31c) follows immediately, and we complete the proof that

$$G(3) < 0.$$

Remark 2.3.3. Since $\hat{W}^n$, $\hat{U}^n$ and $\hat{\Theta}^n$ are enclosed in the intervals $I^n_{\hat{W}}$, $I^n_{\hat{U}}$ and $I^n_{\hat{\Theta}}$, we can directly use interval arithmetic in (2.3.40) to get intervals enclosing $y(x_n) + hf(x_n, y(x_n))$. This strategy avoids estimating the Jacobian matrix $\nabla_y f(x, y)$, but will amplify the propagation of errors from previous steps.

Next we consider the case $s = 2$, c_l=8, and verify that for $s = 2$, $G(8) > 0$.

The verification of $G(8) > 0$ can be done in the same way. In the construction of the local solutions (2.3.4), we can easily verify that the choice of

$$u^0 = \frac{1}{6}, \quad \Theta^0 = \frac{1}{18}, \quad r = 6$$

makes the constraint (2.3.13) hold. Then we truncate the power series (2.3.4) to the first 20 terms and evaluate them at $\eta_s = 0.7$. Using the same technique as the case $c_l = 3$, we can get intervals enclosing the self-similar profiles at $\eta_s = 0.7$

$$I^0_{\hat{W}}, \quad I^0_{\hat{U}}, \quad I^0_{\hat{\Theta}}. \tag{2.3.49}$$

Then we begin to numerically solve (2.3.25) using (2.3.49). We use the same techniques as the previous case to control the numerical errors introduced in each step of the integration, and finally get intervals enclosing the profiles at $\eta = 3$:

$$\begin{aligned}
\hat{U}(3) &\in [5.66176313743309, 5.66176313745025], \\
\hat{W}(3) &\in [1.13763978495371, 1.13763978496956], \\
\hat{\Theta}(3) &\in [2.54776073991655, 2.54776074039048],
\end{aligned}$$

from which (2.3.31a) follows and we complete the proof that for $s = 2$, $G(8) > 0$.

With $G(3) < 0$, $G(8) > 0$, we conclude that there exists c_l such that the self-similar equations (3.1.5) have solutions with the leading order of $\Theta(\xi)$ at $\xi = 0$ being $s = 2$.

Remark 2.3.4. We only verify the existence of self-similar profiles for $s = 2$. But the same procedure can be applied to the cases $s > 2$ without difficulty.

Behavior of the Self-Similar Profiles at Infinity

In this subsection, we prove that the constructed self-similar profiles satisfy the matching condition (2.2.6), and that the profiles are analytic with respect to a transformed variable $\zeta = \xi^{-1/c_l}$ at $\zeta = 0$. With this we can complete the proof of Theorem 2.3.1. This far-field property of the self-similar profiles can explain the Hölder continuity of the velocity field at the singularity time.

Lemma 2.3.8. *For some $c_l > 2$ and $s \geq 2$, if the self-similar profiles constructed using power series* (2.3.4) *and extended to the whole R^+ satisfy the decay condition* (2.3.1b)*, then the profiles satisfy the matching condition* (2.2.6)*.*

After the following change of variables,

$$\zeta = \xi^{-1/c_l}, \quad \tilde{U}(\zeta) = U(\xi)\xi^{-1+1/c_l}, \quad \tilde{\Theta}(\zeta) = \Theta(\xi)\xi^{-1+2/c_l}, \quad \tilde{W}(\zeta) = W(\xi)\xi^{1/c_l}, \tag{2.3.50}$$

$\tilde{U}(\zeta)$, $\tilde{W}(\zeta)$ and $\tilde{\Theta}(\zeta)$ are analytic functions at $\zeta = 0$.

Our strategy is the following: we first prove that $\tilde{U}(\zeta)$, $\tilde{W}(\zeta)$ and $\tilde{\Theta}(\zeta)$ are smooth at $[0, +\infty)$. Then we show that there exist analytic solutions to the ODE system of $\tilde{U}(\zeta)$, $\tilde{W}(\zeta)$, $\tilde{\Theta}(\zeta)$ with the same initial conditions at $\zeta = 0$. Finally we show that smooth solutions to the ODE system of $\tilde{U}(\zeta)$, $\tilde{W}(\zeta)$, $\tilde{\Theta}(\zeta)$ with the given initial conditions are unique, with which we can complete the proof.

Proof. If the decay condition (2.3.1b) holds, then $\hat{U}(\eta)$ tends to 0 in equation (2.3.25), and there exists $\eta_0 > 0$ such that for $\eta > \eta_0$, we have

$$\frac{(2/c_l - 1)\hat{U}(\eta)}{1 + 1/c_l\hat{U}(\eta)} \in (0, 1/2).$$

Then based on (2.3.25a), we have that for $\eta > \eta_0$,

$$\hat{\Theta}'(\eta) \leq \frac{1/2\hat{\Theta}(\eta)}{\eta},$$

which implies that for $\eta > \eta_0$,

$$\hat{\Theta}(\eta) \leq C_1\eta^{1/2}. \tag{2.3.51}$$

Using this estimate in (2.3.25b), we have that for $\eta > \eta_0$,

$$(\hat{W}(\eta)\eta)' \leq C_2\eta^{-3/2},$$

which gives

$$\hat{W}(\eta)\eta < C_3. \tag{2.3.52}$$

Using the above estimate in (2.3.25c), we get that for $\eta > \eta_0$,

$$\hat{U}'(\eta) \leq C_4\eta^{-2},$$

which together with $\hat{U}(+\infty) = 0$ implies that for $\eta > \eta_0$,

$$\hat{U}(\eta) \geq -C_5\eta^{-1}. \tag{2.3.53}$$

Based on (2.3.25b) and (2.3.25c), we have

$$\hat{\Theta}'(\eta) = \frac{(2/c_l - 2)\hat{\Theta}(\eta)\hat{U}(\eta)}{\eta + 1/c_l\hat{U}(\eta)\eta}, \quad (\hat{W}(\eta)\eta)' = \frac{1/c_l\hat{U}(\eta)\hat{W}(\eta)}{1 + 1/c_l\hat{U}(\eta)} + \frac{(1 - 2/c_l)\hat{\Theta}(\eta)}{(1 + 1/c_l\hat{U}(\eta))^2\eta^2}. \tag{2.3.54}$$

Using (2.3.53), (2.3.52) and (2.3.51) in (2.3.54), we can see that $|\hat{\Theta}'(\eta)|$ and $|(\hat{W}(\eta)\eta)'|$ are both integrable from η_0 to $+\infty$, and thus $\hat{\Theta}(\eta)$ and $\hat{W}(\eta)\eta$ converge as $\eta \to +\infty$,

$$\lim_{\eta\to\infty} \hat{W}(\eta)\eta = \hat{W}_\infty \in [0, +\infty), \quad \lim_{\eta\to\infty} \hat{\Theta}(\eta) = \hat{\Theta}_\infty \in (0, +\infty). \tag{2.3.55}$$

Based on (2.3.25c) and the fact that $\hat{U}(+\infty) = 0$, we have

$$\lim_{\eta\to+\infty} \hat{U}(\eta)\eta = -c_l\hat{W}_\infty. \tag{2.3.56}$$

The above limits imply that after changing variables, $\tilde{U}(\zeta)$, $\tilde{\Theta}(\zeta)$ and $\tilde{W}(\zeta)$ are continuous for $\zeta \in [0, +\infty)$. The ODE system they satisfy for $\zeta \in (0, +\infty)$ is

$$\tilde{\Theta}'(\zeta) = \frac{(2/c_l - 1)\tilde{\Theta}(\zeta)\tilde{U}(\zeta)}{-1 - \tilde{U}(\zeta)\zeta}, \tag{2.3.57a}$$

$$\tilde{W}'(\zeta) = \frac{1/c_l\tilde{U}(\zeta)\tilde{W}(\zeta) + (1 - 2/c_l)\tilde{\Theta}(\zeta) - 1/c_l\tilde{\Theta}'(\zeta)\zeta}{-1 - \tilde{U}(\zeta)\zeta}, \tag{2.3.57b}$$

$$\tilde{U}'(\zeta) = -\frac{\tilde{U}(\zeta)}{\zeta} - \frac{c_l\tilde{W}(\zeta)}{\zeta}, \tag{2.3.57c}$$

with initial data given by (2.3.55) and (2.3.56),

$$\tilde{W}(0) = \hat{W}_\infty, \quad \tilde{\Theta}(0) = \hat{\Theta}_\infty, \quad \tilde{U}(0) = -c_l\hat{W}_\infty. \tag{2.3.57d}$$

Equation (2.3.57c) can be written as

$$\tilde{U}(\zeta) = -\frac{c_l}{\zeta}\int_0^\zeta \tilde{W}(\eta)d\eta.$$

Using a simple bootstrap argument, we can get that

$$\tilde{W}(\zeta), \tilde{\Theta}(\zeta), \tilde{U}(\zeta) \in C^\infty([0, +\infty)).$$

On the other hand, given the initial data (2.3.57d), we can construct the following power series solutions to equations (2.3.57):

$$\tilde{U}(\zeta) = -c_l\hat{W}_\infty + \sum_{k=1}^\infty \tilde{U}_k\zeta^k, \quad \tilde{W}(\zeta) = \hat{W}_\infty + \sum_{k=1}^\infty \tilde{W}_k\zeta^k, \quad \tilde{\Theta}(\zeta) = \hat{\Theta}_\infty + \sum_{k=1}^\infty \tilde{\Theta}_k\zeta^k. \tag{2.3.58}$$

Plugging these power series ansatz in (2.3.57) and matching the coefficients of ζ^k, we can uniquely determine the coefficients $\tilde{U}_k$, $\tilde{W}_k$, $\tilde{\Theta}_k$ and prove that the power series (2.3.58) converge in a small neighborhood of $\zeta = 0$. We omit the details here, because the argument is the same as in the near-field. Then to prove the analyticity of $\tilde{U}(\zeta)$, $\tilde{W}(\zeta)$ and $\tilde{\Theta}(\zeta)$ at $\zeta = 0$, we only need the uniqueness of smooth solutions to (2.3.57) with initial condition (2.3.57d). The RHS of (2.3.57c) is not Lipschitz, so the classical uniqueness result will not apply directly here.

Assume $\tilde{U}^i(\zeta)$, $\tilde{W}^i(\zeta)$, $\tilde{\Theta}^i(\zeta)$, $i = 1,2$, are two solutions to equation (2.3.57) with initial condition (2.3.57d). Let $\delta U(\zeta)$, $\delta W(\zeta)$, $\delta\Theta(\zeta)$ be their differences,

$$\delta\tilde{U}(\zeta) = \tilde{U}^1(\zeta) - \tilde{U}^2(\zeta), \quad \delta\tilde{W}(\zeta) = \tilde{W}^1(\zeta) - \tilde{W}^2(\zeta), \quad \delta\tilde{\Theta}(\zeta) = \tilde{\Theta}^1(\zeta) - \tilde{\Theta}^2(\zeta).$$

Then based on (2.3.57c),

$$\delta U(\zeta) = -\frac{c_l}{\zeta}\int_0^\zeta \delta W(\zeta)d\zeta.$$

Using Hardy inequality[30], there exists C_1 independent of ϵ such that

$$\|\delta\tilde{U}\|_{L^2([0,\epsilon])} \le C_1\|\delta\tilde{W}\|_{L^2([0,\epsilon])}.$$

Since the RHS of (2.3.57a) and (2.3.57b) are Lipschitz continuous, we have

$$|\frac{d}{d\zeta}(\delta\tilde{W}(\zeta))| + |\frac{d}{d\zeta}(\delta\tilde{\Theta}(\zeta)))| \le C_2(|\delta\tilde{W}(\zeta)| + |\delta\tilde{U}(\zeta)| + |\delta\tilde{\Theta}(\zeta)|).$$

Integrating the square of both sides on the interval $[0,\epsilon]$ and using (2.3), we get

$$\|(\delta\tilde{W}(\zeta))'\|_{L^2([0,\epsilon])} + \|(\delta\tilde{\Theta}(\zeta))'\|_{L^2([0,\epsilon])} \le C_3(\|\delta\tilde{W}(\zeta)\|_{L^2([0,\epsilon])} + \|\delta\tilde{\Theta}(\zeta)\|_{L^2([0,\epsilon])}). \tag{2.3.59}$$

Since $\delta\tilde{W}(\zeta)$ and $\delta\tilde{\Theta}(\zeta)$ vanish at $\zeta = 0$, by Poincaré-Friedrichs inequality we have

$$\|\delta\tilde{W}(\zeta)\|_{L^2([0,\epsilon])} + \|\delta\tilde{\Theta}(\zeta)\|_{L^2([0,\epsilon])} \le C_4\epsilon(\|(\delta\tilde{W}(\zeta))'\|_{L^2([0,\epsilon])} + \|(\delta\tilde{\Theta}(\zeta))'\|_{L^2([0,\epsilon])}). \tag{2.3.60}$$

The C in the above estimates are all positive constants independent of ϵ. Choosing ϵ small enough, we get a contradiction between (2.3.59) and (2.3.60), and thus

$$\tilde{W}^1 = \tilde{W}^2, \quad \tilde{U}^1 = \tilde{U}^2, \quad \tilde{\Theta}^1 = \tilde{\Theta}^2,$$

which means the solution is unique. And we complete the proof of this theorem. □

Numerical Results

In this subsection we numerically locate the root of $G(c_l)$ for several s and construct the corresponding self-similar profiles. Then we compare the obtained c_l and self-similar profiles with direct numerical simulation of the CKY model.

For any fixed $c_l > 2$, we first numerically compute the coefficients Θ_k, U_k in (2.3.4) up to $k = 50$ and determine the convergence radius of the power series using the following linear regression for $s \le k \le 50$,

$$\log \Theta_k = k \log r_1 + c_1, \quad \log U_k = k \log r_2 + c_2. \tag{2.3.61}$$

We choose $r = 1/2 \min\{1/r_1, 1/r_2\}$ and construct (2.3.4) on $[0, r/2]$.

Then we solve equation (2.2.4) from $\xi = r/2$ to $\xi = 1$ using the 4th order Runge-Kutta method with step-size $h = \frac{1-r/2}{10^4}$.

After $\xi = 1$, we make the change of variables (2.3.24) and solve the ODE system (2.3.25) from $\eta = 1$ to $\eta = 10^5$ using 4th order Runge-Kutta method with step-size $h = \frac{10^5-1}{10^6}$. We use $\hat{U}_{c_l}(10^5)$ as an approximation to $G(c_l)$.

We use the bisection method to find the root of $G(c_l)$.

After getting c_l, we construct the local self-similar profiles using power series (2.3.4) and extend them from $\xi = r/2$ to $\xi = 10$ using the explicit 4th order Runge-Kutta method with step-size $h = \frac{9}{10^4}$. Then we locate the maximum of W, which is $W_{\max} = W(\xi_0)$. For the cases that we consider, $s = 2, 3, 4, 5$, ξ_0 are all less than 10. Finally we rescale the maximum of $W(\xi)$ to $(1, 1)$, and get

$$W_s(\xi) = \frac{1}{W_{\max}} W(\xi\xi_0), \quad \xi \in [0, 1]. \tag{2.3.62}$$

We only compare the self-similar profiles W_s with direct simulation of the CKY model in this thesis, but the numerical results for the profiles Θ and U are similar.

We use a particle method in the direct simulation of the CKY model and consider $N + 1$ particles with position, density and vorticity given by

$$\begin{cases} q = (q_0(t), q_1(t), \dots q_N(t))^T, \\ \theta = (\theta_0(t), \theta_1(t), \dots \theta_N(t))^T, \\ w = (w_0(t), w_1(t), \dots w_N(t))^T. \end{cases}$$

In computing the velocity field, we use the trapezoidal rule to approximate (2.1.6),

$$u_i = -q_i \left(\sum_{j=i}^{N-1} \frac{w_j + w_{j+1}}{2} (q_{j+1} - q_j) \right).$$

In computing the driving force of w, which is θ_x, we use the three points rule:

$$(\theta_x)_i = \begin{cases} 0, & i = 0, \\ \frac{\theta_i-\theta_{i+1}}{q_i-q_{i+1}} + \frac{\theta_i-\theta_{i-1}}{q_i-q_{i-1}} + \frac{\theta_{i+1}-\theta_{i-1}}{q_{i+1}-q_{i-1}}, & 0 < i < N, \\ \frac{\theta_i-\theta_{i-2}}{q_i-q_{i-2}} + \frac{\theta_i-\theta_{i-1}}{q_i-q_{i-1}} + \frac{\theta_{i-2}-\theta_{i-1}}{q_{i-2}-q_{i-1}}, & i = N. \end{cases}$$

Initially, $10^5 + 1$ particles are equally placed in the short interval $[0, 10^{-3}]$, which are sufficient to resolve the solutions in the self-similar regime. Outside this short interval $10^5 - 10^2$ particles are equally placed. So the total number of particles is

$$N + 1 = 2 \times 10^5 - 10^2.$$

Then we need to solve the following ODE system

$$\frac{d}{dt}q = u, \quad \frac{d}{dt}w = \theta_x, \quad \frac{d}{dt}\theta = 0. \tag{2.3.63}$$

The initial condition of θ is

$$\theta(x, 0) = (1 - \cos(\pi x))^{s/2},$$

whose leading order at $x = 0$ is s.

We solve the ODE system (2.3.63) using the 4-th order Runge-Kutta method, and the time step dt is chosen adaptively to avoid particle-crossing:

$$dt_i = \frac{1}{\max(\frac{u_i-u_{i+1}}{q_{i+1}-q_i}, 0)}, \quad dt = \min(\frac{dt_i}{10}, 10^{-3}).$$

At each time step, we record the maximal vorticity $w_{\max}(t_i)$, and the position where it is attained $q_{\max}(t_i)$. According to the self-similar ansatz (2.2.2), we have

$$w_{\max}(t) = C_1(T - t)^{c_w}, \quad q_{\max}(t) = C_2(T - t)^{c_l}.$$

Thus we can compute c_l, c_w, and the singularity time T through linear regressions,

$$\left(\frac{d}{dt}\log w_{\max}(t)\right)^{-1} \approx -\frac{1}{c_w}t + \frac{T}{c_w}, \tag{2.3.64a}$$

$$\left(\frac{d}{dt}\log q_{\max}(t)\right)^{-1} \approx -\frac{1}{c_l}t + \frac{T}{c_l}. \tag{2.3.64b}$$

We compute the time derivatives of $\log w_{\max}(t)$ and $\log q_{\max}(t)$ using the center difference method, and the linear regressions (2.3.64) are done in some time interval close to the singularity time while the numerical solutions still have good accuracy.

	$s=2$	$s=3$	$s=4$	$s=5$
c_w	-0.9747	-1.0001	-1.0006	-1.0007

Table 2.1: Scaling exponent c_w obtained from direct numerical simulation.

At certain time steps close to the singularity time, t^i, $i = 1,2,3$, let w^i be the maximal vorticity at time t^i and q^i be the position the maximal vorticity is attained. We rescale the numerical solution and get the self-similar profiles of w,

$$W_s^i(\xi) = \frac{1}{w_{\max}} w(\xi q^i, t^i), \quad \xi \in [0,1]. \tag{2.3.65}$$

We compare the profiles $W_s^i(\xi)$ (2.3.65) obtained from direct simulation of the model, with $W_s(\xi)$ (2.3.62) obtained from the self-similar equations (3.1.5).

Near singularity time the velocity field seems to be Hölder continuous at the origin,

$$u(x,T) \approx Cx^\alpha.$$

Then we can determine the Hölder exponent α through linear regression

$$\ln u(x,T) \approx \ln C + \alpha \ln x. \tag{2.3.66}$$

We will compare the exponents α (2.3.66) obtained from the singular solutions, with $1 - 1/c_l$ obtained from analyzing the self-similar equations (3.1.5).

In simulating the CKY model, we choose $w(x,0)$ as

$$w(x,0) = 1 - \cos(4\pi x). \tag{2.3.67}$$

We compute the scaling exponents c_w and c_l for different leading orders of θ, $s = 2,3,4,5$, using (2.3.64a) and (2.3.64b), and the results are listed in Table 2.1 and Table 2.2. The Hölder exponents of the velocity field at the singularity time (2.3.66) and $1 - 1/c_l$ are listed in Table 2.3. The c_l that we use in computing $1 - 1/c_l$ are obtained from solving the self-similar equations.

From the Table 2.1, 2.2, 2.3, we can see that the exponents c_w we obtain from the numerical solutions are close to -1. And the c_l we obtain from the singular solution (2.3.64b) are close to those obtained from solving the self-similar equations. At the singularity time, the Hölder exponents of the velocity field are close to $1 - 1/c_l$.

For the case $s = 2$, the dependence of $G(c_l)$ on c_l is plotted in Figure 2.2. We can see that $G(c_l)$ seems to be a monotone increasing function, which implies that for

.

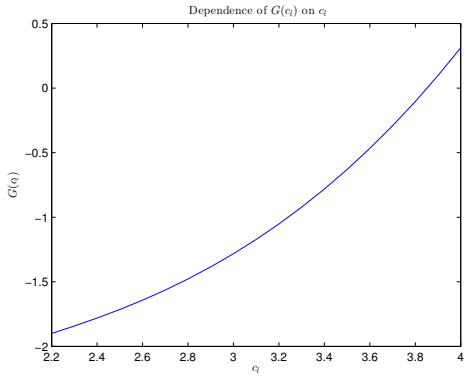

Figure 2.2: Dependence of $G(c_l)$ on c_l for $s = 2$.

	$s = 2$	$s = 3$	$s = 4$	$s = 5$
Linear Regression	3.7942	3.3143	3.1718	3.0773
Self-Similar Equations	3.7967	3.3157	3.1597	3.0841

Table 2.2: c_l got from linear regression (2.3.64b) and the self-similar equations.

	$s = 2$	$s = 3$	$s = 4$	$s = 5$
Hölder exponent	7.3381×10^{-1}	6.9823×10^{-1}	6.9131×10^{-1}	6.7610×10^{-1}
$1 - 1/c_l$	7.3661×10^{-1}	6.9841×10^{-1}	6.8351×10^{-1}	6.7576×10^{-1}

Table 2.3: Hölder exponent of the velocity field at the origin.

fixed s, the scaling exponent c_l to make the decay condition (2.3.1b) hold is unique.

The self-similar profiles that are obtained from solving the self-similar equation (2.3.62) and from direct simulation of the model (2.3.65) are plotted in Figure 2.3. The lines labeled 'exact' are obtained from solving the self-similar equation (2.3.62). Others profiles are obtained from rescaling the numerical solutions at different time steps corresponding to different maximal vorticity (2.3.65).

From Figure 2.3, we can see that after rescaling, the singular solutions at different time steps before the singularity time are very close, which implies that the solutions develop self-similar singularity. Besides, the self-similar profiles obtained from direct simulation of the model (2.3.65) agree very well with the self-similar profiles (2.3.62) we construct by solving the self-similar equations (3.1.5).

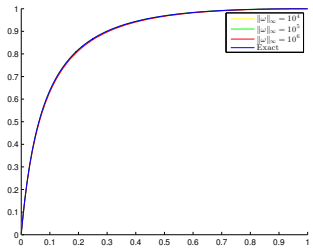

(a) The re-scaled solutions and self-similar profiles we construct. $s = 2$.

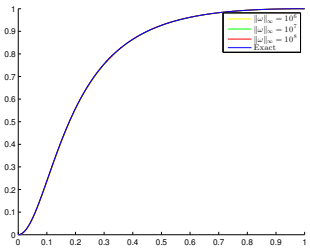

(b) The re-scaled solutions and self-similar profiles we construct. $s = 3$.

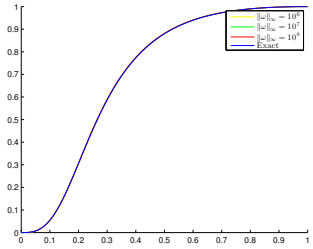

(c) The re-scaled solutions and self-similar profiles we construct. $s = 4$.

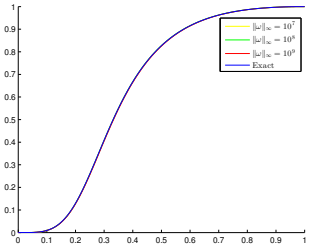

(d) The re-scaled solutions and self-similar profiles we construct. $s = 5$.

Figure 2.3: Self-similar profiles of W for $s = 2,3,4,5$.

2.4 Stability of the Self-similar Profiles

In this section, we investigate the stability of the self-similar singularity for the two 1D models through the dynamic rescaling formation.

In this thesis, we refer to "spatial profiles" as normalized solution,

$$W(t) = \frac{1}{\mu} w(\frac{x}{\lambda}, t), \quad \Theta(t) \to \frac{\lambda}{\mu^2} \theta(\frac{x}{\lambda}, t).$$

Here λ and μ are chosen based on suitable normalization conditions,

$$F(W(t), \Theta(t)) = 1, \quad G(W(t), \Theta(t)) = 1, \tag{2.4.1}$$

and the scaling is based on the scaling invariant property of the equations,

$$w(x,t) \to \frac{1}{\mu} w(\frac{x}{\lambda}, \frac{t}{\mu}), \quad u(x,t) \to \frac{\lambda}{\mu} u(\frac{x}{\lambda}, \frac{t}{\mu}), \quad \theta(x,t) \to \frac{\lambda}{\mu^2} \theta(\frac{x}{\lambda}, \frac{t}{\mu}). \tag{2.4.2}$$

We study the stability of the self-similar profiles. To be specific, we study that (1) starting from initial conditions with profiles sufficiently close to the self-similar profiles, (2) and forcing terms that decay sufficiently fast as approaching the singularity time, whether the solutions to the 1D models develop finite-time singularity with the same asymptotic structure as the self-similar ansatz.

We employ the dynamic rescaling formulation to numerically investigate the above sense of stability for the self-similar profiles in this thesis.

In the dynamic rescaling formulation, we add rescaling terms to (2.1.4) and get

$$w_t(x,t) + u(x,t)\partial_x w(x,t) + c_l(t)x\partial_x w(x,t) = \theta_x(x,t) + c_w(t)w(x,t), \quad (2.4.3a)$$

$$\theta_t(x,t) + u(x,t)\partial_x \theta(x,t) + c_l(t)x\partial_x \theta(x,t) = c_\theta(t)\theta(x,t). \quad (2.4.3b)$$

The $c_l x\partial_x$ terms correspond to stretching the solutions in the spatial direction, and the $c_w w$ and $c_\theta \theta$ terms correspond to scaling the amplitude of the solutions.

According to the scaling invariant property (2.4.2), we need to impose the following constraint on the scaling parameters in (2.4.3),

$$c_\theta(t) = c_l(t) + 2c_w(t),$$

such that the dynamic rescaling system (2.4.3) is equivalent to the two 1D models (2.1.4). To be specific, assuming that $\theta(x,t)$, $w(x,t)$, and $u(x,t)$ are smooth solutions to the 1D models (2.1.4), then correspondingly

$$\tilde{\theta}(x,t) = C_\theta(t)\theta\left(C_l(t)x, \tau(t)\right), \quad (2.4.4a)$$

$$\tilde{w}(x,t) = C_w(t)w\left(C_l(t)x, \tau(t)\right) \quad (2.4.4b)$$

are solutions to the dynamic rescaling equations (2.4.3), where

$$C_\theta(t) = \exp\left(\int_0^t c_\theta(s)ds\right), \quad (2.4.4c)$$

$$C_w(t) = \exp\left(\int_0^t c_w(s)ds\right), \quad (2.4.4d)$$

$$C_l(t) = \exp\left(\int_0^t -c_l(s)ds\right), \quad (2.4.4e)$$

$$\tau(t) = \int_0^t \exp\left(\int_0^s c_w(y)dy\right)ds. \quad (2.4.4f)$$

Let $L(t) = \exp\left(\int_0^t c_l(s)ds\right)$. For the HL-model, the solutions (2.4.4) are defined on the domain $[-L(t),\ L(t)]$, with Biot-Savart law scaled accordingly,

$$u(x) = \frac{1}{\pi}\int_0^{L(t)} w(y)\log\left|\frac{\tan\left(\frac{\pi x}{2L(t)}\right) - \tan\left(\frac{\pi y}{2L(t)}\right)}{\tan\left(\frac{\pi x}{2L(t)}\right) + \tan\left(\frac{\pi y}{2L(t)}\right)}\right| dy. \quad (2.4.5)$$

For the CKY-model, the solutions (2.4.4) are defined on $[0, L(t)]$, with

$$u(x) = -x\int_x^{L(t)} \frac{w(y)}{y}dy. \quad (2.4.6)$$

If $L(t) \to \infty$, the Biot-Savart laws (2.4.5) and (2.4.6) converge to

$$u_{HL} = \frac{1}{\pi}\int_0^\infty w(y)\log\left|\frac{x-y}{x+y}\right|dy, \tag{2.4.7a}$$

$$u_{CKY} = \frac{1}{x}\int_x^\infty \frac{w(y)}{y}dy. \tag{2.4.7b}$$

We will use (2.4.7) to close the dynamics rescaling equations (2.4.3).

We need to choose appropriate normalization conditions in (2.4.3) to fix the two rescaling parameters $c_l(t)$ and $c_w(t)$. Name, we choose $c_l(t)$, $c_w(t)$, such that

$$\frac{d}{dt}F(w(t),\theta(t)) = 0, \quad \frac{d}{dt}G(w(t),\theta(t)) = 0.$$

Our choice is to make the values of the leading order of $w(x,t)$ and $\theta(x,t)$ at the origin remain constant. We first consider the case that the leading order of $\theta(x,0)$ at the origin is 2, and choose $c_w(t)$ and $c_l(t)$ such that

$$\frac{d}{dt}w_x(0,t) = 0, \quad \frac{d}{dt}\theta_{xx}(0,t) = 0, \tag{2.4.8}$$

which according to (2.4.3) gives

$$c_l(t) = \frac{2\theta_{xx}(0,t)}{w_x(0,t)}, \quad c_w(t) = \frac{\theta_{xx}(0,t)}{w_x(0,t)} + u_x(0,t). \tag{2.4.9}$$

According to (2.4.4), solutions to the dynamic rescaling equations are simply rescaling of the solutions to the original 1D models (2.1.4). With the normalization conditions (2.4.8), we conclude that the dynamic rescaling equations govern the evolution of the spatial profiles in the solutions to the 1D models (2.1.4).

We denote the steady state of the system (2.4.3) by

$$\tilde{w}(x), \quad \tilde{\theta}(x), \quad \tilde{u}(x), \quad \tilde{c}_l, \quad \tilde{c}_w, \tag{2.4.10a}$$

and then they satisfy the following equations

$$\tilde{u}(x)\partial_x\tilde{w}(x) + \tilde{c}_l x\partial_x\tilde{w}(x) = \tilde{\theta}_x(x) + \tilde{c}_w\tilde{w}(x), \tag{2.4.10b}$$

$$\tilde{u}(x)\partial_x\tilde{\theta}(x) + \tilde{c}_l x\partial_x\tilde{\theta}(x) = (\tilde{c}_l + 2\tilde{c}_w)\tilde{\theta}(x). \tag{2.4.10c}$$

Given a steady state of (2.4.3), (2.4.10), one can correspondingly construct a set of solutions to the self-similar equations (2.2.4) using

$$c_l = -\tilde{c}_l/\tilde{c}_w,\ W(\xi) = -\frac{1}{\tilde{c}_w}\tilde{w}(\xi),\ \Theta(\xi) = \frac{1}{\tilde{c}_w^2}\tilde{\theta}(\xi),\ U(\xi) = -\frac{1}{\tilde{c}_w}\tilde{u}(\xi). \tag{2.4.11}$$

If the solutions to the original 1D models start from a steady state of the dynamic rescaling equation,

$$\tilde{c}_l, \quad \tilde{c}_w, \quad \tilde{\theta}, \quad \tilde{w},$$

then according to the transformation relation (2.4.4) we can get the blow up time

$$T = -\frac{1}{\tilde{c}_w}.$$

At time τ of the dynamic rescaling equations, the real time in the original models is

$$t = \frac{1}{\tilde{c}_w} \exp(\tilde{c}_w \tau) - \frac{1}{\tilde{c}_w}.$$

And

$$(T - t) = -\frac{1}{\tilde{c}_w} \exp(\tilde{c}_w \tau).$$

The spatial scale in the solutions is

$$C_l(t) = \exp(-c_l \tilde{\tau}).$$

And the amplitude of the solutions is

$$\|w(t)\|_\infty = C_w(t) \|\tilde{w}\|_\infty = C \exp(-c_w \tilde{\tau}).$$

Then the solutions blow up with asymptotic rate

$$\|w(t)\|_\infty = O((T - t)^{-1}), \quad C_l(t) = (T - t)^{\tilde{c}_l / \tilde{c}_w},$$

which is the blow up rate in the self-similar profiles (2.4.11).

Note that since steady state of the dynamic rescaling equations correspond to the self-similar profiles, and the dynamic rescaling equations govern the spatial profiles in the singular solutions, the stability of the self-similar profiles is equivalent to the stability of the steady state of the rescaling equations.

With Biot-Savart law (2.4.7) replacing (2.4.6) and (2.4.5), the dynamic rescaling equations (2.4.3) are not exactly equivalent to the origin 1D models (2.1.4), which are defined on a finite domain, but with perturbation terms that converge to zero. To justify the discarding of the perturbation terms due to the finite domain is indeed one of the reasons that we need stability of the self-similar profiles.

We remark that a similar formulation to (2.4.3) has been used to study the nonlinear Schrödinger equations in [60, 51, 54, 52, 64]. In those works, the dynamic rescaling formulation is used primarily as an approach to accurately solve the equations

numerically. In this thesis, we employ this dynamic formulation to investigate the stability of spatial profiles in the singular solutions. The normalization conditions that we choose in (2.4.8) are also different from those employed in the study of nonlinear Schrödinger equations, which reflects the transport nature of our model equations. In [60], the normalization condition was chosen to be the conservation of some integral norms. And it was argued in [60] that normalization using local scaling factors may be numerically unstable. However, for our problem, at the steady state, the velocity field in (2.4.3), namely, $c_l x + u(x)$, is positive near the origin, and thus the information propagates away from the origin. Our normalization conditions (2.4.8) based on local scaling factors turn out to be stable.

To demonstrate the stability, we consider adding perturbations $\delta w(x)$ and $\delta\theta(x)$ to the steady state (2.4.10). We require that the perturbations agree with the boundary conditions, symmetry and leading order properties of the equations,

$$\frac{d^2}{dx^2}\delta\theta(0) = 0, \quad \frac{d}{dx}\delta w(0) = 0. \tag{2.4.12}$$

The above constraints on the derivatives are in general difficult to impose numerically, and for convenience, we introduce the following change of variables,

$$w(x,t) = x\hat{w}(x,t), \quad \theta(x,t) = x^2\hat{\theta}(x,t), \quad u(x,t) = x\hat{u}(x,t). \tag{2.4.13}$$

With this change of variables, the equations (2.4.3) become

$$\hat{w}_t + (-c_w(t) + c_l(t))\hat{w} + \hat{u}\hat{w} + (c_l(t)x + \hat{u}(x,t)x)\hat{w}_x = 2\hat{\theta} + x\hat{\theta}_x, \tag{2.4.14a}$$

$$\hat{\theta}_t + (-2c_w(t) + c_l(t))\hat{\theta} + 2\hat{u}\hat{\theta} + (c_l(t)x + \hat{u}(x,t)x)\hat{\theta}_x = 0. \tag{2.4.14b}$$

Correspondingly, the Biot-Savart laws become

$$\hat{u}_{CKY}(x) = -\int_x^\infty \hat{w}(y)dy, \quad \hat{u}_{HL}(x) = \frac{1}{\pi}\int_0^\infty \frac{x}{y}\log\left|\frac{x-y}{x+y}\right|\hat{w}(y)dy. \tag{2.4.14c}$$

The constraints (2.4.12) on the perturbations become

$$\delta\hat{\theta}(0) = 0, \quad \delta\hat{w}(0) = 0. \tag{2.4.14d}$$

Initially we choose $\hat{\theta}(0,0) = \hat{w}(0,0) = 1$, and then (2.4.9) leads to

$$c_l(t) = 4, \quad c_w(t) = \hat{u}(0,t) + 2. \tag{2.4.14e}$$

We will use the dynamic rescaling system (2.4.14) in the next two subsections to study the self-similar profiles of the CKY and the HL-model separately.

The CKY-Model

In this subsection we numerically investigate the linearized stability of the steady state of the dynamics rescaling equations (2.4.14).

Recall that the dynamic rescaling equations (2.4.14) are defined on the whole real line R^+. So to conduct numerical simulation, we first restrict the equations (2.4.14) to a fixed finite interval $[0, M]$. Note that the velocity field (2.4.14c) $\hat{u}$ depends on the $\hat{w}$ on the whole R^+, so we need to truncate $\hat{w}$ to the fixed interval $[0, M]$ to close the system. For this purpose, we introduce the following linear projection operator,

$$P[F(x)] = F(x) - \frac{x^2}{M^2} F(M), \quad x \in [0, M]. \tag{2.4.15}$$

With the truncation operator P, the dynamic rescaling equations (2.4.14) become

$$\hat{w}_t = P[2\hat{\theta} + x\hat{\theta}_x - (c_l + c_w)\hat{w} - \hat{u}\hat{w} - (c_l x + \hat{u}x)\hat{w}_x], \tag{2.4.16a}$$

$$\hat{\theta}_t = -(2c_w - c_l)\hat{\theta} - 2(c_l + u)\hat{\theta} - (c_l x + \hat{u}x)\hat{\theta}_x, \tag{2.4.16b}$$

$$\hat{u}(x,t) = -\int_x^M \hat{w}(y,t)dy. \tag{2.4.16c}$$

The projection operator P in (2.4.16a) guarantees that $w(x,t)$ remains continuous and vanishes outside the domain $[0, M]$. Based on the far-field decay conditions of these self-similar profiles (2.2.6), one can easily see that

$$\lim_{M\to\infty} \int_M^\infty \frac{W(\xi)}{\xi} d\xi \to 0,$$

which justifies the truncation and projection introduced in (2.4.16).

The dynamic rescaling equations (2.4.16) are essentially an iteration scheme, and we need appropriate initial conditions so that the solutions converge to the steady states. We use the spatial profiles obtained from direct numerical simulation of the CKY model close to the singularity time as the initial conditions for (2.4.16).

In our computation, we choose

$$M = 1.6 \times 10^9$$

in the truncation (2.4.15). To discretize the spatial domain $[0, M]$, we first divide it into the inner region $[0, 16]$ and outer region $[16, M]$. In the inner region, we use a uniform mesh of size $h = 16/N_1$, and denote the nodal points as x_i,

$$x_i = ih, \quad i = 0, 1, \cdots, N_1. \tag{2.4.17}$$

In the outer region, according to the far-field properties of the profiles that we obtained in the previous section, the profiles have slow variation and are smooth with the transformed variable $\eta = \xi^{-1/c_l}$, so we will use a coarser mesh to reduce the computational cost. We consider a transformed variable $\xi = x^{-1/4}$, and for $x \in [16, 1.6 \times 10^9]$, we have $\xi \in [5 \times 10^{-3}, 1/2]$. We put a uniform mesh of size $\tilde{h} = \frac{1}{2N_2}$ on the ξ-space, and get

$$\xi_i = 1/2 - (i - N_1)h, \quad i = N_1 + 1, N_1 + 2, \cdots, \frac{99}{100}N_2 + N_1 = N. \tag{2.4.18}$$

Then we map ξ_i back to the x-space, and get the nodal points in the outer region,

$$x_i = (\xi_i)^{-4}, \quad N_1 + 1, \cdots, N = N_1 + \frac{99}{100}N_2.$$

In the discretization of the spatial derivatives in (2.4.16), we use the upwind scheme,

$$\hat{\theta}_x(x_i) \approx \frac{\hat{\theta}(x_i) - \hat{\theta}(x_{i-1})}{x_i - x_{i-1}}, \quad \hat{w}_x(x_i) \approx \frac{\hat{w}(x_i) - \hat{w}(x_{i-1})}{x_i - x_{i-1}}. \tag{2.4.19}$$

In the temporal direction, we use the forward Euler scheme and choose time step,

$$dt = \min_i \frac{x_i - x_{i-1}}{\hat{u}(x_i)x_i + c_l x_i}. \tag{2.4.20}$$

With the above discretization and the choice of initial conditions, we observe that the solutions to (2.4.16) converge to their steady states. For the choice that $N_1 = 2000$, $N_2 = 4000$ in (2.4.17) and (2.4.18), we obtain that at the steady state,

$$\tilde{c}_l = 4, \quad \tilde{c}_w \approx -1.0586.$$

According to (2.4.11), we get the corresponding self-similar profiles with

$$c_l = -\tilde{c}_l/\tilde{c}_w \approx 3.7785. \tag{2.4.21}$$

This c_l agrees with our numerical solution of the self-similar equations $c_l = 3.7967$ in the previous subsection.

Next we locate the maximum of the steady state profile $\tilde{w}(\xi)$ (2.4.10), which is $\tilde{w}_{\max} = \tilde{w}(\xi_0)$, and rescale the maximum to $(1, 1)$, and get the rescaled profile $W(\xi)$

$$W(\xi) = \frac{1}{\tilde{w}_{\max}}\tilde{w}(\xi_0\xi). \tag{2.4.22}$$

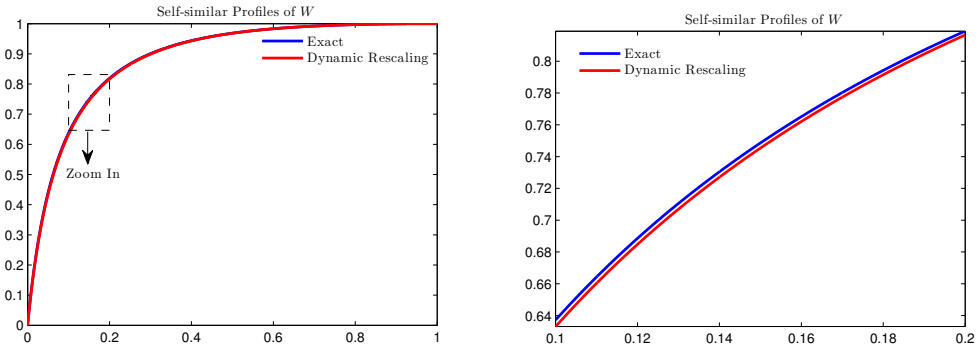

(a) Self-similar profiles of W.

(b) Profiles of W (zoom in).

Figure 2.4: The self-similar profiles obtained from (2.4.14) and (2.2.4).

The rescaled self-similar profile (2.4.22) is plotted in Figure 2.4 together with the one obtained from solving the self-similar equation (2.2.4). We can see that there is very small discrepancy between the two profiles. The small difference in c_l (2.4.21) and the resulting self-similar profile of $W(\xi)$ (2.4.22) imply that the error introduced by the truncation (2.4.15) and spatial discretization (2.4.19) is small.

Next, we consider the stability of the steady states (2.4.10). We denote

$$\hat{w} = (\hat{w}_0, \hat{w}_1, \cdots \hat{w}_N), \quad \hat{u} = (\hat{u}_0, \hat{u}_1, \cdots u_N), \quad \hat{\theta} = (\hat{\theta}_0, \hat{\theta}_1, \cdots \hat{\theta}_N), \tag{2.4.23}$$

where $\hat{w}_i = \hat{w}(x_i)$, $\hat{u}_i = \hat{u}(x_i)$, $\hat{\theta}_i = \hat{\theta}(x_i)$. The equations (2.4.16) after the spatial discretization (2.4.19) become an ODE system of $\hat{w}$ and $\hat{\theta}$,

$$\frac{d}{dt}(\hat{w}, \hat{\theta})^T = F(\hat{w}, \hat{\theta}) = (PF^w(\hat{w}, \hat{\theta}), F^\theta(\hat{w}, \hat{\theta}))^T, \tag{2.4.24}$$

where P corresponds to the projection operator (2.4.15), and F^w, F^θ correspond to the right hand side of (2.4.16a) and (2.4.16b). F^w and F^θ are given by

$$F_i^w = (c_w - c_l)\hat{w}_i - \hat{u}_i\hat{w}_i - (c_l x_i + \hat{u}_i x_i)\frac{\hat{w}_i - \hat{w}_{i-1}}{x_i - x_{i-1}} + 2\hat{\theta}_i + x_i\frac{\hat{\theta}_i - \hat{\theta}_{i-1}}{x_i - x_{i-1}}, \tag{2.4.25}$$

$$F_i^\theta = (2c_w - c_l)\hat{\theta}_i - 2\hat{u}_i\hat{\theta}_i - (c_l x_i + \hat{u}_i x_i)\frac{\hat{\theta}_i - \hat{\theta}_{i-1}}{x_i - x_{i-1}}. \tag{2.4.26}$$

The velocity $\hat{u}_i$ and scaling parameter c_w are functions of $\hat{w}_i$,

$$\hat{u}_i = -\sum_{j=i}^{N-1} \frac{\hat{w}_j + \hat{w}_{j+1}}{2}(x_{j+1} - x_j), \tag{2.4.27}$$

$$c_w = 2 + \sum_{i=0}^{N-1} \frac{\hat{w}_i + \hat{w}_{i+1}}{2}(x_{i+1} - x_i). \tag{2.4.28}$$

Denote the steady state as $\hat{w}^*, \hat{\theta}^*$, then we compute the Jacobian of F (2.4.24) with respect to $(\hat{w}, \hat{\theta})$ at the steady state, namely,

$$\nabla_{\hat{w},\hat{\theta}} F(\hat{w}^*, \hat{\theta}^*). \tag{2.4.29}$$

The entries of the Jacobian (2.4.29) can be computed from

$$\frac{\partial F_i^w}{\partial \hat{w}_j} = (c_w - c_l + \hat{u}_i - \frac{c_l x_i + \hat{u}_i x_i}{x_i - x_{i-1}})\delta_{ij} + \hat{w}_i \frac{x_{j+1} - x_j}{2} + (\hat{w}_i - x_i \frac{\hat{w}_i - \hat{w}_{i-1}}{x_i - x_{i-1}}) \frac{\partial \hat{u}_i}{\partial \hat{w}_j}, \tag{2.4.30a}$$

$$\frac{\partial F_i^w}{\partial \hat{\theta}_j} = (2 + \frac{x_i}{x_i - x_{i-1}})\delta_{ij} - \frac{x_i}{x_i - x_{i-1}} \delta_{j,i-1}, \tag{2.4.30b}$$

$$\frac{\partial F_i^\theta}{\partial \hat{w}_j} = 2\hat{\theta}_i \frac{\partial c_w}{\partial \hat{w}_j} + (-2\hat{\theta}_i - x_i \frac{\hat{\theta}_i - \hat{\theta}_{i-1}}{x_i - x_{i-1}}) \frac{\partial \hat{u}_i}{\partial \hat{w}_j}, \tag{2.4.30c}$$

$$\frac{\partial F_i^\theta}{\partial \hat{\theta}_j} = (2c_w - c_l - 2\hat{u}_i - \frac{c_l x_i + \hat{u}_i x_i}{x_i - x_{i-1}})\delta_{i,j} + \frac{c_l x_i + \hat{u}_i x_i}{x_i - x_{i-1}} \delta_{i-1,j}, \tag{2.4.30d}$$

where

$$\frac{\partial c_w}{\partial \hat{w}_j} = \frac{x_{j+1} - x_{j-1}}{2}, \tag{2.4.31a}$$

$$\frac{\partial \hat{u}_i}{\partial \hat{w}_j} = 1_{j \geq i} \frac{x_{j+1} - x_j}{2} + 1_{j \geq i+1} \frac{x_j - x_{j-1}}{2}. \tag{2.4.31b}$$

With the above explicit formula of $\nabla_{\hat{w},\hat{\theta}} F(\hat{w}^*, \hat{\theta}^*)$, we compute its eigenvalues. For $N_1 = 1000$, $N_2 = 2000$, the first several eigenvalues of (2.4.29) are plotted in Figure 2.5a.

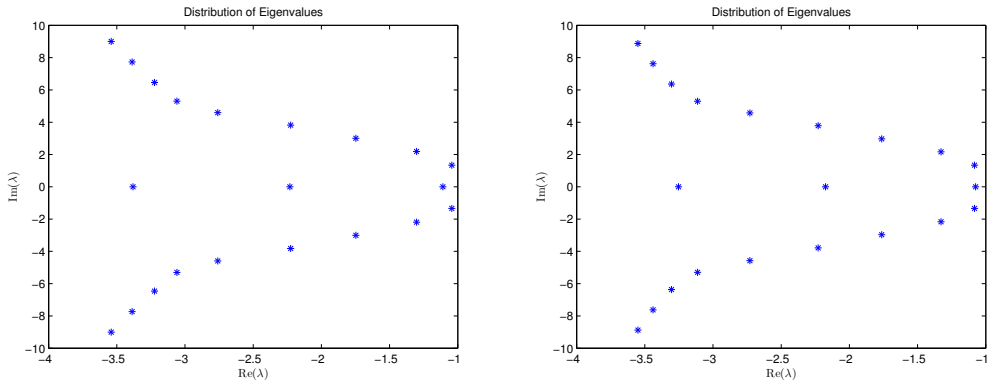

(a) Coarse mesh. (b) Fine mesh.

Figure 2.5: Leading eigenvalues of the Jacobian matrix (2.4.29).

We can see that the maximal real part of the eigenvalues is negative,

$$\mathrm{Re}(\lambda_1) \approx -1.0745.$$

The classical dynamic system theory [66] implies that the discretized dynamics (2.4.24) of rescaling equations (2.4.16) are asymptotically stable near its steady state.

To demonstrate the accuracy of our computation, we use a finer spatial mesh with $N_1 = 2000$, $N_2 = 4000$ in (2.4.17), (2.4.18). We compute the eigenvalues of the Jacobian (2.4.29) for this refined system at its steady state, and the first several of them are plotted in Figure 2.5b. We can see that after refinement, the first several eigenvalues of the Jacobian remain the same. This implies that the negativity of the eigenvalues of (2.4.29) is not a numerical discretization artifact, and the dynamic rescaling equations (2.4.3) has a stable steady state. Correspondingly, we obtain that the self-similar profiles (2.4.11) are asymptotically stable.

Before we end this subsection, we want to comment that the stability that we demonstrate here does not mean that after a small perturbation in the initial conditions of the system (2.1.4), the perturbed solutions will finally converge to the original solutions (2.2.2). Actually, the solutions to the 1D model are highly unstable, and develop singularity in finite time. And a small perturbation will result in a different singularity time T. However, our numerical results suggest that the normalized profiles in the singular solutions will converge, namely, the spatial profiles in the singular solutions enjoy some stability. In another word, there is some stability for the highly unstable (singular) solutions, i.e., stability of instability.

The HL-Model

In this subsection, we consider the self-similar singularity of the HL-model (2.1.4) and (2.1.5). Because of the non-local nature of the Biot-Savart law (2.1.5), the techniques that we employ to prove the self-similar singularity of the CKY model will not apply. For the HL-model, we first simulate the model (2.1.4) numerically and obtain the scaling exponents and self-similar profiles based on the direct numerical simulation. Then we solve the dynamic rescaling equations (2.4.14) and compare the profiles and exponents obtained from the steady state (2.4.11) of (2.4.3) with those obtained from direct numerical simulation of the HL-model. Finally we demonstrate the stability of these self-similar profiles using linearization.

The singularity of the HL-model takes place at the origin, and to efficiently resolve the singularity of the solution, a very fine mesh is required. To save computational

cost, we employ a moving mesh method introduced in [58], which adaptively puts a certain portion of the grid points in the singular region.

We first construct an analytic mesh mapping function $x(s)$ with derivative given by

$$x_s(s) = a + \frac{\beta}{\alpha\sqrt{\pi}} e^{-\frac{(1-s)^2}{\alpha^2}}. \tag{2.4.32}$$

$x(s)$ maps from $s \in [0,1]$ to $x \in [0,1]$, and a, α, β are parameters that will be chosen dynamically. Note that $x_s(s)$ is even at $s = 1$, and thus this map (2.4.32) preserves the symmetry of the solutions at $x = 1$. For α small, $x_s(s) \approx a$ for s near 0 due to the fast decay of the exponential function, and thus x_s is approximately even at $s = 0$, and the map $x(s)$ also preserves symmetry at $s = 0$.

We use an uniform mesh in the s-space with nodal points,

$$s_j = jh, \quad j = 0,2,\cdots N, \quad h = \frac{1}{N}, \tag{2.4.33}$$

which correspond to $x_j = x(s_j), j = 0,\cdots N$ in the physical space.

Preliminary simulation suggests that the profile of w in the singular solutions to the HL-model is similar to that of the CKY-model, and takes the shape of a bump. So we define the singular region $\mathcal{S}(t)$ as

$$\mathcal{S}(t) = \{x | 0 < x < x(2M(t))\}, \tag{2.4.34}$$

where $M(t)$ is position at which the maximum of w is attained in the s-space.

In our simulation of the HL-model, we choose the following initial condition,

$$w(x,0) = \sin(\pi x), \quad \theta(x,0) = 1000 - 1000\cos(\pi x).$$

We initially choose $a = 1$, $\beta = 0$, $\alpha = \frac{1}{3}$, and will adjust the parameters to make sure that $[\delta_1, \delta_2]$ portion of the nodal points are placed in the singular region.

To be specific, we fix $\alpha = 1/3$, and choose $\delta_1 = 1/5$, $\delta_2 = 1/2$. With this choice we can see that the exponential part of $x_s(s)$ is small for $s < 1/2$ due to fast decay of exponential function, which means $u_s(s) \approx a$ for $s \leq 1/2$.

At time t_0, if the portion of nodal points in the singular region drops below δ_1, we modify the parameters, and choose a based on

$$a\delta_2 = x(2M(t_0)),$$

which guarantees that x approximately maps $[0,\delta_2]$ to $\mathcal{S}(t_0)$. Besides, we need

$$x(1) = a + \int_0^1 \frac{\beta}{\alpha\sqrt{\pi}} e^{-\frac{(1-x(t))^2}{\alpha^2}} dt = 1,$$

and consequently β can be determined as $\beta = \frac{2-2a}{\mathrm{erf}(1/\alpha)}$.

Every time we adjust the parameters, we reconstruct $w(s,t)$ and $\theta(s,t)$ using interpolation in the s-space. Our numerical results show that the map (2.4.32) with appropriate parameters can resolve the singularity of the solutions.

In the s-space, based on (2.1.5), we have

$$u_x(x(s)) = \text{P.V.}\ \frac{1}{2}\int_{-1}^{1} w(x(t))\cot[\frac{\pi}{2}(x(s)-x(t))]x_s(t)dt,\quad s\in[0,1], \tag{2.4.35}$$

$$= \frac{1}{2}\int_{-1}^{1} w(x(t))x_s(t)[\cot(\frac{\pi}{2}(x(s)-x(t))) - \frac{1}{x_s(s)}\cot(\frac{\pi}{2}(s-t))]dt, \tag{2.4.36}$$

$$+ \text{P.V.}\ \frac{1}{2}x_s(s)\int_{-1}^{1} w(x(t))x_s(t)\cot(\frac{\pi}{2}(s-t))dt. \tag{2.4.37}$$

We denote (2.4.36) as I_1, and denote (2.4.37) as I_2. I_2 is the Hilbert transform of $w(x(s))x_s(s)$, and since we have a uniform mesh on the s-space, we can compute I_2 efficiently using FFT. For I_1, the integrand is continuous, and we have

$$\lim_{t\to s} w(x(t))x_s(t)[\cot(\frac{\pi}{2}(x(s)-x(t))) - \frac{1}{x_s(s)}\cot(\frac{\pi}{2}(s-t))] = w(x(s))\frac{x_{ss}(s)}{\pi}. \tag{2.4.38}$$

We use the trapezoidal rule to compute the integral in the first part I_1, which is known to have spectral accuracy for smooth periodic functions.

In the s-domain, the equations (2.1.4) become

$$\theta_t + u\frac{\theta_s}{x_s(s)} = 0, \tag{2.4.39a}$$

$$w_t + u\frac{w_s}{x_s(s)} = \frac{\theta_s}{x_s(s)}. \tag{2.4.39b}$$

We use a 6-th order finite difference scheme to discretize θ_s, w_s,

$$f_s(x_i) \approx \frac{-1}{60h}f(x_{i-3}) + \frac{3}{20h}f(x_{i-2}) - \frac{3}{4h}f(x_{i-1}) + \frac{3}{4h}f(x_{i+1}) - \frac{3}{20h}f(x_{i+2}) + \frac{1}{60h}f(x_{i+3}).$$

In the temporal direction, we use the 4th order explicit Runge Kutta method.

The time step dt is chosen such that

$$adt = 0.9h, \quad a = \max|\frac{u}{x_s(s)}|.$$

The simulation will be terminated once the minimal mesh size in the physical space gets below 10^{-15}. We choose $N = 2000$ and the rescaled solution $w(x,t)$ at different time steps corresponding to different $\|w\|_\infty$ are plotted in Figure 2.6.

From the figure we can see that the rescaled solutions are very close at different time steps, which implies the solutions develop self-similar singularity.

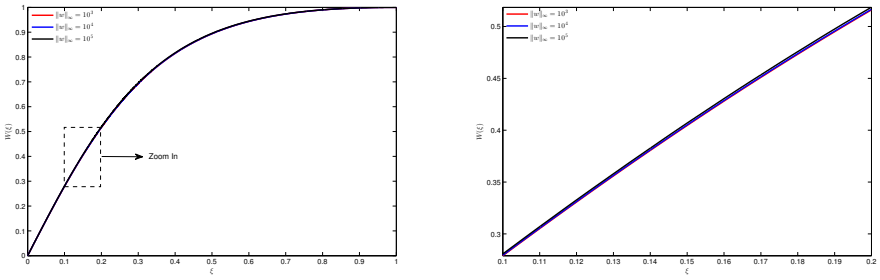

(a) Solutions of $w(x,t)$. (b) Zoom in.

Figure 2.6: The rescaled solutions W at different time steps close to singularity.

In our simulation we track the maximal vorticity $w_{\max}(t)$ and the position at which the maximum is attained, $l(t)$. They are obtained in each time step using a 6-th order polynomial interpolation. We also track $\frac{d\|w\|_\infty}{dt}$ at each time step,

$$\frac{d\|w\|_\infty}{dt} = \theta_x(l(t),t).$$

Based on (2.2.2), we have

$$w_{\max}(t) \approx C(T-t)^{c_w}, \quad l(t) \approx C(T-t)^{c_l}. \tag{2.4.40}$$

We can obtain the singular time T and c_w using linear regression,

$$\left(\frac{d}{dt}\log(\|w(x,t)\|_\infty)\right)^{-1} \approx \frac{t}{c_w} - \frac{T}{c_w}, \tag{2.4.41}$$

where $\frac{d}{dt}\log(\|w(x,t)\|_\infty)$ can be computed from

$$\frac{d}{dt}\log(\|w(x,t)\|_\infty = \frac{1}{\|w(x,t)\|_\infty}\frac{d}{dt}\|w\|_\infty.$$

$\frac{d}{dt}\log(\|w(x,t)\|_\infty$ and the line fitting region are plotted in Figure 2.7.

The linear regression (2.4.41) in the fitting zone $t \in [0.0373, 0.0374]$ gives us

$$c_w \approx -0.9378, \quad T \approx 3.7444 \times 10^{-2}.$$

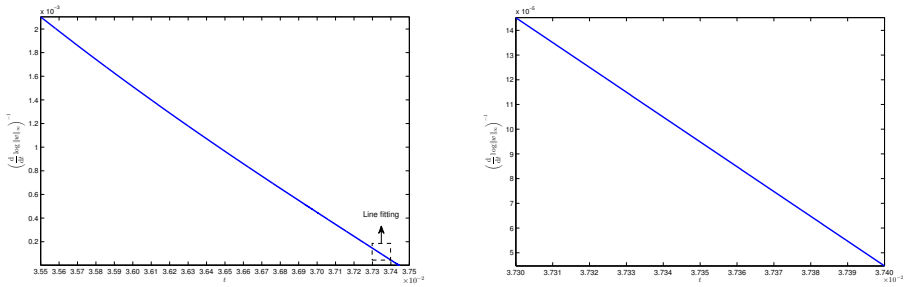

(a) $\frac{d}{dt}\log(\|w(x,t)\|_\infty$ and t. (b) The regression region.

Figure 2.7: The line fitting to determine c_w and the singularity time T.

We can see that the c_w we obtain is very close to -1, as predicted by (2.2.3).

With the singularity time T obtained from (2.4.41) and using (2.4.40), we can obtain c_l from the following linear regression, where $\log(T-t)$ and $\log(l(t))$ are explanatory and dependent variables respectively,

$$\log(l(t)) \approx \log C + c_l \log(T-t). \tag{2.4.42}$$

We plot $\log(l(t))$ over the line fitting zone $t \in [0.0373, 0.0374]$ in Figure 2.8.

From the figure we can see that the curve is very close to a straight line, which implies the validity of the scaling law (2.4.40). And the linear regression gives

$$c_l \approx 2.9800. \tag{2.4.43}$$

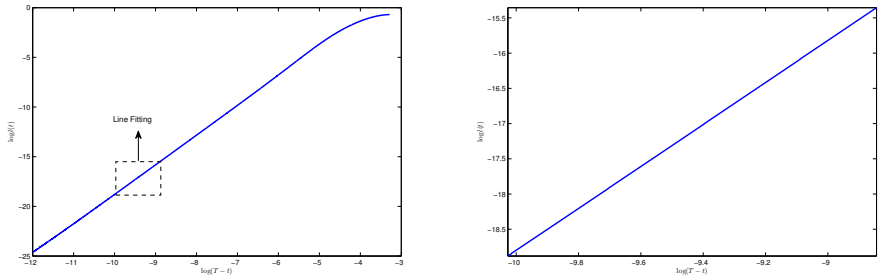

(a) $\log(l(t))$ and $\log(T-t)$. (b) The regression region.

Figure 2.8: The line fitting to determine c_l.

At time $t = 0.0374$ which is endpoint of the line fitting zone that we choose in (2.4.41) and (2.4.42), the solution $w(s,t)$ is plotted in Figure 2.9. From the figure,

we can see that the solution remains smooth with respect to the variable s until close to the singularity time T, and this implies that the moving mesh method can resolve the singularity of the solutions of the HL-model very well.

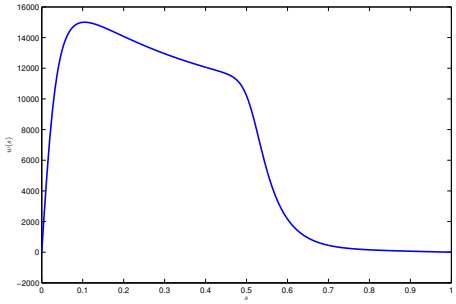

Figure 2.9: The configuration of w with respect to s at $t = 0.0374$.

Then we investigate the stability of the profiles in the HL-model using the dynamic scaling equations (2.4.14) as for the CKY model in the previous subsection.

In the spatial discretization, we first restrict the computational domain of (2.4.14) to $[0, M]$ with $M = 10^5$. Since the velocity field $\hat{u}(x,t)$ (2.4.14c) depends on the $\hat{w}(x,t)$ on the whole R^+, we need to truncate the solution $\hat{w}(x,t)$ using the projection operator (2.4.15). To be specific, the Biot-Savart law (2.4.14c) becomes

$$\hat{u}(x) = \frac{1}{\pi}\int_0^M \frac{y}{x}\log\left|\frac{x-y}{x-y}\right|\hat{w}(y)dy, \quad x \in [0,M], \tag{2.4.44}$$

and the equation for $\hat{w}(x,t)$ (2.4.14a) becomes

$$\hat{w}_t = P[2\hat{\theta} + x\hat{\theta}_x - (c_l + c_w)\hat{w} - \hat{u}\hat{w} - (c_l x + \hat{u}x)\hat{w}_x]. \tag{2.4.45}$$

The truncation operator P preserves the symmetries of the HL-model at the origin.

In the discretization of the spatial domain, we put N_1+1 nodal points on the interval $[0,16]$, which is the inner region

$$x_i = ih, \quad i = 0,1,\cdots N_1, \quad h = \frac{1}{16N_1}.$$

And in the outer region, we introduce a map $\xi = \log x$, and denote

$$\xi_i = \log(\frac{1}{16}) + (i - N_1)h, \quad i = N_1+1,\cdots N_1+N_2, \quad h = \frac{\log(M) - \log(\frac{1}{16})}{N_2}.$$

Then we get the outer region nodal points

$$x_i = \exp(\xi_i), \quad i = N_1 + 1, \cdots N_1 + N_2.$$

We denote the mesh size as

$$h_i = x_{i+1} - x_i.$$

We use the same notations (2.4.23) for the discretized dynamics as in the CKY-model. In computing the spatial derivatives in (2.4.16), we use the upwind scheme,

$$\hat{w}_x(x_i) \approx \frac{\hat{w}(x_i) - \hat{w}(x_{i-1})}{h_i}, \quad \hat{\theta}_x(x_i) \approx \frac{\hat{\theta}(x_i) - \hat{\theta}(x_{i-1})}{h_i}.$$

In computing the velocity field using (2.4.7), we need to be careful since it involves singular integral operators. Our strategy is the following: we first interpolate $\hat{w}(x)$ using a piece-wise linear function, and on each interval $[x_i, x_{i+1}]$ we have

$$\hat{w}(x) = \hat{w}_{i-1} + \frac{\hat{w}_i - \hat{w}_{i-1}}{h_i}(x - x_{i-1}), \quad x \in [x_{i-1}, x_i].$$

With the above interpolation of $\hat{w}(x,t)$, we compute the velocity field according to (2.4.14c) explicitly. In another word, we only discretize the vorticity field, and do not discretize the singular kernel in the Biot-Savart law (2.4.7).

To be specific, we denote

$$\begin{aligned}
S^1_{i,j} &= \frac{1}{2h_i x_i}\left[\left(\frac{y^3}{3} - \frac{y^2}{2}x_{j-1} - \frac{x_i^3}{3} + \frac{x_i^2}{2}x_{j-1}\right)\log|x_i - y|\right]\Big|_{y=x_{j-1}}^{x_j}, \\
S^2_{i,j} &= \frac{-1}{2h_i x_i}\left[\left(\frac{y^3}{3} - \frac{y^2}{2}x_{j-1} + \frac{x_i^3}{3} + \frac{x_i^2}{2}x_{j-1}\right)\log|x_i + y|\right]\Big|_{y=x_{j-1}}^{x_j}, \\
S^3_{i,j} &= \frac{-1}{2h_{i+1} x_i}\left[\left(\frac{y^3}{3} - \frac{x_{j+1}y^2}{x} + \frac{x_i^2}{2}x_{j+1} - \frac{x_i^3}{3}\right)\log|x_i - y|\right]\Big|_{y=x_j}^{y=x_{j+1}}, \\
S^4_{i,j} &= \frac{1}{2h_{i+1} x_i}\left[\left(\frac{y^3}{3} - \frac{x_{j+1}^2}{2}y^2 + \frac{x_i^3}{3} + \frac{x_{j+1}x_i^2}{2}\right)\log|x_i + y|\right]\Big|_{y=x_j}^{y=x_{j+1}}.
\end{aligned}$$

And by a direct calculation, we get

$$\hat{u}(x_i) = \sum_j (S^1_{i,j} + S^2_{i,j} + S^3_{i,j} + S^4_{i,j} + \frac{x_{j-1}}{6} - \frac{h_i x_i}{6} - \frac{x_{j+1}}{6} - \frac{h_{i+1}x_i}{6})\hat{w}_j. \quad (2.4.46)$$

In the temporal direction, we use the forward Euler scheme, which is the same as that in the CKY-model, and choose the time step dt according to the CFL condition (2.4.20). To simulate the dynamic rescaling equations (2.4.14), we need an

appropriate initial condition. We cannot solve the steady state equations (2.4.10) using the shooting method as we did for the CKY-model because of the nonlocal nature of the Biot-Savart law (2.4.14c). Considering the close connection of the two models, we use the self-similar profiles of the CKY-model as the initial condition to simulate dynamic rescaling equation of the HL-model.

In our numerical simulation, the solutions to (2.4.14) converge to a steady state. For $N_1 = 2000$, $N_2 = 4000$, at the steady state, we have

$$\tilde{c}_l = 4, \quad \tilde{c}_w = -1.3516.$$

Then according to (2.4.11), we get a set of self-similar profiles with

$$c_l = -\frac{\tilde{c}_l}{\tilde{c}_w} = 2.9596.$$

This c_l agrees with the one we obtained from the direct simulation of the model (2.4.43).

The rescaled steady state solution W (2.4.11) is plotted in Figure 2.10, together with the self-similar profiles obtained from direct simulation. From the figure we can see that the error in the self-similar profile of w is small, which implies that the errors introduced in the truncation (2.4.44), (2.4.45) and discretization (2.4.19) are small.

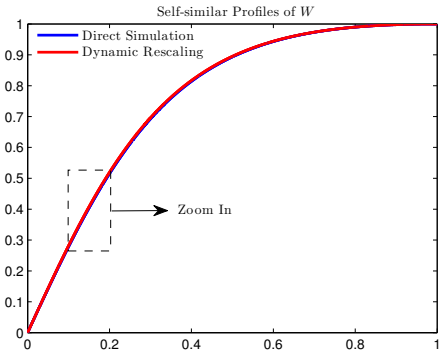

(a) Self-similar profiles of W.

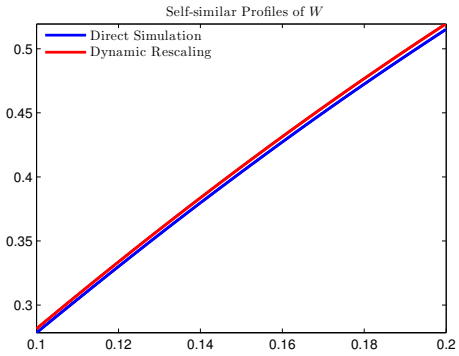

(b) Profiles of W (zoom in).

Figure 2.10: The self-similar profiles obtained from (2.4.14) and [40].

At the steady state, we compute the Jacobian (2.4.29) of the discretized dynamic rescaling system and compute its eigenvalues. The computation is exactly the same as that for the CKY-model (2.4.30) except in the Biot-Savart law (2.4.31). For the HL-model, the derivative of $\hat{u}_i$ with respect $\hat{w}_j$ is given explicitly in (2.4.46).

For $N_1 = 1000$, $N_2 = 2000$, the distribution of the eigenvalues of (2.4.29) is plotted in Figure 2.11a. From the figure we can see that the real parts of the eigenvalues of the Jacobian (2.4.29) are negative, and this implies that the self-similar profiles of the HL-model are stable. Then we refine the mesh using $N_1 = 2000$, $N_2 = 4000$, and compute the corresponding Jacobian matrix at the corresponding steady state. The eigenvalues of the Jacobian matrix are plotted in Figure 2.11b. We can see that the first several eigenvalues remain unchanged under mesh refinement.

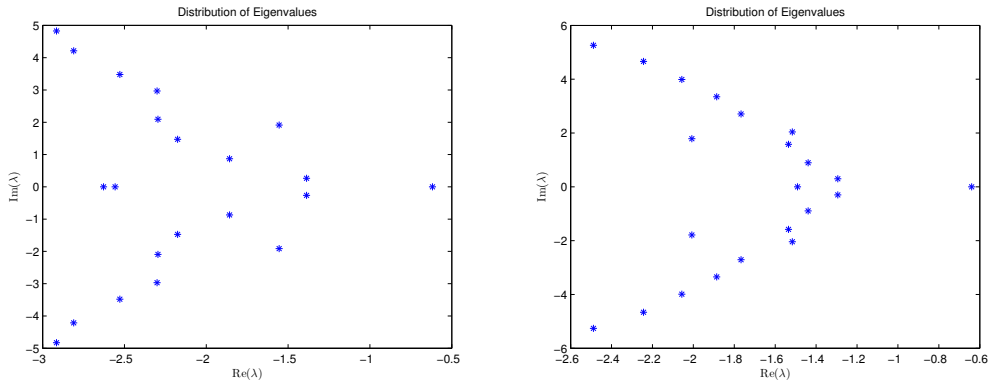

(a) Coarse mesh. (b) Fine mesh.

Figure 2.11: Leading eigenvalues of the Jacobian matrix.

2.5 Finite-time Singularity of the HL Model with Singular Profiles

Since the CKY model has a family of self-similar profiles corresponding to different leading orders of θ at the origin, one may expect similar behavior for the HL model based on their qualitative similarity. However, if we choose the second order derivative of $\theta(x,0)$ at the origin to be zero, then the solutions will develop finite-time singularity in a very different way. To be specific, the normalized solutions to the HL model will not converge as approaching the singularity time, but develop a singularity themselves. In another word, there is a smaller scale generated, and the solutions to the HL model develop singularity at multiple spatial scales.

We use two different approaches to study the behavior of the singular solutions in the case $s > 2$, direct numerical simulation of the 1D model, and the dynamic rescaling formulation that we introduced in the previous section.

Direct Numerical Simulation

In the direct numerical simulation, we choose the following initial data,

$$w(x,0) = 0, \quad \theta(x,0) = 4\sin^2(\frac{\pi}{2}x),$$

which corresponds to the case that

$$s = 4$$

as the leading order of $\theta(x,0)$ at the origin.

The numerical discretization of the equations (2.1.4), and the adaptive moving mesh method that we employ in this case with $s = 4$ are the same as that in our previous section. In the numerical simulation, we keep track of the maximal vorticity $\|w(t)\|_\infty$, the position where the maximal vorticity is attained $C_l(t)$,

$$\|w(t)\|_\infty = w(C_l(t),t),$$

and the numerical solutions at several time steps corresponding to different $\|w\|_\infty$. We consider two resolutions with $N = 2000$ and $N = 4000$ total node points.

We first study the blow up rate of the solutions. Based on the self-similar ansatz (2.2.2) that we made, and the relation between scaling exponents (2.2.3), we have

$$w(x,t) = (T-t)^{-1} W(\frac{x}{(T-t)^{c_l}}), \tag{2.5.1}$$

and thus we expect that $\|w(t)\|_\infty$ blows up as

$$\|w(t)\|_\infty = O((T-t)^{-1}).$$

$\|w(t)\|_\infty^{-1}$ versus t is plotted in Figure 2.12, which is indeed very close to a straight line. And we conclude that the blowup rate for $\|w\|_\infty$ is approximately

$$\|w\|_\infty \approx (T-t)^{-1}. \tag{2.5.2}$$

Next we consider the decay rate of $C_l(t)$, which is the position where the maximal vorticity is attained. $C_l(t)$ characterizes the length scale of the solutions. If the self-similar ansatz that we made in (2.5.1) is valid, then we have

$$C_l(t) = C(T-t)^{c_l}.$$

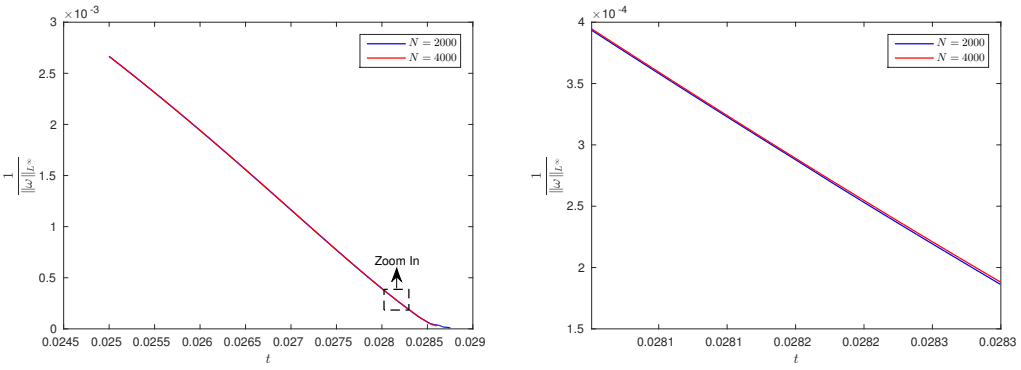

(a) $\|w\|_\infty^{-1}$. (b) Zoom in.

Figure 2.12: Blowup rate of $\|w\|_\infty$ for the HL model with $s = 4$.

$C_l(t)^{1/2}$ versus t is plotted in Figure 2.13, which is very close to a straight line. And we conclude that the decay of the length scale for $s = 4$ is approximately

$$C_l(t) \approx (T - t)^2. \tag{2.5.3}$$

In the self-similar equations (2.2.4), if $c_l = 2$, we have

$$(U + 2\xi)\Theta_\xi = 0, \quad W + (U + 2\xi)W_\xi = \Theta_\xi,$$

which can be easily proved to have only trivial analytic solutions.

However, this does not contradict our numerical results obtained here about the decay rate of $C_l(t)$, since the normalized solutions in this case do not converge to smooth profiles. And we will give an explanation of the blowup rate $\|w(t)\|_\infty^{-1}$ and $C_l(t)$ in the next subsection using the dynamic rescaling formulation.

Next we investigate the evolution of the spatial profiles in the singular solutions. Based on our obtained numerical solutions, we first normalize the leading order derivatives of θ and w at origin as what we did for the case $s = 2$.

At time steps corresponding to different $\|w\|_\infty$, we choose λ and μ such that

$$W(\xi) = \frac{1}{\mu} w(\frac{x}{\lambda}, t), \quad \Theta(\xi) = \frac{\lambda}{\mu} \theta(\frac{x}{\lambda}, t),$$

satisfy

$$W^{(3)}(0) = 1, \quad \Theta^{(4)}(0) = 1.$$

The resulting spatial profiles $W(\xi)$ and $\Theta(\xi)$ are plotted in Figure 2.14. We can see that the maximum of the profile W keeps increasing, and the position where

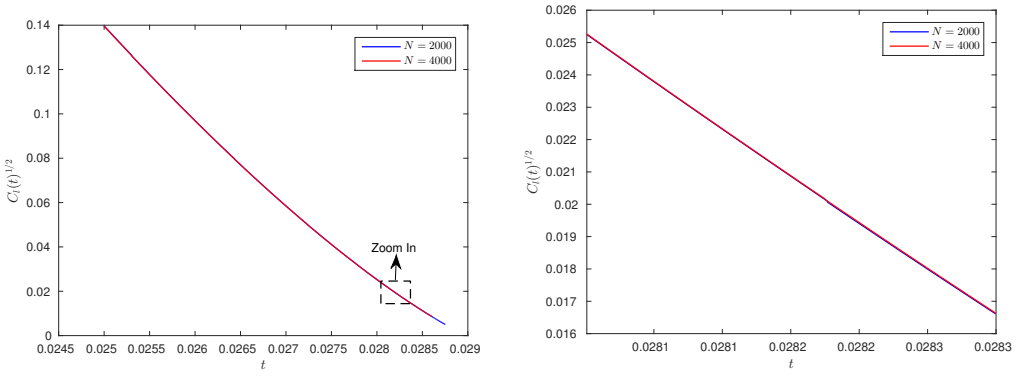

(a) $C_l(t)$. (b) Zoom in.

Figure 2.13: Decay rate of $C_l(t)$ for the HL model with $s = 4$.

the maximum is attained converges to the origin. At the same time, the profiles of Θ decay to zero. In another word, the profiles of the singular solutions do not converge under our normalization condition, but develop singularities themselves.

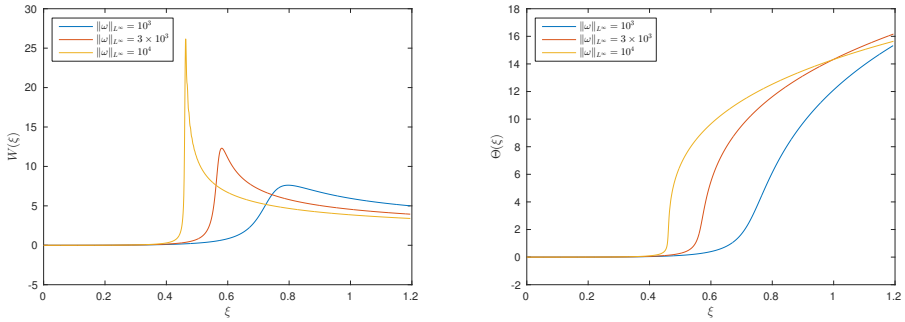

(a) The profiles of W. (b) The profiles of Θ.

Figure 2.14: Profiles of W and Θ obtained by normalizing their leading order derivatives at the origin.

Next we consider another normalization condition for the spatial profiles of W and Θ. We normalize the position where the maximum of w is attained, and the value of θ at that position. Namely, we choose λ and μ, such that

$$W(\xi) = \frac{1}{\mu} w(\frac{x}{\lambda}, t), \quad \Theta(\xi) = \frac{\lambda}{\mu} \theta(\frac{x}{\lambda}, t),$$

satisfy the following condition

$$\|W\|_\infty = W(1), \quad \Theta(1) = 1.$$

The profiles of the singular solutions at different time steps under this choice of normalization condition are plotted in Figure 2.15. From the figure, we can see that the W profile and Θ profile both converge to 0 on the left of 1, and the normalized W blows up at 1. Moreover, there is a jump developed at 1 for the Θ profile.

We will further investigate the spatial profiles in the singular solutions for the case $s > 2$ using the dynamic rescaling formulation in the next subsection.

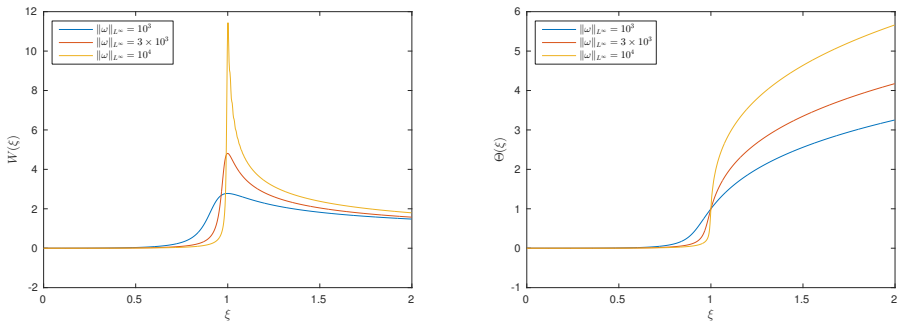

(a) The profiles of W.

(b) The profiles of Θ.

Figure 2.15: Profiles of W and Θ obtained by normalizing the position where $\|W\|_\infty$ is attained, and the value of Θ.

Dynamic Rescaling Formulation

In the dynamic rescaling formulation for the case $s = 4$, we use the same change of variables (2.4.13), and get the equation (2.4.16). We use the rescaling of the numerical solutions obtained from direct numerical simulation of the HL model as the initial data for the dynamic rescaling equations.

Because the solutions to the rescaling equations develop singularity, we adaptively put a certain portion of node points near the singular region. We use a total of 10^4 node points, and the maximum resolution near the singularity point is

$$3 \times 10^{-4}.$$

The change of variables (2.4.13) guarantees that the second order derivative of θ at the origin will remain as zero. To determine the scaling parameters $c_l(t)$ and $c_w(t)$ in the rescaling equations, we first normalize the leading order derivatives of the rescaled solutions, namely, we choose $c_l(t)$ and $c_w(t)$ to make

$$\frac{d}{dt}\theta^{(4)}(0,t) = 0, \quad \frac{d}{dt}w^{(3)}(0,t) = 0.$$

The solutions to the dynamic rescaling equations at several different time steps are plotted in Figure 2.16. We observe that solution w to the rescaling equations blows up. To be specific, $\|\omega\|_\infty$ blows up and the position where w attains its maximum converges to the origin. At the same time θ becomes smaller and tends to zero. These results agree with direct simulation of the HL model in Figure 2.14.

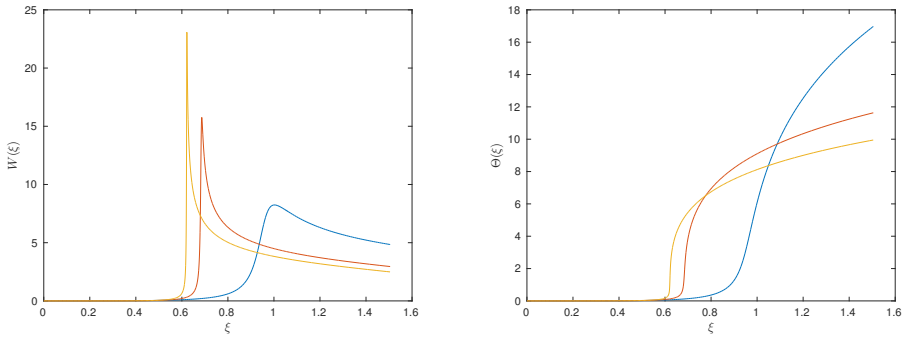

(a) w at different time steps. (b) θ at different time steps.

Figure 2.16: Evolution of solutions to the dynamic rescaling equations.

Then we consider normalizing the position where the maximal vorticity $\|w\|_\infty$ is attained, and the value of θ at that point. This normalization condition requires

$$\frac{d}{dt}w_x(1,t) = 0, \quad \frac{d}{dt}\theta(1,t) = 0. \tag{2.5.4}$$

The first condition gives

$$c_l(t) + u(1,t) = \frac{\theta_{xx}}{w_{xx}}.$$

In our simulation, we observe that at the position where w attains its maximum, θ_x also attains it maximum, and thus $\theta_{xx}(1,t) = 0$. Then the above normalization condition leads to the following choice of scaling parameters,

$$c_l(t) = u(1,t), \quad c_w(t) = -\frac{1}{2}c_l(t),$$

where the choice of $c_l(t)$ guarantees that the position of maximal vorticity is normalized, and $c_l(t) = -2c_w(t)$ guarantees that the value of θ will not change.

The solutions to the dynamic rescaling equations at different time steps are plotted in Figure 2.17. The solutions converge to singular profiles, with θ developing a jump and ω developing a peak point, which agrees with Figure 2.15.

In our simulation of the dynamic rescaling equations with the second normalization condition (2.5.4), we observe that the scaling parameter $c_l(t)$ grows with t linearly,

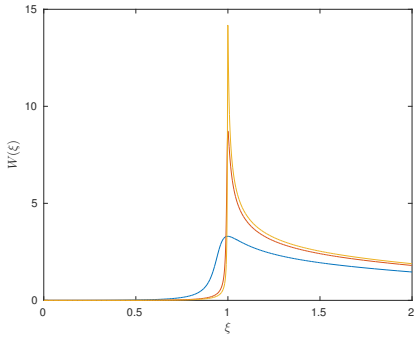

(a) w at different time steps.

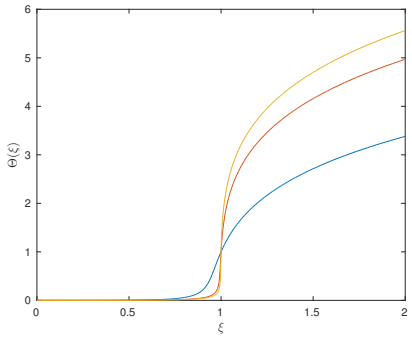

(b) θ at different time steps.

Figure 2.17: Evolution of solutions to the dynamic rescaling equations with the second normalization condition.

which is shown in Figure 2.18a. The maximal norm of w also grows linearly with t, which is shown in Figure 2.18b. Note that $c_l(t)$ ceases to increase after finite time, and this is because the numerical solutions to the rescaling equations lose accuracy after finite time as w blows up and θ develops a jump.

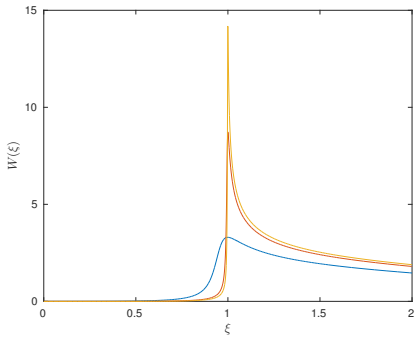

(a) $c_l(t)$ grows with t.

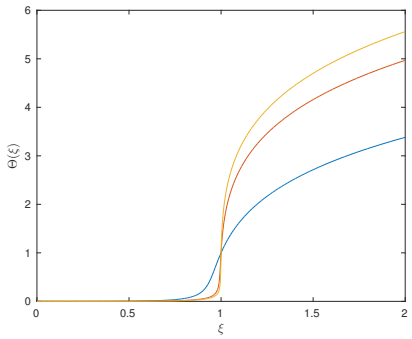

(b) $\|w\|_\infty$ grows with t.

Figure 2.18: Growth of the dynamic rescaling solutions with time.

Recall that we have the following relation between the dynamically rescaled solutions $\tilde{\theta}$, $\tilde{w}$ and the solutions to the HL model, θ, w,

$$\tilde{\theta}(x,t) = C_\theta(t)\theta\left(C_l(t)x, \tau(t)\right), \tag{2.5.5a}$$

$$\tilde{w}(x,t) = C_w(t)w\left(C_l(t)x, \tau(t)\right), \tag{2.5.5b}$$

where

$$C_\theta(t) = \exp(\int_0^t c_\theta(s)ds), \tag{2.5.5c}$$

$$C_w(t) = \exp(\int_0^t c_w(s)ds), \tag{2.5.5d}$$

$$C_l(t) = \exp(\int_0^t -c_l(s)ds), \tag{2.5.5e}$$

$$\tau(t) = \int_0^t \exp(\int_0^s c_w(y)dy)ds. \tag{2.5.5f}$$

Now we assume that the scaling parameter $c_l(s)$ and the maximum norm of w, $\|w\|_\infty$ both grow linearly with time s in the dynamic rescaling formulation,

$$c_l(s) = 2C_1 s, \quad c_w(s) = -C_1 s, \quad \|w(s)\|_\infty = C_2 s. \tag{2.5.6}$$

Then according to the above transformation relation (2.5.5), we can get that the blow up time of the original HL model is

$$T = \int_0^\infty \exp(\int_0^y c_w(x)dx)dy.$$

At time s of the rescaling system, the corresponding time in the HL model is

$$t = \int_0^s \exp(\int_0^x c_w(y)dy)dx.$$

Then according to our assumption (2.5.6), we have

$$T - t = \int_s^\infty \exp(\int_0^y c_w(x)dx)dy = \int_s^\infty \exp(-\frac{C_1}{2}x^2)dx.$$

The length scale in the solutions to the HL model is

$$C_l(t) = \exp(\int_0^s -c_l(s)ds) = \exp(-C_1 s^2). \tag{2.5.7}$$

The maximal norm of the solution w to the HL model is

$$\|w(t)\|_{L^\infty} = \exp(\int_0^t -c_w(s)ds)\|\tilde{w}(s)\|_\infty = C_2 s \exp(\frac{C_1}{2}s^2). \tag{2.5.8}$$

For large $s \gg 1$, we have

$$T - t = O(s^{-1}\exp(-\frac{C_1}{2}s^2)). \tag{2.5.9}$$

Then we conclude with (2.5.9) and (2.5.9) that

$$\|w(t)\|_\infty = O((T-t)^{-1}).$$

We take logarithm of $(T-t)$ in (2.5.9), and get

$$\log(T-t) = O(-\log s - \frac{C_1}{2}s^2) = O(-\frac{C_1}{2}s^2), \tag{2.5.10}$$

and thus

$$s = O(|\log(T-t)|^{1/2}). \tag{2.5.11}$$

With (2.5.9), (2.5.7) and (2.5.11), we get

$$C_l(t) = (T-t)^2|\log(T-t)|. \tag{2.5.12}$$

The results (2.5.10) and (2.5.12) can explain the blow up rate of the HL model observed in our direct numerical simulation, (2.5.2) and (2.5.3).

Note that here we only consider initial conditions for the dynamic rescaling equations with $s = 4$, and we observe that the solution θ converges to zero on the left of $x = 1$. So all derivatives of θ at the origin converge to zero, no matter what the initial leading order of θ is. With this we can conclude that the singular behaviors of the solutions to the rescaling equations are the same for all $s \geq 4$.

After discretization, the dynamic rescaling equations become an ODE system, and we observe that the solutions to this ODE system converge to a steady state. In the steady state of the ODE, θ is a step function, and w is like a point-mass.

The reason for this steady state configuration is that on the left side of $x < 1$, the velocity field of the dynamic rescaling equations satisfies

$$u(x) + c_l x > 0,$$

and information of the solutions at the origin propagates to the left, which makes θ vanish according to the equation

$$\theta_t + (u(x) + c_l(t)x)\theta_x = 0.$$

As a result, w also converges to 0, according to

$$w_t + (u(x) + c_l(t)x)w_x = \theta_x + c_w(t)w.$$

At $x = 1$, the velocity of the dynamic rescaling equations is zero, and thus the value of θ remains constant. On the right of $x = 1$, the velocity field satisfies

$$u(x) + c_l x > 0,$$

and consequently θ converges to a constant equal to $\theta(1)$.

Due to the formation of singularity in the dynamic rescaling equations, our numerical scheme can not resolve the solutions after finite time, and the ODE system loses accuracy in approximating the rescaling equations. This being said, since the dynamic rescaling equations are discretized using a stable numerical scheme (upwind scheme), the singular steady state of the resulting ODE may reflect the asymptotic behaviors of the solutions to the dynamic rescaling equations.

To summarize the singular behaviors of the two 1D models, we get that for the leading order of the initial data $\theta(x, 0)$ being $s = 2$, the solutions to the CKY model and the HL model both develop self-similar singularity as the 3D axisymmetric Euler equations, and the self-similar singularity scenario is stable.

For $s > 2$, the self-similarity of the singular solutions pertains for the CKY model, while for the HL model, the singular solutions exhibit multi-scale feature. To be specific, the profiles of the singular solutions develop singularity themselves, and the solutions to the HL model develop singularity at multiple spatial scales. We will see in the next chapter that for the 3D Euler equations with $s > 2$, the solutions also develop finite-time singularity at multiple spatial scales, which is a new singularity formation scenario not observed before in the literature.

Chapter 3

TWO TYPES OF SINGULAR BEHAVIORS FOR THE 3D EULER EQUATIONS

3.1 Connection of the 3D Euler Equations with the 2D Boussinesq System

Let's first recall the finite-time singularity scenario reported by Luo and Hou in [58], where the 3D axisymmetric Euler equations

$$u_{1,t} + u^r u_{1,r} + u^z u_{1,z} = 2u_1\psi_{1,z}, \tag{3.1.1a}$$

$$\omega_{1,t} + u^r \omega_{1,r} + u^z \omega_{1,z} = (u_1^2)_z, \tag{3.1.1b}$$

$$-[\partial_r^2 + (3/r)\partial_r + \partial_z^2]\psi_1 = \omega_1, \tag{3.1.1c}$$

with Biot-Savart law

$$u^r = -r\psi_{1,z}, \quad u^z = 2\psi_1 + r\psi_{1,r}, \tag{3.1.1d}$$

were numerically solved in a periodic cylinder. The configuration of the singular solutions in the meridian plane is plotted in Figure 3.1a.

The solid boundary and the odd symmetry of ω_1 and u_1 in the axial direction create a compressing flow along the boundary and seem to be responsible for the observed finite-time singularity. Moreover, the numerical solutions develop local self-similar structure around the singularity point in the meridian plane, $x = (z, r) = (0, 1)$.

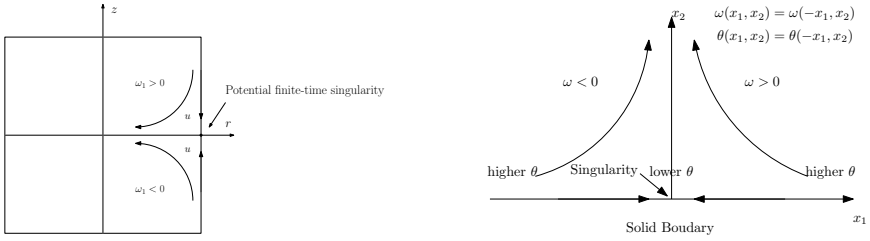

(a) In the meridian plane. (b) Boussinesq singularity.

Figure 3.1: Configuration of the potentially singular solutions.

We make the following self-similar ansatz for the local singular solutions, where

the 2D velocity field $v(\tilde{x},t)$ is $v(\tilde{x},t) = (u^z(\tilde{x},t), u^r(\tilde{x},t))^T$,

$$w_1(\tilde{x},t) \approx (T-t)^{c_w} W(\frac{\tilde{x}_0 - \tilde{x}_0}{(T-t)^{c_l}}), \tag{3.1.2a}$$

$$u_1(\tilde{x},t) \approx (T-t)^{c_u} U_1(\frac{\tilde{x} - \tilde{x}_0}{(T-t)^{c_l}}), \tag{3.1.2b}$$

$$v(\tilde{x},t) \approx (T-t)^{c_v} V(\frac{\tilde{x} - \tilde{x}_0}{(T-t)^{c_l}}), \tag{3.1.2c}$$

$$\psi_1(\tilde{x},t) \approx (T-t)^{c_\psi} \Psi(\frac{\tilde{x} - \tilde{x}_0}{(T-t)^{c_l}}). \tag{3.1.2d}$$

However, when plugging the above self-similar ansatz (3.1.2) into the equations (3.1.1), we cannot match the exponent of $(T-t)$ for each term in the equations. This is because the axisymmetric Euler equations (3.1.1) do not enjoy a perfect scaling invariant property centered at the boundary point $(r,z) = (1,0)$.

For $c_l > 0$, the $2u_1\psi_{1,z}$ term in (3.1.1a) and the $(3/r)\partial_r\psi$ term in (3.1.1c) become low order terms, and they will be discarded in the self-similar equations (3.1.4). We get the following conditions for the scaling exponents

$$c_w = -1, \quad c_v = c_l - 1, \quad c_u = c_l/2 - 1, \tag{3.1.3}$$

and the self-similar equations governing the self-similar profiles,

$$W + c_l\xi \cdot \nabla W + V \cdot \nabla W = (U_1^2)_{\xi_1}, \tag{3.1.4a}$$

$$(1 - c_l/2)U_1 + c_l\xi \cdot \nabla U_1 + V \cdot \nabla U_1 = 0, \tag{3.1.4b}$$

$$V = \nabla^\perp(-\Delta)^{-1}W. \tag{3.1.4c}$$

Note that c_l is the only unknown scaling exponent in the relation (3.1.3), and it cannot be determined by dimensional analysis. To solve the self-similar equations (3.1.4), one needs to find c_l such that equations (3.1.4) have non-trivial solutions, which is essentially a nonlinear eigenvalue problem.

It is well-known that the 3D axisymmetric Euler equations away from the axis are similar to the 2D Boussinesq system [59], which is given by

$$\omega_t + v \cdot \nabla\omega = \theta_{x_1}, \tag{3.1.5a}$$

$$\theta_t + v \cdot \nabla\theta = 0. \tag{3.1.5b}$$

The velocity field $v(x_1,x_2)$ is related to the voricity field $\omega(x_1,x_2)$ through

$$v = \nabla^\perp(-\Delta)\omega. \tag{3.1.5c}$$

In the Boussinesq system (3.1.5), the quantity θ plays the same role as the square of the angular velocity u_1^2 in Euler equations (3.1.1). If we rotate the finite-time singularity scenario in Figure 3.1a by $\pi/2$, we get a corresponding finite-time singularity scenario for the 2D Boussinesq system depicted in Figure3.1b.

The Boussinesq system has the following scaling-invariant property,

$$\theta(x,t) \to \frac{\lambda}{\mu^2}\theta(\frac{x}{\lambda},\frac{t}{\mu}), \quad \omega(x,t) \to \frac{1}{\mu}w(\frac{x}{\lambda},\frac{t}{\mu}), \quad v(x,t) \to \frac{\lambda}{\mu}v(\frac{x}{\lambda},\frac{t}{\mu}). \tag{3.1.6}$$

If we make the following ansatz for the singularity scenario in Figure 3.1b,

$$\theta = (T-t)^{c_\theta}\Theta(\frac{x}{(T-t)^{c_l}}),\ \omega = W(\frac{x}{(T-t)^{c_l}}),\ v = (T-t)^{c_v}V(\frac{x}{(T-t)^{c_l}}), \tag{3.1.7}$$

and plug them in (3.1.5), we get the following relation for the scaling exponents

$$c_v = c_l - 1, \quad c_\theta = c_l - 2, \quad c_w = -1, \tag{3.1.8}$$

and the self-similar equations governing the self-similar profiles,

$$W + c_l\xi\cdot\nabla W + V\cdot\nabla W = \Theta_{\xi_1}, \tag{3.1.9a}$$

$$(2-c_l)\Theta + c_l\xi\cdot\nabla\Theta + V\cdot\nabla\Theta = 0, \tag{3.1.9b}$$

$$V = \nabla^\perp(-\Delta)^{-1}W. \tag{3.1.9c}$$

We do not need to discard any low order terms (as in (3.1.4)) to get (3.1.9).

One can see that the self-similar equations for the axisymmetric Euler (3.1.4) and the 2D Boussinesq system (3.1.9) are indeed equivalent with the change of variables

$$\Theta = U_1^2.$$

In this chapter, we first employ a power series method to construct local analytic solutions to the self-similar equations (3.1.4). However, due to the 2D nature of the equations, we cannot extend the local self-similar profiles to the whole domain by solving the PDE as we did for the 1D CKY model.

Then we study the stability of the self-similar profiles in (3.1.4) using the dynamic rescaling formulation, which has been introduced in Chapter 2. We consider the dynamic rescaling formulation for the 2D Boussinesq instead of the axisymmetric Euler, because the 2D Boussinesq system (3.1.5) enjoys perfect scaling invariant property, which is absent for the 3D axisymmetric Euler.

If we work on the 3D Euler equations, then to make the rescaling equations equivalent to the original Euler system, one has to put some time-dependent coefficients on the low order terms that are discarded in the self-similar equations (3.1.4).

We will show that the dynamic rescaling equations for the Euler equations (3.1.1) can actually be viewed as a perturbation to that of the Boussinesq system (3.1.5), with the perturbation converging to zero exponentially fast in time. This together with the stability of the self-similar profiles can justify the use of the rescaling equations for the Boussinesq system to investigate the Euler self-similar singularity.

3.2 Existence of Local Analytic Self-similar Profiles

In Chapter 2, we proved the existence of self-similar profiles for the 1D CKY model by constructing local power series solutions, and then extending the local solutions to infinity. For the self-similar equations of the 2D Boussinesq system (3.1.9), with suitable local analytic boundary conditions, we can also prove that there exists a family of local analytic solutions using the power series method.

Let the leading order of $\Theta(\xi_1,\xi_2)$ in ξ_1 be $s = 2k$,

$$\Theta(\xi_1,\xi_2) = O(\xi_1^s), \quad |\xi| \to 0.$$

Note that s has to be even due to the even symmetry of $\Theta(\xi_1,\xi_2)$ in ξ_1.

We specify a local analytic boundary condition for $V_2(0,\xi_2)$,

$$V_2(0,\xi_2) = v(\xi_2). \tag{3.2.1}$$

Then we consider (3.1.9) with the Biot-Savart law replaced by local relation

$$\partial_{\xi_1} V_1 + \partial_{\xi_2} V_2 = 0, \quad \partial_{\xi_1} V_2 - \partial_{\xi_2} V_1 = W.$$

The first equation above is the incompressibility condition, and the second one is

$$\nabla \times V = W.$$

Theorem 3.2.1. *For fixed $c_l > 2$ and the leading order of Θ at the origin, s,*

$$\Theta(\xi_1,\xi_2) = O(\xi_1^s), \quad \partial_{\xi_1}^s \Theta(0,0) = 1,$$

if the local analytic boundary condition (3.2.1) *satisfies*

$$v'(0) = \frac{(s-1)c_l + 2}{s}, \tag{3.2.2}$$

then there exist unique analytic solutions to (3.1.9) *with boundary condition* (3.2.1).

Before we prove the above theorem, we comment that this result is non-trivial because there exists a formal singularity at the origin for the system (3.1.9), and thus the Cauchy-Kowalevski theorem does not apply. There are some extensions of the classical theorem to equations with a formal singularity [3, 2], which assert that under certain *Fuchs type* conditions, analytic solutions to the singular PDE exist and are unique. In our construction, the *Fuchs type* conditions fail for equations (3.1.9), and this is actually necessary for the existence of nontrivial self-similar profiles.

Our proof of the local existence is essentially a modification of the Cauchy-Kowalevski majorization argument, and due to the formal singularity, one needs to take advantage of the special structure of the equations to construct the majorizing PDE.

We only prove Theorem 3.2.1 for the case $s = 2$ in this thesis. But the same argument applies to other cases with $s \geq 4$ without difficulty.

Proof. With local boundary condition (3.2.1) and even symmetry of V_2, we have

$$V_2(\xi_1, \xi_2) = v(\xi_2) + O(\xi_1^2). \tag{3.2.3}$$

Using the incompressibility condition $\nabla \cdot V = 0$, one can get

$$V_1(\xi_1, \xi_2) = -\xi_1 v'(\xi_2) + O(\xi_1^3). \tag{3.2.4}$$

Using (3.2.3), (3.2.4) and the fact that the leading order of Θ is 2 in (3.1.9b),

$$\partial_{\xi_1}^2 \Theta(0,0) \neq 0,$$

we get the following condition, which is (3.2.2) in the case $s = 2$,

$$v'(0) = \frac{c_l + 2}{2}. \tag{3.2.5}$$

Then we make the following change of variables,

$$V_1(\xi_1, \xi_2) = -\frac{c_l + 2}{2}\xi_1 - \xi_1 \phi'(\xi_2) + \xi_1 U_1(\xi_1, \xi_2), \tag{3.2.6a}$$

$$V_2(\xi_1, \xi_2) = \frac{c_l + 2}{2}\xi_2 + \phi(\xi_2) + \xi_1 U_2(\xi_1, \xi_2), \tag{3.2.6b}$$

where $\phi(\xi_2)$ is $v(\xi_2)$ minus its linear part,

$$\phi(\xi_2) = \sum_{j=2}^{\infty} \phi_j \xi_2^j = v(\xi_2) - \frac{c_l + 2}{2}\xi_2. \tag{3.2.6c}$$

With the change of variables (3.2.6), the equations for Θ, W, U_1 and U_2 become

$$(2-c_l)\Theta + \frac{c_l-2}{2}\xi_1\partial_{\xi_1}\Theta + \frac{3c_l+2}{2}\xi_2\partial_{\xi_2}\Theta \\ -\xi_1\phi'(\xi_2)\partial_{\xi_1}\Theta + \phi(\xi_2)\partial_{\xi_2}\Theta + \xi_1 U_1\partial_{\xi_1}\Theta + \xi_1 U_2\partial_{\xi_2}\Theta = 0, \quad (3.2.7a)$$

$$W + \frac{c_l-2}{2}\xi_1\partial_{\xi_1}W + \frac{3c_l+2}{2}\xi_2\partial_{\xi_2}W \\ -\xi_1\phi'(\xi_2)\partial_{\xi_1}W + \phi(\xi_2)\partial_{\xi_2}W + \xi_1 U_1\partial_{\xi_1}W + \xi_1 U_2\partial_{\xi_2}W = \Theta_{\xi_1}, \quad (3.2.7b)$$

$$U_1 + \xi_1\partial_{\xi_1}U_1 + \xi_1\partial_{\xi_2}U_2 = 0, \quad (3.2.7c)$$

$$\xi_1\partial_{\xi_2}U_1 - \xi_1\phi''(\xi_2) - U_2 - \xi_1\partial_{\xi_1}U_2 = W. \quad (3.2.7d)$$

We make the following power series ansatz for equations (3.2.7),

$$\Theta = \sum_{i=2}^{\infty}\sum_{j=0}^{\infty}\Theta_{i,j}\xi_1^i\xi_2^j, \qquad W = \sum_{i=1}^{\infty}\sum_{j=0}^{\infty}W_{i,j}\xi_1^i\xi_2^j, \quad (3.2.8a)$$

$$U_1 = \sum_{i=1}^{\infty}\sum_{j=0}^{\infty}U^1_{i,j}\xi_1^i\xi_2^j, \qquad U_2 = \sum_{i=1}^{\infty}\sum_{j=1}^{\infty}U^2_{i,j}\xi_1^i\xi_2^j. \quad (3.2.8b)$$

Plugging the ansatz (3.2.8) into (3.2.7), for the Θ equation (3.2.7a), we get that,

$$(2-c_l+i(c_l-2)/2+j(3c_l+2)/2)\Theta_{i,j} - \sum_{n=0}^{j-1} i(j-n+1)\Theta_{i,n}\phi_{j-n+1} + \\ \sum_{n=0}^{j-1} n\Theta_{i,n}\phi_{j-n+1} + \sum_{m=2}^{i-1}\sum_{n=0}^{j} m\Theta_{m,n}U^1_{i-m,j-n} + \sum_{m=2}^{i-2}\sum_{n=0}^{j} nU^2_{i-m-1,j-n+1}\Theta_{m,n} = 0. \quad (3.2.9a)$$

For the $W(\xi_1,\xi_2)$ equation (3.2.7b), we have

$$(1+i(c_l-2)/2+j(3c_l+2)/2)W_{i,j} - \sum_{n=0}^{j-1} i(j-n+1)W_{i,n}\phi_{j-n+1} + \\ \sum_{n=0}^{j-1} nW_{i,n}\phi_{j-n+1} + \sum_{m=1}^{i-1}\sum_{n=0}^{j} mW_{m,n}U^1_{i-m,j-n} + \sum_{m=1}^{i-2}\sum_{n=0}^{j} nU^2_{i-m-1,j-n+1}W_{m,n} = (i+1)\Theta_{i+1,j}. \quad (3.2.9b)$$

And the incompressibility condition (3.2.7c) is

$$U^1_{i,j} + iU^1_{i,j} + (j+1)U^2_{i-1,j+1} = 0. \quad (3.2.9c)$$

The Biot-Savart law (3.2.7d) becomes

$$(j+1)U^1_{i-1,j+1} - \delta_{i1}(j+2)(j+1)\phi_{j+2} - U^2_{i,j} - iU^2_{i,j} = W_{i,j}. \tag{3.2.9d}$$

Using condition (3.2.5) in (3.2.9a), we have one degree of freedom in determining $\Theta_{2,0} > 0$. Without loss of generality, we can simply choose $\Theta_{2,0} = 1$.

Then we can determine

$$\Theta_{2,j}, \quad j = 1, \ldots \infty,$$

inductively based on (3.2.9a). Next using $\Theta_{2,j}$ in (3.2.9b), we can determine

$$W_{1,j}, \quad j = 0, \ldots \infty,$$

inductively. And using $W_{1,j}$ in the Biot-Savart law (3.2.9d), we can determine

$$U^2_{1,j}, \quad j = 1, \ldots \infty,$$

inductively. $U^1_{1,j}$ can be determined from (3.2.9c), and we have $U^1_{1,j} = 0$.

Assuming now that for some $i \geq 1$ we have determined

$$U^1_{i,j}, \quad \Theta_{i+1,j}, \quad W_{i,j}, \quad U^2_{i,j}, \quad j = 0, \ldots \infty. \tag{3.2.10}$$

Then using (3.2.9c), we can first determine

$$U^1_{i+1,j}, \quad j = 1, 2 \cdots \infty. \tag{3.2.11}$$

Then using (3.2.9a) and (3.2.11), we can determine

$$\Theta_{i+2,j}, \quad j = 1, 2 \cdots \infty. \tag{3.2.12}$$

Next we use (3.2.9b), (3.2.11) and (3.2.12) to determine

$$W_{i+1,j}, \quad j = 1, \cdots \infty. \tag{3.2.13}$$

Finally we use (3.2.9d), (3.2.13) and (3.2.11) to determine

$$U^2_{i+1,j}, \quad j = 1, \cdots \infty.$$

Thus using (3.2.10), we can determine

$$U^1_{i+1,j}, \quad \Theta_{i+2,j}, \quad W_{i+1,j}, \quad U^2_{i+1,j}, \quad j = 0, \ldots \infty,$$

and then all the coefficients in (3.2.8) can be uniquely inductively determined.

We denote $\Theta_2(\xi_2)$ as

$$\Theta_2(\xi_2) = \frac{1}{2}\partial_{\xi_1}^2\Theta(0,\xi_2) = \sum_{j=0}^{\infty}\Theta_{2,j}\xi^j.$$

Then using (3.2.7a), we can derive that $\Theta_2(\xi_2)$ satisfies the following equation,

$$\Theta_2(\xi_2)[\frac{c_l+2}{2}\xi_2 + \phi(\xi_2)] = \Theta_2(\xi_2)\phi'(\xi_2).$$

Using $\Theta_2(0) = 1$ and the fact that $\phi(\xi_2) = O(\xi_2^2)$ near $\xi_2 = 0$, we can determine $\Theta_2(\xi_2)$ as a local analytic function,

$$\Theta_2(\xi_2) = \exp\int_0^{\xi_2}\frac{\phi'(t)}{(c_l+2)/2t + \phi(t)}dt.$$

To finish the proof of the theorem, we still need to prove that the power series (3.2.8) constructed using the above procedure converge near the origin. Our strategy is finding a set of majorizing power series whose convergence is easier to prove.

We say that a power series

$$f^m(\xi_1,\xi_2) = \sum_{i=0}^{\infty}\sum_{j=0}^{\infty}f_{i,j}^m\xi_1^i\xi_2^j$$

majorize power series

$$f(\xi_1,\xi_2) = \sum_{i=0}^{\infty}\sum_{j=0}^{\infty}f_{i,j}\xi_1^i\xi_2^j$$

if

$$f_{i,j}^m \geq |f_{i,j}|,$$

and we denote this as

$$f^m(\xi_1,\xi_2) \gg f(\xi_1,\xi_2) \quad \text{or} \quad f(\xi_1,\xi_2) \ll f^m(\xi_1,\xi_2).$$

Since $\phi(\xi_2)$ and $\Theta_2(\xi_2)$ are analytic, we can find analytic $\phi^m(\xi_2)$, $\Theta_2^m(\xi_2)$, such that

$$\Theta_2^m(\xi_2) \gg \Theta_2(\xi_2), \quad \phi^m(\xi_2) \gg \phi(\xi_2),$$

with the same leading order values,

$$\Theta_2^m(0) = 1, \quad \phi^m(0) = (\phi^m)'(0) = 0.$$

Then we consider the following PDE system with zero initial conditions at $\xi_1 = 0$,

$$\partial_{\xi_1}\Theta^m = 4\frac{U_2^m\partial_{\xi_2}\Theta^m + (c_l-2)\xi_1\Theta_2^m/4}{(c_l-2)/4 - U_1^m - (\phi^m)'}\frac{1}{1-2\phi^m/(\xi_2(3c_l+2))}, \tag{3.2.14a}$$

$$\partial_{\xi_1}W^m = \frac{\frac{4((\phi^m)''+\partial_{\xi_2}U_2^m)\partial_{\xi_2}\Theta^m+(c_l-2)\Theta_2^m/4}{((c_l-2)/4-U_2^m-(\phi^m)')(1-2\phi^m/(\xi_2(3c_l+2)))} + U_2^m\partial_{\xi_2}W^m}{\frac{c_l-2}{2} - \frac{4\partial_{\xi_2}\Theta^m}{((c_l-2)/4-U_1^m-(\phi^m)')(1-2\phi^m/\xi_2/(3c_l+2))} - U_1^m - (\phi^m)'} \tag{3.2.14b}$$

$$\times\frac{1}{1-2\phi^m/(\xi_2(3c_l+2))}, \tag{3.2.14c}$$

$$\partial_{\xi_1}U_1^m = \partial_{\xi_2}U_2^m, \tag{3.2.14d}$$

$$\partial_{\xi_1}U_2^m = \partial_{\xi_1}W_m + \phi_m''(y) + \partial_{\xi_2}U_1^m. \tag{3.2.14e}$$

The RHS of (3.2.14) is analytic with respect to ξ_1, ξ_2, Θ^m, U_1^m, U_2^m, W^m and their first order derivatives, and then using the Cauchy-Kowalevski Theorem, there exist unique local analytic solutions to the above PDE with zero initial conditions

$$W^m(0,\xi_2) = \Theta^m(0,\xi_2) = U_1^m(0,\xi_2) = U_2^m(0,\xi_2) = 0.$$

A remarkable property for system (3.2.14) is that all derivatives of the right hand side with respect to ξ_1, ξ_2 and U_1^m, V_1^m, Θ^m, W^m and their first order derivatives are non-negative. This is because the factors in the RHS all can be expended as

$$\frac{1}{1-x} = 1 + x + x^2 + \cdots \gg 0. \tag{3.2.15}$$

Thus the derivatives of the solutions Θ^m, W^m, U_1^m and U_2^m at the origin are also non-negative based on the construction in the Cauchy-Kowalevski Theorem [28].

Next, we prove that the power series solutions of (3.2.14) actually majorize the solutions of (3.2.7) that we construct. We expand solutions to (3.2.14) as

$$\Theta^m = \sum_{i=2}^{\infty}\sum_{j=0}^{\infty}\Theta_{i,j}^m\xi_1^i\xi_2^j, \qquad W^m = \sum_{i=1}^{\infty}\sum_{j=0}^{\infty}W_{i,j}^m\xi_1^i\xi_2^j, \tag{3.2.16a}$$

$$U_1^m = \sum_{i=1}^{\infty}\sum_{j=0}^{\infty}U_{i,j}^{m,1}\xi^i\xi_2^j, \qquad U_2^m = \sum_{i=1}^{\infty}\sum_{j=1}^{\infty}U_{i,j}^{m,2}\xi_1^i\xi_2^j. \tag{3.2.16b}$$

It is obvious that for $k = 0$,

$$|U_{i,j}^1| \le U_{i,j}^{m,1},\ |U_{i,j}^2| \le U_{i,j}^{m,2},\ |W_{i,j}| \le W_{i,j}^m,\ |\Theta_{i+1,j}| \le \Theta_{i+1,j}^m,\ i \le k, j = 0,\ldots\infty, \tag{3.2.17}$$

since all of them vanish.

Now we assume that (3.2.17) holds for $k = m$, and prove that (3.2.17) holds for $k = m + 1$. If $m = 0$, we can compute $\partial^2_{\xi_1}\Theta^m(0,\xi_2)$ directly from (3.2.14a) as

$$\partial^2_{\xi_1}\Theta^m(0,\xi_2) = \frac{2(c_l-2)\Theta_2^m}{(c_l-2)/2 - U_1^m - (\phi^m)'}\frac{1}{1-2\phi^m/(\xi_2(3c_l+2))} \gg 4\Theta_2^m \gg 2\Theta_2.$$

In the above estimate, we have used the fact

$$\frac{1}{(c_l-2)/2 - U_1^m - (\phi^m)'} \gg \frac{2}{c_l-2}, \quad \frac{1}{1-2\phi^m/(\xi_2(3c_l+2))} \geq 1,$$

according to the expansion (3.2.15). So

$$|\Theta_{2,j}| \leq \Theta^m_{2,j}.$$

If $m \neq 0$, $\Theta_{m+1,j}$ is determined using (3.2.9a),

$$\begin{aligned}\Theta_{m+1,j} = &\frac{\sum_{n=0}^{j-1}(m+1)(j-n+1)\Theta_{m+1,n}\phi_{j-n+1}}{2-c_l+(m+1)(c_l-2)/2+j(3c_l+2)/2}\\ &-\frac{-\sum_{l=2}^{m}\sum_{n=0}^{j}[l\Theta_{l,n}U^1_{m+1-l,j-n}+nU^2_{m-l,j-n+1}\Theta_{l,n}]}{2-c_l+(m+1)(c_l-2)/2+j(3c_l+2)/2}\\ &+\frac{\sum_{n=0}^{j-1}-n\Theta_{m+1,n}\phi_{j-n+1}}{2-c_l+(m+1)(c_l-2)/2+j(3c_l+2)/2}.\end{aligned}$$

Separating the denominator to two positive parts, we get

$$|\Theta_{m+1,j}| \leq \max\{I_1, I_2\}, \tag{3.2.18}$$

where

$$\begin{aligned}I_1 = |&\frac{\sum_{n=0}^{j-1}(m+1)(j-n+1)\Theta_{m+1,n}\phi_{j-n+1}}{2-c_l+(m+1)(c_l-2)/2}\\ &-\frac{\sum_{l=2}^{m}\sum_{n=0}^{j}[l\Theta_{l,n}U^1_{m+1-l,j-n}+nU^2_{m-l,j-n+1}\Theta_{l,n}]}{2-c_l+(m+1)(c_l-2)/2}|, \quad (3.2.19a)\end{aligned}$$

$$I_2 = |\frac{\sum_{n=0}^{j-1}-n\Theta_{m+1,n}\phi_{j-n+1}}{j(3c_l+2)/2}|. \tag{3.2.19b}$$

For $j = 0$, we define $I_2 = 0$.

In the above estimate (3.2.18), we have used the fact that

$$\frac{a_1+a_2}{b_1+b_2} \leq \max(\frac{a_1}{b_1},\frac{a_2}{b_2}), \quad \text{for} \quad b_1, b_2 > 0.$$

Then we consider $\Theta^m_{m+1,j}$, and introduce the following notation.

For $f(\xi_1,\xi_2)=\sum_{i=0}^{\infty}\sum_{j=0}^{\infty} f_{i,j}\xi_1^i\xi_2^j$, we define

$$F_{m,n}[f]=f_{m,n}.$$

According to (3.2.14a),

$$(m+1)\Theta^m_{m+1,j}=F_{m,j}[4\frac{U_2^m\partial_{\xi_2}\Theta^m+(c_l-2)\xi_1\Theta_2^m/4}{(c_l-2)/4-U_1^m-(\phi^m)'}\frac{1}{1-2\phi^m/(\xi_2(3c_l+2))}].$$

Next we use induction to prove that for $j=0,\dots\infty$,

$$\Theta^m_{m+1,j}=\frac{1}{m+1}F_{m,j}[4\frac{U_2^m\partial_{\xi_2}\Theta^m+(c_l-2)\xi_1\Theta_2^m/2}{(c_l-2)/4-U_1^m-(\phi^m)'}\frac{1}{1-2\phi^m/(\xi_2(3c_l+2))}]$$
$$\geq|\Theta_{m+1,j}|.$$

For $j=0$, since $I_2=0$, we have

$$|\Theta_{m+1,0}|\leq|I_1|.$$

And according to (3.2.14a),

$$\partial_{\xi_1}\Theta^m((c_l-2)/4-U_1^m-(\phi^m)')=4(U_2^m\partial_{\xi_2}\Theta^m+(c_l-2)\xi_1\Theta_2^m/4)\times$$
$$\frac{1}{1-2\phi^m/\xi_2/(3c_l+2)}.$$

Since $\frac{1}{1-2\phi^m/\xi_2/(3c_l+2)}\gg 1$,

$$\partial_{\xi_1}\Theta^m((c_l-2)/4-U_1^m-(\phi^m)')\gg 4(U_2^m\partial_{\xi_2}\Theta^m+(c_l-2)\xi_1\Theta_2^m/4).$$

Finally, discarding the second term on the RHS, we get

$$\frac{c_l-2}{4}\Theta^m_{\xi_1}\gg(\phi^m)'\partial_{\xi_1}\Theta^m+U_1^m\partial_{\xi_1}\Theta^m+U_2^m\partial_{\xi_2}\Theta^m.$$

Considering the coefficient of the $\xi_1^m\xi_2^j$ term on both sides, we get

$$\frac{(m+1)(c_l-2)}{4}\Theta^m_{i,j}\geq$$
$$\sum_{n=0}^{j-1}(m+1)(j-n+1)\Theta^m_{m+1,n}\phi^m_{j-n+1}$$
$$+\sum_{l=2}^{m}\sum_{n=0}^{j}[l\Theta^m_{l,n}U^{m,1}_{m+1-l,j-n}+nU^{m,2}_{m-l,j-n+1}\Theta^m_{l,n}].$$

Choosing $j = 0$ and using the induction assumption (3.2.17), we get

$$\Theta^m_{m+1,0} \geq \frac{4}{(m+1)(c_l-2)} \sum_{l=2}^{m} l|\Theta_{l,0}||U^{m,1}_{m+1-l,0}|. \tag{3.2.20}$$

Using the fact that

$$(m+1)(c_l-2)/4 \leq (m+1)(c_l-2)/2 - 1,$$

in (3.2.20) and comparing (3.2.20) with (3.2.19a), we get

$$\Theta^m_{m+1,0} \geq I_1 \geq |\Theta_{m+1,0}|.$$

Now we assume that

$$\Theta^m_{m+1,j} \geq |\Theta_{m+1,j}|, \quad \text{for} \quad j \leq p,$$

and consider $\Theta_{m+1,p+1}$ and $\Theta^m_{m+1,p+1}$.

If $I_1 \geq I_2$ for $i = m+1$, $j = p+1$, using the same argument as $j = 0$ will lead to

$$\Theta^m_{m+1,p+1} \geq |\Theta_{m+1,p+1}|.$$

Otherwise, we consider I_2, and according to (3.2.19b), we have

$$I_2 \leq \frac{\sum_{n=0}^{j-1} |\Theta_{m+1,n}\phi_{j-n+1}|}{(3c_l+2)/2}.$$

Using the induction assumption (3.2.17), we get

$$I_2 \leq \frac{\sum_{n=0}^{j-1} \Theta^m_{m+1,n}\phi^m_{j-n+1}}{(3c_l+2)/2}.$$

Based on the above estimate, we have

$$I_2 \leq \frac{1}{m+1} F_{m,j}[\xi_1\Theta^m_2 \times \frac{\phi^m}{\xi_2(3c_l+2)}].$$

Using the fact that

$$U^m_2 \gg 0, \quad \Theta^m \gg 0, \quad \frac{1}{1-x} \gg 1,$$

we can get

$$I_2 \leq \frac{1}{m+1} F_{m,j}[4\frac{U^m_2\partial_{\xi_2}\Theta^m + (c_l-2)\xi_1\Theta^m_2/4}{(c_l-2)/4 - U^m_1 - (\phi^m)'} \frac{2\phi^m/(\xi_2(3c_l+2))}{1-2\phi^m/(\xi_2(3c_l+2))}].$$

Since

$$\frac{2\phi^m/(\xi_2(3c_l+2))}{1-2\phi^m/(\xi_2(3c_l+2))} \ll \frac{1}{1-2\phi^m/(\xi_2(3c_l+2))},$$

we get

$$|\Theta_{m+1,j}| \le \frac{1}{m+1} F_{m,j}[4\frac{U_2^m \partial_{\xi_2}\Theta^m + (c_l-2)\xi_1\Theta_2^m/4}{(c_l-2)/4 - U_1^m - (\phi^m)'} \frac{1}{1-2\phi^m/(\xi_2(3c_l+2))}] = \Theta_{m+1,j}^m.$$

So now we have proved that

$$|\Theta_{m+1,j}| \le |\Theta_{m+1,j}^m|, \quad \text{for} \quad j = 0, \dots \infty.$$

Then we consider $W_{m,j}$ and $W_{m,j}^m$ for $j = 0, \dots \infty$.

$W_{m,j}$ is determined from (3.2.9b), and we have

$$W_{m,j} = \frac{\sum_{n=0}^{j-1} m(j-n+1)W_{m,n}\phi_{j-n+1}}{1+m(c_l-2)+j(3c_l+2)/2} - \frac{\sum_{l=1}^{m-1}\sum_{n=0}^{j}(m-1)[W_{l,n}U_{m-l,j-n}^1 + nU_{m-1-l,j-n+1}^2 W_{l,n}]}{1+m(c_l-2)+j(3c_l+2)/2} + \frac{-\sum_{n=0}^{j-1} nW_{m,n}\phi_{j-n+1} + (m+1)\Theta_{m+1,j}}{1+m(c_l-2)+j(3c_l+2)/2}.$$

Again we separate the denominator into two parts, and get

$$|W_{m,j}| \le \max\{J_1, J_2\},$$

where

$$J_1 = |\frac{\sum_{n=0}^{j-1} m(j-n+1)W_{m,n}\phi_{j-n+1}}{1+m(c_l-2)} - \frac{\sum_{l=1}^{i-1}\sum_{n=0}^{j} l[W_{l,n}U_{m-l,j-n}^1 + nU_{m-l-1,j-n+1}^2 W_{l,n}] + (m+1)\Theta_{m+1,j}}{1+m(c_l-2)}|, \quad (3.2.21a)$$

$$J_2 = |\frac{-\sum_{n=0}^{j-1} nW_{i,n}\phi_{j-n+1}}{j(3c_l+2)/2}|. \quad (3.2.21b)$$

And for $j = 0$, we simply define $J_2 = 0$.

Next we use induction to prove that

$$|W_{m,j}| \le W_{m,j}^m, \quad \text{for} \quad j = 0, \dots \infty.$$

For $j = 0$, $J_2 = 0$, so $|W_{m,0}| \leq J_1$. According to (3.2.14c), we have

$$\partial_{\xi_1} W^m \left(\frac{c_l - 2}{2} - \frac{4\partial_{\xi_2}\Theta^m}{((c_l-2)/4 - U_1^m - (\phi^m)')(1 - 2\phi^m/\xi_2/(3c_l+2))} - U_1^m - (\phi^m)'\right) =$$
$$\left(\frac{4((\phi^m)'' + \partial_{\xi_2} U_2^m)\partial_{\xi_2}\Theta^m + (c_l-2)\Theta_2^m/4}{((c_l-2)/4 - U_2^m - (\phi^m)')(1 - 2\phi^m/(\xi_2(3c_l+2)))} + U_2^m \partial_{\xi_2} W^m\right) \times$$
$$\frac{1}{1 - 2\phi^m/(\xi_2(3c_l+2))}.$$

So we have

$$\partial_{\xi_1} W^m \left(\frac{c_l - 2}{2} - \frac{4\partial_{\xi_1}\Theta^m}{((c_l-2)/4 - U_1^m - (\phi^m)')(1 - 2\phi^m/\xi_2/(3c_l+2))} - U_1^m - (\phi^m)'\right) \gg$$
$$\left(\frac{4((\phi^m)'' + \partial_{\xi_2} U_2^m)\partial_{\xi_2}\Theta^m + (c_l-2)\Theta_2^m/4}{((c_l-2)/4 - U_2^m - (\phi^m)')(1 - 2\phi^m/(\xi_2(3c_l+2)))} + U_2^m \partial_{\xi_2} W^m\right).$$

Then

$$\frac{c_1 - 2}{2}\partial_{\xi_1} W^m - (\phi^m)(\xi_2) - U_1^m \partial_{\xi_1} W^m - U_2^m \partial_{\xi_2} W^m \gg$$
$$\frac{4(\partial_{\xi_1} W^m + (\phi^m)'' + \partial_{\xi_2} U_2^m)\partial_{\xi_2}\Theta^m + (c_l-2)\Theta_2^m/4}{((c_l-2)/4 - U_1^m - (\phi^m)')(1 - 2\phi^m/\xi_2/(3c_l+2)}.$$

Using (3.2.14e), we have

$$\frac{c_1 - 2}{2}\partial_{\xi_1} W^m - \phi'(\xi_2) - U_1^m \partial_{\xi_1} W^m - U_2^m \partial_{\xi_2} W^m \gg$$
$$\frac{4\partial_{\xi_1} U_1^m \partial_{\xi_2}\Theta^m + (c_l-2)\Theta_2^m/4}{((c_l-2)/4 - U_1^m - (\phi^m)')(1 - 2\phi^m/\xi_2/(3c_l+2)}.$$

Note that $\partial_{\xi_1} U_1^m \gg U_1^m/\xi_1$, and plugging this into the right hand side of the above equation, we get that the right hand side majorizes $\Theta_{\xi_1}^m/\xi_1$. Finally, we get

$$\frac{c_l - 2}{2}\partial_{\xi_1} W^m \gg (\phi^m)'(\xi_2)\partial_{\xi_1} W^m + U_1^m \partial_{\xi_1} W^m + U_2^m \partial_{\xi_2} W^m + \partial_{\xi_2}\Theta^m/\xi_1.$$

Comparing this with (3.2.7b), and computing $F_{m-1,j}$ of both sides, we obtain

$$W_{m,0}^m \geq J_1 \geq |W_{m,0}|.$$

Assume now that $W_{m,j}^m \geq |W_{m,j}|$ for $j \leq p$. Then for $j = p+1$, if $J_1 > J_2$, we can prove $W_{m,p+1}^m \geq |W_{m,p+1}|$ following the same procedure as $j = 0$. If $J_2 > J_1$, then we can use the same technique as for Θ the case $I_2 > I_1$ to obtain that

$$W_{m,j}^m \geq |W_{m,j}|.$$

Then we consider $U^2_{m,j}$, and according to (3.2.9d), we have

$$U^2_{m,j} = \frac{(j+1)U^1(m-1,j+1) - \delta_{i1}(j+2)(j+1)\phi_{j+2} - W_{i,j}}{i+1}.$$

And according to (3.2.14e),

$$U^{m,2}_{m,j} = \frac{(j+1)U^{m,1}_{m-1,j+1} + \delta_{m1}(j+2)(j+1)\phi^m_{j+2} + mW^m_{m,j}}{m}.$$

Using $|W_{m,j}| \le W^m_{m,j}$ and the induction assumption (3.2.17), we get that

$$U^{m,2}_{m,j} \ge |U^2_{m,j}|, \quad j = 0, \dots \infty.$$

Then we consider $U^1_{m,j}$, and using (3.2.9c) and (3.2.14d), we have

$$U^1_{m,j} = \frac{-U^2_{m-1,j+1}}{1+m}, \quad U^{m,1}_{m,j} = \frac{U^{m,2}_{m-1,j+1}}{m}.$$

And according to the induction assumption (3.2.17),

$$|U^1_{m,j}| \le U^{m,1}_{m,j}$$

follows immediately.

Based on the induction process, we finally prove that

$$\Theta^m \gg \Theta, \quad W^m \gg W, \quad U^m_1 \gg U_1, \quad U^m_2 \gg U_2.$$

With this we conclude that the power series solutions that we construct converge, and there exist local analytic solutions to the self-similar equations (3.1.9). □

Recall that in our construction of the self-similar profiles for the CKY model in Chapeter 2, we extend the local power series solutions of the self-similar equations to the whole domain by solving an ODE. With the local power series solutions constructed in Theorem 3.2.1, one may attempt to extend the local solutions to the whole domain $R^+ \times R^+$ using the marching method employed for the CKY model. However, for the 2D Boussinesq system (3.1.9), the Biot-Savart law reads,

$$V = \nabla^\perp(-\Delta)^{-1}W. \tag{3.2.22}$$

And to extend the local power series solutions to the whole domain $R^+ \times R^+$ is ill-posed because of the elliptic nature of the Biot-Savart law (3.2.22).

In the rest part of this chapter we turn to investigating the spatial profiles in the singular solutions of the Boussinesq and axisymmetric Euler equations numerically.

3.3 The Dynamic Rescaling Formulation for the 2D Boussinesq System

In this section, we introduce the dynamic rescaling formulation for the 2D Boussinesq system and our numerical discretization of the equations. We show that the dynamic rescaling equations of the axisymmetric Euler equations are a perturbation to that of the 2D Boussinesq system, and the perturbation terms converge to zero exponentially fast in time. Then the stability of the self-similar profiles can justify the use of the dynamic rescaling equations of the 2D Boussinesq system to study the self-similar singularity of the axisymmetric Euler equations.

We add scaling terms $c_l(t)x\cdot\nabla$, $c_\theta(t)\theta$, $c_\omega(t)\omega$ to the Boussinesq equations

$$\omega_t + v\cdot\nabla\omega + c_l(t)x\cdot\nabla\omega = \theta_{x_1} + c_\omega(t)\omega, \tag{3.3.1a}$$

$$\theta_t + v\cdot\nabla\theta + c_l(t)x\cdot\nabla\theta = c_\theta(t)\theta, \tag{3.3.1b}$$

with Biot-Savart law the same as (3.1.5c),

$$v(x) = \nabla^\perp(-\Delta)^{-1}w. \tag{3.3.1c}$$

The scaling terms $c_l(t)x\cdot\nabla$ scale the solutions in the spatial direction, and the $c_\omega(t)$, $c_\theta(t)$ terms scale the amplitude of the solutions.

We need to choose the following condition for the scaling parameters

$$c_\theta(t) = c_l(t) + 2c_w(t), \tag{3.3.2}$$

according to the scaling-invariance (3.1.6) such that the dynamic rescaling equations are equivalent to the original equations (3.1.5). To be precise, let $\theta(x,t)$, $w(x,t)$, $v(x,t)$ be solutions to the Boussinesq system (3.1.5), then with (3.3.2),

$$C_\theta(t)\theta(C_l(t)x,\tau(t)),\ C_w(t)w(C_l(t)x,\tau(t)),\ C_u(t)u(C_l(t)x,\tau(t)), \tag{3.3.3a}$$

are solutions to the rescaling equations (3.3.1), where

$$\frac{d}{dt}\tau(t) = \exp(\int_0^t c_w(s)ds), \tag{3.3.3b}$$

$$C_\theta(t) = \exp(\int_0^t c_\theta(s)ds), \tag{3.3.3c}$$

$$C_w(t) = \exp(\int_0^t c_w(s)ds), \tag{3.3.3d}$$

$$C_l(t) = \exp(\int_0^t -c_l(s)ds). \tag{3.3.3e}$$

Namely, the solutions to (3.3.1) are simply rescalings of solutions to (3.1.5). From the relation (2.4.4), we can get that if the solutions of the rescaling equations (3.3.1) converge to a steady state, then correspondingly the solutions of the Boussinesq system will develop singularity in finite-time

$$T = \int_0^{+\infty} \exp(\int_0^{\tau} c_w(s)ds)d\tau.$$

The steady state of the dynamic rescaling equations (3.3.1) denoted by

$$\tilde{c_w} < 0,\ \tilde{c_l} > 0,\ \tilde{w},\ \tilde{\theta},\ \tilde{u}$$

corresponds to a solution to the self-similar equations (3.1.9),

$$c_l = -\tilde{c_l}/\tilde{c_w}, \quad W(\xi) = -\frac{1}{\tilde{c_w}}\tilde{w}(\xi), \quad \Theta(\xi) = \frac{1}{\tilde{c_w}^2}\tilde{\theta}(\xi). \tag{3.3.4}$$

The axisymmetric Euler equations (3.1.1) do not enjoy perfect scaling invariant property centered at the singularity point

$$\tilde{x} = (z,r) = (0,1),$$

and if we scale the solutions to the Euler equations $\omega_1(r,z)$, $u_1(r,z)$ as (3.3.3),

$$\hat{\omega}_1(x,t) = C_w(t)\omega_1(C_l(t)x + \tilde{x}, \tau(t)),\ \hat{u}_1(x,t) = C_u(t)u_1(C_l(t)x + \tilde{x}, \tau(t)),$$

then the equations satisfied by the rescaled solutions $\hat{\omega}_1(x,t)$, $\hat{u}_1(x,t)$ are defined on $x_1 \in R$, $x_2 \in (0, 2C_l(t)^{-1})$, and given by

$$\hat{u}_{1,t} + (c_l(t)x_2 + \hat{u}^r)\hat{u}_{1,x_2} + (c_l(t)x_1 + \hat{u}^z)\hat{u}_{1,x_1} = c_u(t)\hat{u} + 2\hat{u}_1\hat{\psi}_{1,x_1}C_l(t), \tag{3.3.5a}$$

$$\hat{\omega}_{1,t} + (c_l(t)x_2 + \hat{u}^r)\hat{\omega}_{1,x_2} + (c_l(t)x_1 + \hat{u}^z)\hat{\omega}_{1,x_1} = (\hat{u}_1^2)_{x_1} + c_w(t)\hat{\omega}, \tag{3.3.5b}$$

where

$$C_u(t) = \exp(\int_0^t c_u(s)ds). \tag{3.3.5c}$$

The velocity fields $\hat{u}^r$ and $\hat{u}^z$ in (3.3.5) are related to $\hat{\omega}$ through

$$-[\partial_{x_1x_1} + \partial_{x_2x_2} + \frac{3C_l(t)}{1 - C_l(t)x_2}\partial_{x_2}]\hat{\psi}_1 = \hat{\omega}_1, \tag{3.3.5d}$$

and

$$\hat{u}^r = (1 - C_l(t)x_2)\hat{\psi}_{1,x_1}, \quad \hat{u}_z = 2C_l(t)\hat{\psi}_1 - (1 - C_l(t)x_2)\hat{\psi}_{1,x_2}. \tag{3.3.5e}$$

By relating θ, v_1 and v_2 in (3.1.4) with $\hat{u}^2$, $\hat{u}^z$ and $\hat{u}^r$ in (3.3.5), we can see that (3.3.5) can be viewed as a perturbation to (3.1.4). The perturbation terms include

$$2\hat{u}_1\hat{\psi}_{1,x_1}C_l(t)$$

in (3.3.5a),

$$\frac{3C_l(t)}{1-C_l(t)x_2}\partial_{x_2}$$

in (3.3.5d),

$$C_l(t)x_2\hat{\psi}_{1,x_1}$$

in (3.3.5e), and

$$2C_l(t)\hat{\psi}_1 + C_l(t)x_2\psi_{1,x_2}$$

in (3.3.5e). They all converge to zero exponentially fast in time if

$$c_l(t) \to \tilde{c}_l > 0, \quad t \to +\infty,$$

because

$$C_l(t) = \exp(\int_0^t -c_l(s)ds) = O(\exp(-\tilde{c}_l t)), \quad t \to \infty.$$

Thus the dynamic rescaling equations of the axisymmetric Euler equations can be viewed as a perturbation to that of the Boussinesq system with the perturbation terms converging to zero exponentially fast in time.

Recall that for the Boussinesq system (3.1.5), the leading order of $\theta(x,t)$ in x_1 is preserved and we assume that the leading order of $\theta(x_1,x_2)$ in x_1 is $s = 2k$,

$$\theta(x_1,x_2) = O(x_1^s),\ x_1 \to 0, \quad \frac{d^{2k}}{dx_1^{2k}}\theta(0,0) > 0. \tag{3.3.6}$$

We can make the following change of variables

$$\theta(x,t) = x_1^{2k}\tilde{\theta}(x,t), \quad \omega(x,t) = x_1^{2k-1}\tilde{\omega}(x,t), \quad \tilde{\theta}(0,0) > 0. \tag{3.3.7a}$$

Due to the symmetry $\omega(x_1,x_2) = -\omega(-x_1,x_2)$ and the no-flow boundary condition, we have $v_1(0,x_2) = 0$, and thus we can make the change of variables

$$v_1(x_1,x_2,t) = x_1\tilde{v}_1. \tag{3.3.7b}$$

With (3.3.7), we get the following equations for $\tilde{\omega}$ and $\tilde{\theta}$,

$$\tilde{\omega}_t + (v + c_l x)\cdot\nabla\tilde{\omega} = 2k\tilde{\theta} + x_1\tilde{\theta}_{x_1} + (c_w - (2k-1)c_l - (2k-1)\tilde{v}_1)\tilde{w}, \tag{3.3.8a}$$

$$\tilde{\theta}_t + (v + c_l x)\cdot\nabla\tilde{\theta} = (-(2k-1)c_l + 2c_w - 2k\tilde{v}_1)\tilde{\theta}. \tag{3.3.8b}$$

Using the symmetry of ω, namely, $\omega(y_1,y_2) = -\omega(-y_1,y_2)$, and the solid boundary condition, we can write the Biot-Savart law (3.3.1c) in an integral form as

$$v_1(x_1,x_2) = \int_{\substack{[0,+\infty)\\ \times[0,+\infty)}} \frac{y_1^{2k-1}\tilde{\omega}(y_1,y_2)(x_2-y_2)}{(x_1-y_1)^2+(x_2-y_2)^2} + \frac{-y_1^{2k-1}\omega(y_1,y_2)(x_2-y_2)}{(x_1+y_1)^2+(x_2-y_2)^2} + \frac{-y_1^{2k-1}\omega(y_1,y_2)(x_2+y_2)}{(x_1-y_1)^2+(x_2+y_2)^2} + \frac{y_1^{2k-1}\omega(y_1,y_2)(x_2+y_2)}{(x_1+y_1)^2+(x_2+y_2)^2} dy_1 dy_2. \quad (3.3.8c)$$

$$v_2(x_1,x_2) = -\int_{\substack{[0,+\infty)\\ \times[0,+\infty)}} \frac{y_1^{2k-1}\tilde{\omega}(y_1,y_2)(x_1-y_1)}{(x_1-y_1)^2+(x_2-y_2)^2} + \frac{-y_1^{2k-1}\omega(y_1,y_2)(x_1+y_1)}{(x_1+y_1)^2+(x_2-y_2)^2} + \frac{-y_1^{2k-1}\omega(y_1,y_2)(x_1-y_1)}{(x_1-y_1)^2+(x_2+y_2)^2} + \frac{y_1^{2k-1}\omega(y_1,y_2)(x_1+y_1)}{(x_1+y_1)^2+(x_2+y_2)^2} dy_1 dy_2. \quad (3.3.8d)$$

$$\tilde{v}_1(0,x_2) = -4\int_{\substack{[0,+\infty)\\ \times[0,+\infty)}} \frac{y_1^{2k-1}\tilde{\omega}(y_1,y_2)(y_2-x_2)y_1}{[y_1^2+(y_2-x_2)^2]^2} + \frac{y_1^{2k-1}\tilde{\omega}(y_1,y_2)(x_2+y_2)y_1}{[y_1^2+(y_2+x_2)^2]^2} dy_1 dy_2. \quad (3.3.8e)$$

The finite-time singularity reported in [58] corresponds to the case that $k = 1$ in (3.3.6). We consider two cases $k = 1$ and $k > 1$ in this thesis, and show that the singular solutions for the two cases exhibit very different behaviors.

To investigate the stability of the self-similar profiles, we need to add perturbations to the steady state of (3.1.4), and see whether the solutions to the rescaling equations converge back to the steady state. The leading order of the perturbation $\delta\theta$ at the origin should be as least $2k$, and the change of variables (3.3.7) makes it easier to impose leading order property constraints on the perturbations.

To fix the scaling parameters in (3.3.8), we need suitable normalization conditions. For $k = 1$, we normalize $\tilde{\theta}(0,0,t)$ and $\tilde{\omega}(0,0,t)$, which correspond to the leading order derivatives of θ and ω in (3.1.4) at the origin,

$$\frac{d}{dt}\tilde{\theta}(0,0,t) = 0, \quad \frac{d}{dt}\tilde{\omega}(0,0,t) = 0. \quad (3.3.9)$$

The above condition leads to the following choice of the scaling parameters

$$c_w(t) = \tilde{v}_1(0,t) + 2k\frac{\tilde{\theta}(0,t)}{\tilde{\omega}(0,t)}, \quad c_l(t) = \frac{2-2k}{2k-1}\tilde{v}(0,t) + \frac{4k}{2k-1}\frac{\tilde{\theta}(0,t)}{\tilde{\omega}(0,t)}. \quad (3.3.10)$$

We will see in our numerical simulation that for the case $k = 1$ and with the choice of parameters (3.3.10), the solutions to the rescaling equation (3.3.8) converge to a steady state with $c_w < 0$, which implies that the solutions to (3.1.5) develop self-similar singularity in finite time. The steady state is also linearly stable, which implies that the Euler equations (3.1.1) develop finite-time singularity with the same blowup rate and self-similar profiles. However, for the case $k > 1$ with (3.3.9), we observe that the solution w blows up, and θ converges to zero.

Then we choose a different condition that normalizes the position where the maximum of w is attained and the value of θ at that point. With this condition, the solutions to the rescaling equations (3.3.8) converge to a steady state with singularity. To be specific, on the x_1 axis, w develops a δ function like shape, and θ develops a jump. Namely, there is a smaller scale generated, and the original Euler equations develop finite-time singularity at multiple spatial scales.

Considering the symmetry of the solutions with respect to x_1, the dynamic rescaling equations (3.3.8) can be viewed as defined on domain $[0,+\infty) \times [0,+\infty)$. In numerical computation, we need to restrict the equations to a finite computational domain $D_M = [0, M_1] \times [0, M_2]$. Since the velocity field (3.3.1c) on the computational finite-domain depends on the vorticity ω on the whole domain, we need to truncate the vorticity ω and introduce the following truncation operator

$$P_M f(x_1, x_2) = f(x_1, x_2) - \frac{x_1^2}{M^2} f(M, x_2) - \frac{x_2^2}{M^2} f(x_1, M) - \frac{x_1^2 x_2^2}{M^4} f(M, M). \quad (3.3.11)$$

Putting the truncation operator P_M in the dynamic rescaling equation of $\tilde{\omega}$, we get

$$\tilde{\omega}_t = P_M(-(v + c_l x) \cdot \nabla \tilde{\omega} + 2k\tilde{\theta} + x_1 \tilde{\theta}_{x_1} + (c_w - (2k-1)c_l - (2k-1)\tilde{v}_1)\tilde{w}), \quad (3.3.12a)$$

$$\tilde{\theta}_t = -(v + c_l x) \cdot \nabla \tilde{\theta} + (-(2k-1)c_l + 2c_w - 2k\tilde{v}_1)\tilde{\theta}. \quad (3.3.12b)$$

We discretize the computational domain $[0, M] \times [0, M]$ using Cartesian mesh,

$$x^{i,j} = (x_1^i, x_2^j), \quad 0 \le i \le N_1, \quad 0 \le i \le N_2, \quad (3.3.13)$$

and in computing the spatial derivatives in (3.3.8), we use the upwind scheme which is stable. Close to the steady state of the dynamic rescaling equations (3.3.8), there is no incoming characteristics on the boundary of the computational domain, so we do not need additional boundary conditions for $\tilde{\theta}(x,t)$ or $\tilde{\omega}(x,t)$.

To compute the velocity field $v(x,t) = \nabla^{\perp}(-\Delta)^{-1}\omega$, we cannot solve a Poisson equation to get the stream function $\psi = (-\Delta)^{-1}\omega$ and then take derivatives. This is because the dynamic rescaling equations (3.1.4) are defined on the whole domain, and when we restrict the equations to the computational domain D_M, we do not have appropriate boundary conditions for the stream function $\psi(x,t)$ on $M_1 \times [0, M_2]$ or $[0, M_1] \times M_2$. We instead employ the explicit integration formula (3.3.8c) and (3.3.8d) to compute the velocity field. To do so, we first recover $\tilde{w}(x)$ on the computational domain as piecewise bilinear function using its values on the discrete node points $x^{i,j}$. Plugging the piecewise bilinear function $\tilde{\omega}(x)$ in (3.3.8c) and (3.3.8d), we can compute the velocity field on the node points $x^{i,j}$ explicitly.

After the discretization procedure described above, we get an ODE system for the values of the $\tilde{\omega}$ and $\tilde{\theta}$ on the node points. We denote

$$\vec{\omega} = (\omega_1, \omega_2, \ldots \omega_{N_1 N_2})^T, \quad \vec{\theta} = (\theta_1, \theta_2, \ldots \theta_{N_1 N_2})^T, \tag{3.3.14a}$$

and get an ODE system

$$\frac{d}{dt}\vec{\omega} = F_{\omega}(\vec{\omega}, \vec{\theta}), \quad \frac{d}{dt}\vec{\theta} = F_{\theta}(\vec{\omega}, \vec{\theta}). \tag{3.3.14b}$$

The upwinding discretization of the spatial directives in (3.3.8), the Biot-Savart law (3.3.8c), (3.3.8d), the determination of the scaling parameters (3.3.10), and the projection operator (3.3.11), are all encoded in the right hand side F_{ω} and F_{θ}.

In the temporal direction, we discretize the ODE system (3.3.14) using a simple forward Euler scheme with the CFL number chosen to be 0.5.

The dynamic-rescaling formulation is essentially a nonlinear iteration scheme which converges to the self-similar profiles. To make the solutions converge, we need to choose the initial data for the rescaling system (3.3.8) close enough to the steady state. We first simulate the original equations (3.1.5) using initial data with the same leading order property, and then resale the solutions at a step close to the singularity time to get the initial data for the rescaling equations (3.3.8).

3.4 The Self-similar Singularity Scenario

The initial data for the finite-time Euler singularity reported in [58] is

$$u_1(r,z) = 100 e^{-30(1-r^2)^4} \sin(\frac{2\pi}{L} z).$$

Since θ in the Boussinesq system (3.1.5) corresponds to u_1^2 in the Euler equations (3.1.1), the finite-time singularity scenario in [58] corresponds to the case that the leading order of $\theta(x_1, x_2)$ in the x_1 direction is $s = 2$, (3.3.6).

In our simulation of the dynamic rescaling equations, we observe that in the near-field, the solutions have relatively fast variation, and away from the origin, the solutions have relatively slow variation. Such far field property of the self-similar profiles has been proved for the 1D CKY model in Chapter 2. So in the discretization of the dynamic rescaling equations in (3.3.13), we put relatively denser node points near the origin, and relatively coarser node points in the far field.

To be specific, we put half of the x_1^i in the near-field $[0, 10]$,

$$x_1^i = i \times h, \quad h = 20/N_1, \quad 0 \le i \le N_1/2. \tag{3.4.1a}$$

In the far-field, we make x_1^i grow exponentially fast

$$x_1^i = \exp(\log(x_1^{N_1/2}) + h(i - N_1/2)^{1.5}), \quad N_1/2 \le i \le N_1, \tag{3.4.1b}$$

where

$$h = \log(x_1^{N_1/2}) - \log(x_1^{N_1/2-1}).$$

In the x_2 direction, we use the same set of node points,

$$x_2^i = x_1^i, \quad 0 \le i \le N_2. \tag{3.4.1c}$$

We choose two sets of mesh in the simulation of (3.3.8). For the relatively coarse mesh, we choose $N_1 = N_2 = 40$, and for the finer mesh, we choose $N_1 = N_2 = 80$.

We choose $\tilde{\theta}(0,0) = \tilde{\omega}(0,0) = 1$ initially, then the scaling parameter $c_l(t)$ (3.3.10) is fixed and equal to 4. In our numerical simulation, we observe that the solutions to the dynamic rescaling equations converge to a steady state.

At the steady state, we have $\tilde{c}_w = -1.4295$ for the coarse mesh simulation; for the fine mesh simulation, we have $\tilde{c}_w = -1.4281$. According to (3.3.4), the resulting scaling exponents c_l in the self-similar ansatz (3.1.2) are

$$c_l = -\tilde{c}_l/\tilde{c}_w = 2.7982, \quad c_l = -\tilde{c}_l/\tilde{c}_w = 2.8009, \tag{3.4.2}$$

which are close to the scaling exponent obtained from the direct numerical simulation of the axisymmetric Euler equations in [58],

$$(2.7395, 2.9133).$$

The contour plot of the w at the steady state are given in Figure 3.2, which agrees with the configuration of the solution ω_1 in [58] for axisymmetric Euler equations.

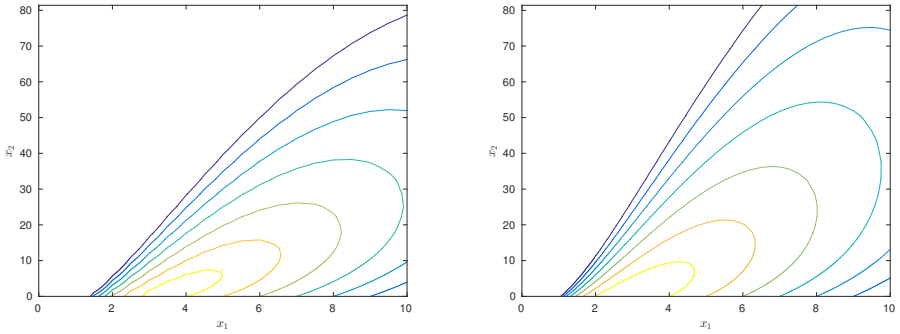

(a) $N_1 = N_2 = 40$. (b) $N_1 = N_2 = 80$.

Figure 3.2: Contour plot of w at the steady state.

At the steady state of the ODE system, we linearize the equations (3.3.14), and compute the Jacobian matrix given by

$$J = \begin{bmatrix} \nabla_\omega F_\omega & \nabla_\theta F_\omega \\ \nabla_\omega F_\theta & \nabla_\theta F_\theta \end{bmatrix}. \tag{3.4.3}$$

Since $\tilde{\theta}(0,0) = \tilde{\omega}(0,0) = 1$ and they remain constant in the ODE, we do not view them as degrees of freedom in computing (3.3.14) and (3.4.3).

The first several eigenvalues of the Jacobian matrix are plotted in Figure 3.3.

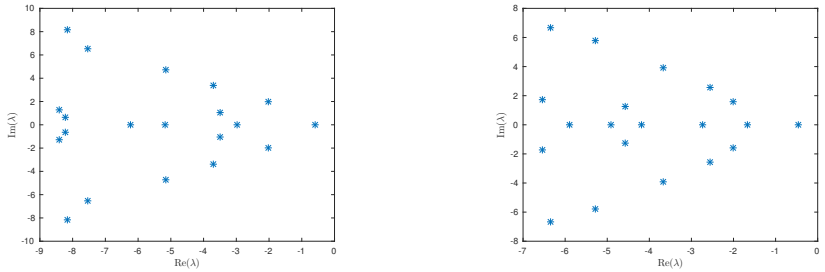

(a) $N_1 = N_2 = 40$. (b) $N_1 = N_2 = 80$.

Figure 3.3: Linearized stability of the self-similar profiles for $s = 2$.

We can see that the real parts of the first several eigenvalues of the Jacobian matrix J are all negative, which reflects the stability of the steady state and the self-similar profiles (3.3.1). Namely, staring from initial data close to the steady state, the solutions to the dynamic rescaling equations will converge back to the steady state.

As we have shown, the dynamic rescaling equations of the Euler equations can be viewed as a perturbation to that of the Boussinesq system (3.1.4), and the perturba-

tion terms converging to zero exponentially fast in time. So based on the stability of the self-similar profiles for the Boussinesq system, the solutions to the axisymmetric Euler equations will develop finite-time singularity with the same blow up rate and spatial profiles in the singular solutions. Thus our numerical results on the dynamic rescaling equations for the 2D Boussinesq system confirm the finite-time singularity reported in [58] for 3D axisymetric Euler equations.

3.5 The Finite-time Singularity with Multi-scale Feature

In the previous section, we consider initial conditions for the Boussinesq system with the leading order of θ in the x_1 direction being 2, and show that the solutions develop stable self-similar singularity. In the section, we consider the case that the leading order of θ in x_1 is larger or equal to 4. This finite-time singularity scenario has never been studied before, and we use two approaches to study the spatial profiles in the potentially singular solutions, namely, the direct numerical simulation of the system and the dynamic rescaling formulation. We observe that the spatial profiles in the singular solutions do not converge in this case, which means that the solutions do not develop self-similar singularity as the case $s = 2$.

Direct Numerical Simulation

We consider numerically solving the 2D Boussinesq system (3.1.5) on domain

$$D = (x_1, x_2) \in (-1, 1) \times (0, 1),$$

with no-flow boundary condition on ∂D. We consider the following initial condition

$$w(x_1, x_2) = \sin^3(\pi x_1)(1 - x_2)^3, \quad \theta(x_1, x_2) = (1 - \cos(\pi x_1))^2(1 - x_2)^2.$$

The leading order of θ at the order is 4 for the above initial data.

The numerical solutions are observed to develop finite-time singularity at the origin, and to resolve the singular solutions we use an adaptive mesh with more node points placed near the origin. The effective mesh size in our numerical computation is

$$2^{-18} \times 2^{-18}.$$

We use the first order upwind scheme to discretize the spatial derivatives in the equations; in the temporal direction, we use the forward Euler scheme. We choose the CFL number to be 0.5 to guarantee the stability of the simulation.

In the numerical simulation, we keep track of $\|w(t)\|_\infty$ which is attained on the x_1 axis, and the position where the maximum is attained, $C_l(t)$,

$$\|w(t)\|_\infty = w(C_l(t), 0).$$

Note that the maximum vorticity $\|w(t)\|_\infty$ characterizes the amplitude of the solutions, and $C_l(t)$ characterizes the length scale of the solutions.

We also record the solutions at several different time steps corresponding to different values of maximal vorticity $\|w(t)\|_\infty$ to get the spatial profiles in the solutions.

We first consider the blowup rate for the potentially singular solutions. We plot $\|w(t)\|_\infty^{-1}$ and $C_l(t)^{1/2}$ versus the time t in Figure 3.4.

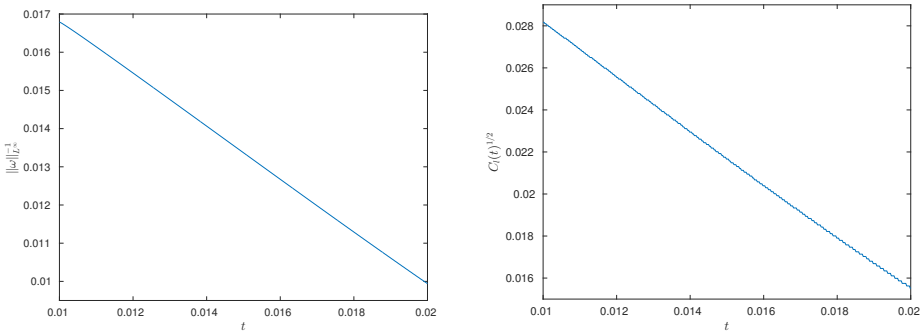

(a) Blowup of w.

(b) Decay of length scale.

Figure 3.4: Blow up rate for the solutions of the Boussinesq system with $s = 4$.

From the figure, we can see that $\|w(t)\|_\infty^{-1}$ and $C_l(t)^{1/2}$ both decay linearly with time, and thus we can conclude that $\|w(t)\|_\infty$ blows up approximately as

$$\|w(t)\|_\infty \approx O((T-t)^{-1}), \tag{3.5.1}$$

and the length scale of the solution decays approximately as

$$C_l(t) \approx O((T-t)^2). \tag{3.5.2}$$

The blowup rate (3.5.1) agrees with our self-similar ansatz (3.1.7),

$$w(x,t) = (T-t)^{-1} W\left(\frac{x}{(T-t)^{c_l}}\right).$$

For the length scale $C_l(t)$, (3.5.2) implies $c_l = 2$ in the ansazt (3.1.7).

Note that in our proof of the local existence of analytic self-similar profiles for the Boussinesq system in Theorem 3.2.1, we require that $c_l > 2$. And one can easily verify that for $c_l = 2$, the self-similar equations (3.1.9) have only trivial analytic solutions. However, this does not contradict our numerical results, because in the

case $s = 4$, the spatial profiles in the singular solutions develop singularity, and the solutions to the Boussinesq system do not blow up in a self-similar way.

At different time steps corresponding to different values of $\|w\|_\infty$, we rescale the solutions by normalizing the position where the maximal vorticity is attained, and the value of θ at that position to get the spatial profiles of the singular solutions. The profiles restricted on the x_1 axis are plotted in Figure 3.5. We can see that w develops a δ function-like shape, and θ tends to develop a jump.

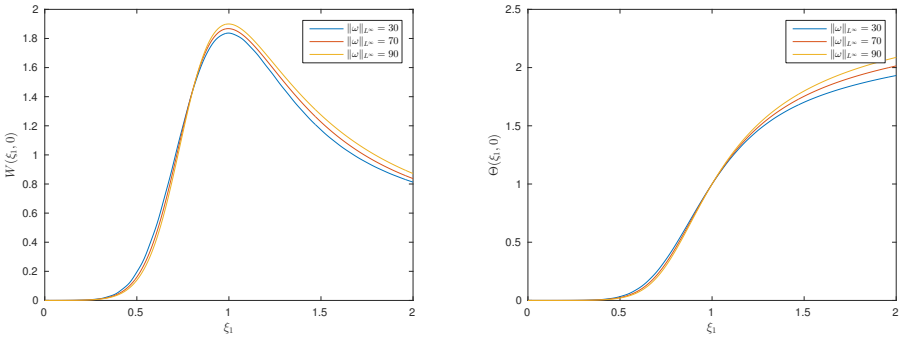

(a) Profile of w on the x_1 axis. (b) Profile of θ on the x_1 axis.

Figure 3.5: Spatial profiles of the Boussinesq system for $s = 4$.

In the next subsection, we continue to study the spatial profiles in the singular solutions of the PDE for the case $s = 4$ using the dynamic rescaling formulation.

Dynamic Rescaling Formulation

In the dynamic rescaling formulation, we first truncate the computation domain and restrict the equations on the finite truncated domain using the projection operator introduced in (3.3.11). Then we make the same change of variables (3.3.7) with $k = 1$ as what we have done for the case $s = 2$. The change of variables makes sure that the second order of derivatives of the solution θ in the x_1 direction will remain zero on the x_2 axis throughout the simulation.

Our preliminary numerical results suggest that the solutions to the rescaling equations develop a singularity at the point of maximal vorticity. So we need to use a relatively large number of node points near the singularity point, which makes the computation of the velocity field using the integral form of Biot-Savart law very expensive. We give up the integral formula (3.3.8) in this subsection.

In the case $s = 4$, to compute the velocity field on the truncated domain, we first

compute the stream function ϕ by solving the Poisson equation,

$$-\Delta\phi = w.$$

As we have explained in the previous section, we do not have the correct boundary condition for ϕ on the computational domain since ϕ does not decay to zero at infinity. In our computation, we will simply choose $\phi = 0$ as the boundary conditions for the Poisson equation. Using this Dirichlet boundary condition is equivalent to periodically extending the vorticity field w on the computational domain to the whole space and then employing the integral formula (3.3.8). The error in the velocity field introduced due to the periodic extension of the vorticity is smooth at the singularity point, and thus will not contribute to the interior singularity formation.

To fix the scaling parameters, we first normalize the leading order derivatives of the solutions and observe that w blows up and θ converges to zero.

Then we consider normalizing the position where the maximum of w is attained, and the value of θ at that position. In our computation, the maximum of w is attained on the x_1 axis, so we choose $c_l(t)$ and $c_w(t)$ such that

$$w(1,0,t) = \|w(t)\|_\infty, \quad \frac{d}{dt}\theta(1,0,t) = 0. \tag{3.5.3}$$

The above normalization condition leads to the following choice of scaling parameters in the dynamic rescaling equations,

$$c_l(t) = u_1(1,0), \quad c_l(t) + 2c_w(t) = 0.$$

In the simulation of the dynamic rescaling equations, we keep track of the scaling parameter $c_l(t)$ and $\|w(t)\|_\infty$, and record the solution in several time steps.

$c_l(t)$ and $\|w(t)\|_\infty$ versus t are plotted in Figure 3.6. We can see that and the scaling parameter $c_l(t)$ seems to converge and $\|w(t)\|_\infty$ is increasing. As we refine the mesh, we observe that the maximal $\|w(t)\|_\infty$ keeps increasing, which $c_l(t)$ remains the same. Thus we conjecture that for the case that $s = 4$, with the normalization condition (3.5.3), $c_l(t)$ converges, and $\|w\|_\infty$ blows up with time.

We restrict the solutions to the dynamic rescaling equations to the x_1 axis, and at different time steps, the solutions are plotted in Figure 3.7. We observe that the solution w blows up at $x_1 = 1$, and the θ solution develops a jump at $x_1 = 1$.

Due to the formation of singularity in the dynamic rescaling equations, it is hard to numerically resolve the solutions. In our simulation, after we discretize the rescaling equations in the spatial direction using a fixed mesh, we obtain an ODE system.

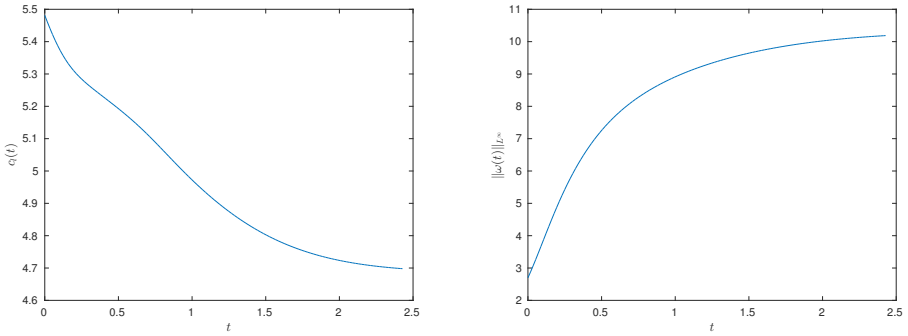

(a) $c_l(t)$. (b) $\|w(t)\|_\infty$.

Figure 3.6: Evolution of the solutions to the dynamic rescaling equations.

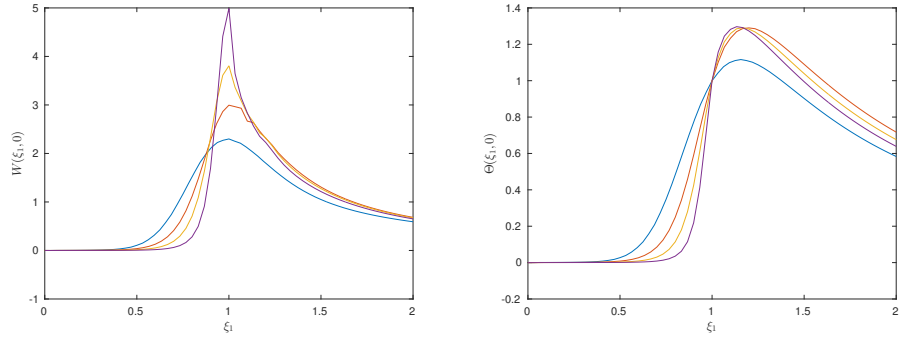

(a) $w(x_1,0)$. (b) $\theta(x_1,0)$.

Figure 3.7: Evolution of the solutions to the dynamic rescaling equations.

Numerically, we observe that the solutions to the discretized ODE system converge, which reflects the stability of this singularity scenario. However, we would like to comment that due to the formation of the singularity, the numerical solutions of the rescaling equations lose accuracy before they convergence to the steady state.

The steady state of the discretized system is visualized in Figure 3.8.

We can see that θ converges to a rarefaction wave-like solution. On the left side θ vanishes, and on the right side θ is constant and equal to 1. There exists a smooth transition region in between. The formation of this rarefaction wave like steady state is related to the velocity field in the rescaling equations,

$$v(x) + c_l x.$$

On the x_1 axis, $v_1(x) + c_l x_1$ positive except the singularity point,

$$v_1(x_1^*,0) + c_l x_1^* = 0; \quad v_1(x_1,0) + c_l x_1 > 0, \quad x_1 \neq x_1^*.$$

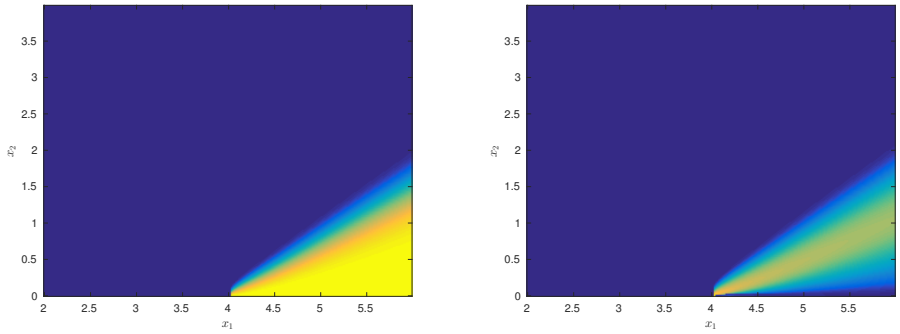

(a) θ. (b) w.

Figure 3.8: Steady state of the discretized dynamic rescaling equations.

Then according to the equation

$$(v + c_l(t)x) \cdot \nabla\theta = 0,$$

the characteristics go to the left on both sides of the singularity point x_1^*, and thus

$$\theta(x_1, 0) = \theta(0, 0), \quad 0 < x_1 < x_1^*,$$

and

$$\theta(x_1, 0) = \theta(x_1^*, 0), \quad x_1^* < x_1 < +\infty,$$

which can explain the jump of θ at the singularity point.

At the steady state w develops a delta-function like shape, and it seems to be supported on the transition region of θ, and decreases away from the x_1 axis.

To sum up, for the case $s = 4$, the profiles in the singular solution develop singularity themselves. Note that the profiles are already rescalings of the singular solutions, and the singularity in the profiles means that there is a smaller scale generated in the singular solutions. Thus the solutions to the 2D Boussinesq system (and Euler equations) develop finite-time singularity at multiple spatial scales in the case $s = 4$, which is very different from the self-similar singularity scenario observed for $s = 2$. This multi-scale singularity scenario is depicted in Figure 3.9. Such Euler singularity scenario has never been observed before in the literature.

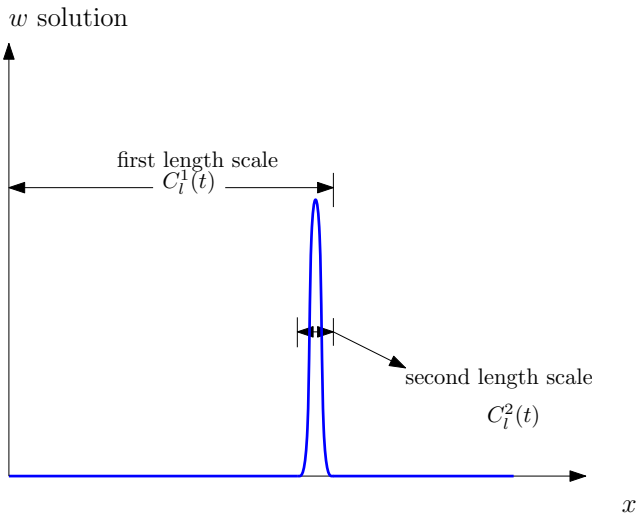

Figure 3.9: Finite-time singularity with multi-scale feature.

Chapter 4

SINGULARITY OF A FAMILY OF 3D MODELS FOR THE 3D EULER EQUATIONS

4.1 The Effect of Convection and the Derivation of the Models

In the 3D Euler and Navier-Stokes equations,

$$\omega_t + u \cdot \nabla\omega = \omega \cdot \nabla u + \Delta\omega,$$

due to the incompressibility condition of the velocity field,

$$\nabla \cdot u = 0,$$

the convection terms $u \cdot \nabla\omega$ have no contribution in energy estimates of the equations. The reason is that when we multiple by ω on both sides of the equations and then do integration by part, the convection terms vanish.

However, previous analytical and numerical results have shown the stabilizing effect of the convection terms. Hou and Li [38] proposed a 1D model of the 3D axisymmetric Euler and Navier-Stokes equations on the symmetric axis,

$$\tilde{u}_t + 2\tilde{\phi}\tilde{u}_z = 2\tilde{\phi}_z\tilde{u} + \nu\Delta\tilde{u}, \tag{4.1.1a}$$

$$\tilde{w}_t + 2\tilde{\phi}\tilde{w}_z = (\tilde{u}^2)_z + \nu\Delta\tilde{w}, \tag{4.1.1b}$$

which is closed by Biot-Savart law

$$-\tilde{\phi}_{zz} = \tilde{w}. \tag{4.1.1c}$$

The above 1D model is obtained by restricting the 3D axisymmetric Euler equations on the symmetric axis, and it is exact in the sense that one can obtain a family of solutions (with infinite energy) of the 3D Navier-Stokes (Euler) equations based on the solution of the 1D model. Hou and Li showed that the convection term in the model (4.1.1) has an amazing stabilizing effect in the sense that one of the terms obtained from differentiating the convection term cancels exactly one of the nonlinear stretching terms. And they obtained a Lyapunov function of the form $(\tilde{u}_z^2 + \tilde{w}^2)$ which satisfies a maximal principle. Based on this *a priori estimate*, they proved that the 1D model, viscid or inviscid, is globally well-posed.

By taking a Lagrangian point of view, Deng, Hou and Yu [19, 20] obtained a localized non-blowup criterion that refines the criterion of Constantin, Fefferman and Majda [18], which also reflects the importance of the convection terms, since the Lagrange point of view takes the convection terms into account naturally.

To further demonstrate the stabilizing effect, Hou and Lei [37] proposed a 3D model of the 3D axisymmetric Euler and Navier-Stokes equations,

$$u_{1,t} = 2u_1\psi_{1,z} + \nu\Delta_5 u_1, \tag{4.1.2a}$$

$$\omega_{1,t} = (u_1^2)_z + \nu\Delta_5\omega_1, \tag{4.1.2b}$$

$$w_1 = -\Delta_5\psi_1, \tag{4.1.2c}$$

which is obtained simply by dropping the convection terms in the 3D axisymmetric Euler and Navier-Stokes equations introduced in (3.1.1).

With appropriate Dirichlet boundary conditions, this 3D model enjoys the energy conservation property, and shares several non-blowup criteria and the partial regularity result [36] with the Euler and Navier-Stokes equations.

It is proved by Hou, Wang, et al [42, 43] that under certain Robin-Dirichlet boundary condition, which does not preserve energy, the model (4.1.2) can develop finite-time singularity. And numerical results suggest that the 3D model (4.1.2) with natural boundary condition can also blow up. Moreover, when the convection terms are added back to the model, the blow up scenario is destroyed immediately.

In this chapter of the thesis, we study a family of 3D models derived by changing the amplitude of the convection terms in the axisymmetric Euler and Navier-Stokes equations (3.1.1) by a factor of ϵ. We arrive at

$$u_{1,t} + \epsilon u^r u_{1,r} + \epsilon u^z u_{1,z} = 2u_1\psi_{1,z} + \nu\Delta u_1, \tag{4.1.3a}$$

$$\omega_{1,t} + \epsilon u^r \omega_{1,r} + \epsilon u^z \omega_{1,z} = (u_1^2)_z + \nu\Delta\omega_1, \tag{4.1.3b}$$

$$-[\partial_r^2 + (3/r)\partial_r + \partial_z^2]\psi_1 = \omega_1, \tag{4.1.3c}$$

where u^r and u^z are related to the stream function ψ_1 by

$$u^r = -r\psi_{1,z}, \quad u^z = 2\psi_1 + r\psi_{1,r}. \tag{4.1.3d}$$

The case $\epsilon = 1$ corresponds to the 3D Euler and Navier-Stokes equations, while the case $\epsilon = 0$ corresponds to the model proposed by Hou and Lei [37]. We will show that this family of models enjoy a similar energy identity as the Euler and

Navier-Stokes equations. The partial regularity result and a non-blowup criterion for the Navier-Stokes equations also apply to this family of 3D viscous models.

We propose this family of models to further investigate the potential stabilizing effect of the convection terms. We numerically study the solutions of this family of inviscid models using both direct numerical simulation and the dynamic rescaling formulation. Our numerical results suggest that the model develops finite-time singularity for small ϵ, and the solutions enjoy self-similar structure with the center of singular region travelling. We refer to this singularity scenario as the travelling wave self-similar singularity scenario. As we increase the amplitude the convection terms, we observe that this singularity scenario is destroyed, which reflects the subtle balance between the convection terms and the vortex stretching terms.

In this chapter, we first prove several results concerning the regularity of the new 3D models to show the qualitative similarity of these models with the Euler and Navier-Stokes equations. Then we present our numerical results for this family of models using direct numerical simulation and the dynamic rescaling formulation.

4.2 Some Theoretical Results about the New 3D Models

The Laplace operator in the diffusion terms and the Biot-Savart law of the model (4.1.3) is a five-dimensional Laplace operator, and we can view the 3D model as a system defined on $y = (y_1, y_2, \cdots y_4, z) \in R^5$ with

$$r = (y_1^2 + y_2^2 + \cdots y_4^2)^{1/2},$$

and the solutions being symmetric with respect to $y_1, \cdots y_4$.

We denote the velocity field of 3D model as

$$u = ru^1 e_\theta + \epsilon u^r e_r + \epsilon u^z e_z. \tag{4.2.1}$$

Then one can easily verify that

$$\nabla_x \cdot u = \partial_r(\epsilon r u^r) + \partial_z(\epsilon r u^z) = 0.$$

Namely, the 3D velocity field of the fluid is divergence free.

This inviscid models enjoy the following scaling invariance property,

$$u_1(x,t) \to \frac{1}{\tau} u_1\left(\frac{x}{\lambda}, \quad \frac{t}{\tau}\right), \omega_1(x,t) \to \frac{1}{\lambda\tau}\omega_1\left(\frac{x}{\lambda}, \frac{t}{\tau}\right). \tag{4.2.2}$$

And for the viscous model $\nu > 0$, we have the following scaling invariance,

$$u_1(x,t) \to \frac{1}{\tau} u_1\left(\frac{x}{\tau^{1/2}}, \frac{t}{\tau}\right), \quad \omega_1(x,t) \to \tau^{-3/2}\omega_1\left(\frac{x}{\tau^{1/2}}, \frac{t}{\tau}\right). \tag{4.2.3}$$

The new 3D model enjoys the following energy identity for $\epsilon < 2$.

Theorem 4.2.1. *For a smooth solution to the 3D model* (4.1.3)*, ψ_1 and u_1,*

$$\frac{1}{2}\frac{d}{dt}\int_{-\infty}^{\infty}\int_{0}^{\infty}(|u_1|^2 + (2-\epsilon)|\nabla_y\psi_1|^2)r^3drdz + \nu\int_{-\infty}^{\infty}\int_{0}^{\infty}(|\nabla_y u_1|^2 + (2-\epsilon)|\Delta_y\psi_1|^2)r^3drdz = 0. \quad (4.2.4)$$

We denote the energy functional in the above theorem as E_ϵ,

$$E_\epsilon = \int_{-\infty}^{\infty}\int_{0}^{\infty}(|u_1|^2 + (2-\epsilon)|\nabla_y\psi_1|^2)r^3drdz. \quad (4.2.5)$$

For $\epsilon = 1$, E_1 is the same as the L^2 energy of the Euler and Navier-Stokes equations.

For $\epsilon < 2$, E_ϵ is equivalent to the L^2 energy of Euler and Navier-Stokes equations,

$$\min(1, 2-\epsilon)E_1 \le E_\epsilon \le \max(1, 2-\epsilon)E_1.$$

Proof. Multiplying the first equation (4.1.3a) by $u_1 r^3$, and integrating over $drdz$, which is equivalent to the 5D Lebesgue measure dy, we get

$$\frac{1}{2}\frac{d}{dt}\int u_1^2 r^3 drdz + \frac{1}{2}\int \epsilon(u^r r)r^2(u_1^2)_r drdz + \frac{1}{2}\int \epsilon(u^z r)r^2(u_1^2)_z drdz = \int 2u_1^2\phi_{1,z}r^3 drdz - \nu\int |\nabla_y u_1|^2 r^3 drdz.$$

For the convection terms, we use integration by part, and the fact that

$$(ru^r)_r + (zu^z)_z = 0, \quad (4.2.6)$$

to get

$$\frac{1}{2}\int \epsilon(u^r r)r^2(u_1^2)_r drdz + \frac{1}{2}\int \epsilon(u^z r)r^2(u_1^2)_z = -\int \epsilon u^r r^2 u_1^2 drdz.$$

Then we have

$$\frac{1}{2}\frac{d}{dt}\int u_1^2 r^3 drdz - \int \epsilon u^r r^2 u_1^2 drdz = \int 2u_1^2\phi_{1,z}r^3 drdz - \nu\int |\nabla_y u_1|^2 r^3 drdz.$$

Then using $u^r = -r\psi_{1,z}$, we get that

$$\frac{1}{2}\frac{d}{dt}\int u_1^2 r^3 drdz = \int (2-\epsilon)u_1^2\phi_{1,z}r^3 drdz - \nu\int |\nabla_y u_1|^2 r^3 drdz. \quad (4.2.7)$$

Multiplying (4.1.3b) by $\psi_1 r^3$, and using the fact that $-\Delta\psi_1 = \omega_1$, we have

$$\frac{1}{2}\frac{d}{dt}\int |\nabla\psi_1|^2 r^3 dr dz + \int \epsilon(u^r r)\omega_{1,r}\psi_1 r^2 dr dz + \int \epsilon(u^z r)\omega_{1,z}\psi_1 r^2 dr dz$$
$$= -\int u_1^2 \psi_{1,z} r^3 dr dz - \nu \int |\Delta_y \psi_1|^2 r^3 dr dz.$$

Using the divergence free condition (4.2.6), the Biot-Savart law (4.1.3d), and integration by part, we can show that the convection terms vanish,

$$\int \epsilon(u^r r)\omega_{1,r}\psi_1 r^2 dr dz + \int \epsilon(u^z r)\omega_{1,z}\psi_1 r^2 dr dz = 0.$$

Then we have

$$\frac{1}{2}\frac{d}{dt}\int |\nabla\psi_1|^2 r^3 dr dz = -\int u_1^2 \psi_{1,z} r^3 dr dz - \nu \int |\Delta_y \psi_1|^2 r^3 dr dz. \tag{4.2.8}$$

Adding up (4.2.7) and (4.2.8), we can complete the proof. □

For the viscous model, we have the following Prodi-Serrin type criterion.

Theorem 4.2.2. *Consider smooth solutions to the 3D model* (4.1.3) *with* $\nu > 0$*.*

$$\frac{3}{p} + \frac{2}{q} \le 1, \quad 3 < p \le +\infty.$$

Then if

$$\|v\|_{L^q(L^p(R^3),[0,T))} < +\infty,$$

the solutions can be smoothly extended beyond T*.*

Note that the quantity $\|v\|_{L^q(L^p(R^3),[0,T))}$ is critical with respect to the scaling (4.2.3). The proof is of the theorem is similar to that in [37], and we omit the details here.

Moreover, one can obtain the following partial regularity result for suitable weak solutions of the 3D viscous models in the same spirit as [9, 57].

Theorem 4.2.3. *For* $\nu > 0$*, there exist global suitable weak solutions to* (4.1.3)*. And for a suitable weak solution on an open set in space-time, the one-dimensional Hausdorff measure of the associated singular set if zero.*

The proof of the above theorem is similar to that in [36].

4.3 Numerical Study of the Family of Inviscid Models

In this section, we study the finite-time singularity for the inviscid models numerically. We use two approaches, direct numerical simulation and the dynamic rescaling formulation. We focus on the following range of ϵ

$$\epsilon \in [0, 1]$$

to investigate the potential stabilizing effect of convection, since $\epsilon = 1$ corresponds to the Euler equations and $\epsilon = 0$ corresponds the model of Hou and Lei [37].

We first numerically study the family of models (4.1.3) with $\epsilon = 0$ using direct simulation and the following choice of initial data,

$$w(r, z) = 0, \quad u(r, z) = 300 \sin^{20}(\pi z)(r^2 - 1)^{40}.$$

The problem is numerically solved on the domain $(r, z) \in D = (0, 1) \times (0, 1)$, with

$$1024 \times 1024$$

degrees of freedom. In the spatial direction, we use a upwind scheme to discretize the derivatives, and in the temporal direction, we use the forward Euler method with the CFL number $\nu = 0.5$. We employ a no-blow boundary condition since we are investigating the inviscid case, which leads to the Dirichlet boundary condition

$$\psi_1|_{\partial D} = 0,$$

for the Poisson equation (4.1.3c).

We observe that the numerical solutions develop singularity in finite time. The center of the singular region is not stationary but travelling along the symmetric axis. We use an adaptive mesh in the simulation, which puts a certain portion of node points in the singular region of the solutions.

We save the numerical solutions for $\epsilon = 0$ at a time close to the singularity time T, and use them as initial conditions to numerically solve the family of models. We observe that for small ϵ, the solutions still develop self-similar singularity with the center of the singular region travelling. But for ϵ larger than certain critical value, the self-similar singularity scenario will be destroyed.

We keep track of the maximum norm of u_1, $\|u_1(t)\|_\infty$, in the simulation, and the decay of $\|u_1(t)\|_\infty^{-1}$ versus time is plotted in Figure 4.1.

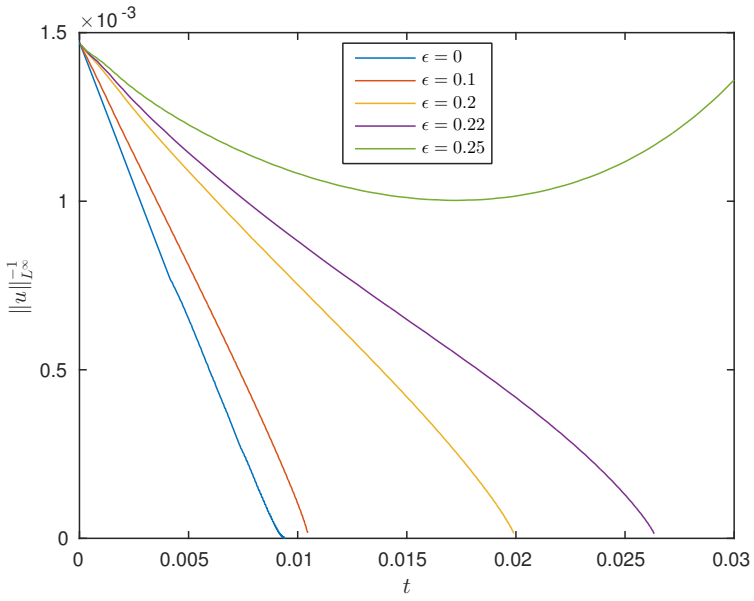

Figure 4.1: Blowup of the family of models for small ϵ.

We can see that for small ϵ, $\|u_1(t)\|_\infty^{-1}$ is close to a straight line, and thus the solutions develop singularity with approximately the following asymptotic rate,

$$\|u_1(t)\|_\infty = O((T-t)^{-1}). \tag{4.3.1}$$

According to the scaling invariance of the equations (4.2.2), (4.3.1) is the only possible blowup rate for $\|u_t(t)\|_\infty$ in self-similar singularity.

For $\epsilon = 0$, we record the numerical solutions at different time steps corresponding to different values of $\|\omega_1\|_\infty$. Since the center of the singular region is travelling, we first shift the center of singularity to the origin, and then normalize the maximum of u_1 and ω_1. Namely, we choose λ, τ and c such that

$$u_1^{\lambda,\tau} = \frac{1}{\tau} u_1\left(\frac{x-c}{\lambda}, t\right), \quad \omega_1^{\lambda,\tau} = \frac{1}{\lambda\tau}\omega_1\left(\frac{x-c}{\lambda}, t\right),$$

satisfy

$$\omega_1^{\lambda,\mu}(0,0) = 0, \quad \|\omega_1^{\lambda,\mu}\|_\infty = 1, \quad \|u_1^{\lambda,\mu}\|_\infty = 1.$$

The normalized solutions are plotted in Figure 4.2.

We can see that the normalized solutions at different time steps seem to converge, which implies the self-similar singularity of the 3D model.

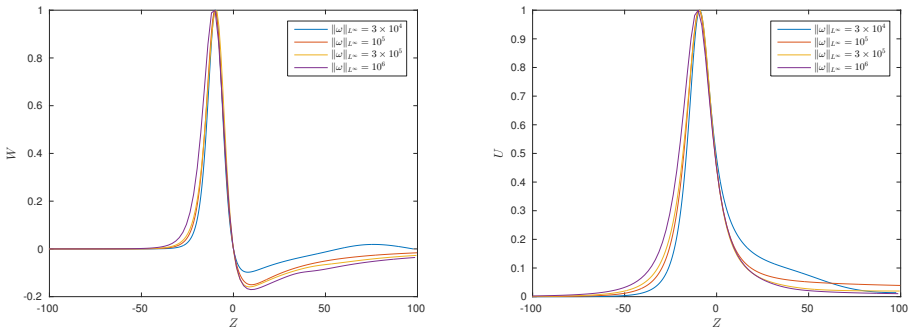

(a) $w(0,z)$. (b) $u(0,z)$.

Figure 4.2: Profiles of the singular solutions in direct numerical simulation.

Similar behaviors are observed for the models with small ϵ. The critical value of ϵ for the regularity of the family of 3D models seem to be close to

$$\epsilon_c = 0.22. \tag{4.3.2}$$

Namely, for $\epsilon < \epsilon_c$, the solutions develop travelling wave like self-similar singularity, and for $\epsilon > \epsilon_c$, the self-similar singularity scenario is destroyed.

The self-similar singularity of the solutions is different from those for the 2D Boussinesq system (3D axisymmetiric Euler) or the two 1D models in the sense that the center of the singularity region is not stationary but travelling.

Based on the behaviors of the singular solutions observed in our simulation, we make the following self-similar ansatz for the singular solutions,

$$u(r,z,t) = (T-t)^{c_u} U\left(\frac{r}{(T-t)^{c_l}}, \frac{z-z(t)}{(T-t)^{c_l}}\right), \tag{4.3.3a}$$

$$w(r,z,t) = (T-t)^{c_w} W\left(\frac{r}{(T-t)^{c_l}}, \frac{z-z(t)}{(T-t)^{c_l}}\right). \tag{4.3.3b}$$

Note that the above ansatz of the singular solutions allows the center of the singularity, $(r,z) = (0,z(t))$, to travel along the symmetric axis.

Plugging the above ansatz into the 3D models (4.1.3) and matching the power of $(T-t)$ for each term, one gets the following condition for the scaling exponents,

$$c_u = -1, \quad c_w = -1 - c_l,$$

and the following travelling rate of the singular region,

$$\frac{d}{dt} z(t) = C(T-t)^{c_l}.$$

The following self-similar equations govern the spatial profiles in (4.3.3),

$$U + (c_l r + \epsilon U^r)U_r + (c + c_l z + \epsilon U^z)U_z = 2U\Psi_z, \tag{4.3.4a}$$

$$(c_l + 1)W + (c_l r + \epsilon U^r)W_r + (c + c_l z + \epsilon U^z)W_z = (U^2)_z, \tag{4.3.4b}$$

$$-[\partial_r^2 + (3/r)\partial_r + \partial_z^2]\Psi_1 = W. \tag{4.3.4c}$$

Using a scaling of the profiles, one can set the travelling speed c in (4.3.4) as one. But the scaling exponent c_l cannot be determined simply by dimensional analysis. Thus the self-similar singularity is again of the second kind, and we next use the dynamic rescaling formulation to further study the self-similar profiles.

4.4 Stability of the Travelling Wave Self-similar Singularity

In this section, we use the dynamic rescaling formulation to study the spatial profiles in the singular solutions of the 3D inviscid models (4.1.3). Since the center of the singularity is travelling along the symmetric axis, to recover the spatial profiles in the singular solutions, one needs to shift the singular solutions to a fixed point. So we consider adding a convection velocity term, in addition to the stretching and the scaling terms introduced for the 2D Boussinesq system, to the 3D models (4.1.3) and get the following dynamic rescaling equations,

$$u_{1,t} + (c_l r + \epsilon u^r)u_{1,r} + (c_l z + \epsilon u^z + c)u_{1,z} = 2u_1\psi_{1,z} + c_u u_1, \tag{4.4.1a}$$

$$\omega_{1,t} + (c_l r + \epsilon u^r)\omega_{1,r} + (c_l z + \epsilon u^z + c)\omega_{1,z} = (u_1^2)_z + c_w w, \tag{4.4.1b}$$

$$-[\partial_r^2 + (3/r)\partial_r + \partial_z^2]\psi_1 = \omega_1, \tag{4.4.1c}$$

where u^r and u^z are related to the stream function ψ_1 by

$$u^r = -r\psi_{1,z}, \quad u^z = 2\psi_1 + r\psi_{1,r}.$$

The $c_l(t)r\partial_r$, $c_l(t)z\partial_z$ terms stretch the solutions in the spatial direction; the $c(t)\partial_z$ term shifts the solutions along the symmetric axis; the $c_w(t)w$ and $c_u(t)u$ terms rescale the solutions ω_1 and u_1 in amplitude respectively.

We need to choose the following condition for the scaling parameters in (4.4.1),

$$c_w(t) = c_u(t) - c_l(t)$$

according to the scaling invariance property of the inviscid models, (4.2.2), such that the dynamic rescaling equations are equivalent to the 3D models (4.1.3).

To fix the scaling parameters in the above dynamic rescaling formulation, we need suitable normalization conditions. We first fix the center of the solution at the origin.

In another word, we choose $c(t)$ in (4.4.1) such that

$$\omega_1(0,0,t) = 0.$$

The above condition leads to

$$c = \frac{(u_1^2)_z - \epsilon u^r \omega_{1,r} - \epsilon u^z \omega_{1,z}}{\omega_{1,z}}.$$

Then we choose $c_l(t)$ and $c_u(t)$ to normalize the derivatives of w and the value of u at the origin. Namely, we choose $c_l(t)$ and $c_u(t)$ such that

$$\frac{d}{dt} w_z(0,0) = 0, \quad \frac{d}{dt} u(0,0) = 0.$$

The dynamic rescaling equations (4.4.1) are defined on unbounded domain

$$(r,z) \in R^+ \times R,$$

and in our numerical computation, we first truncate the computation domain to

$$(r,z) \in D = [0,50] \times [-50,50].$$

Note that to compute the velocity field u^r and u^z (4.1.3d), one needs to solve the Poisson equation (4.1.3c). However, we do not have appropriate boundary conditions for the stream function ψ_1 on the boundary of the domain. In our simulation, we simply choose a zero boundary condition, which is equivalent to extending ω_1 in (4.1.3c) periodically. The error introduced by this truncation and the artificial boundary condition is small if the truncated computation domain D is large enough.

We use the numerical solutions to the models with $\epsilon = 0$ close to the singularity time as initial conditions for the dynamic rescaling system (4.4.1).

In our simulation of the dynamic rescaling equations, we observe that for small ϵ

$$\epsilon < 0.19, \tag{4.4.2}$$

the rescaling solutions converge to a steady state, which implies that the solutions to the inviscid models (4.1.3) develop self-similar singularity.

Next we study the stability of the self-similar profiles, and we only consider the case $\epsilon = 0$ here. After discretization, the dynamic rescaling equations (4.4.1) become an ODE system, and at the steady state of the ODE system, we compute the Jacobian

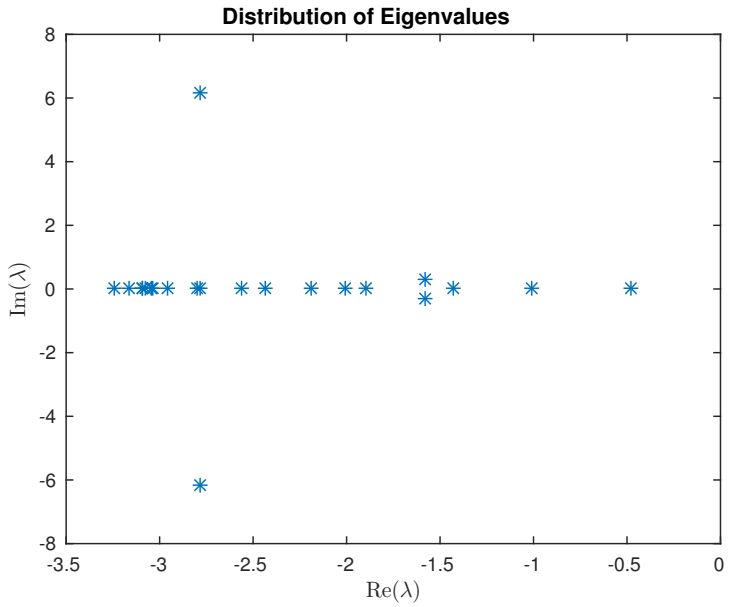

Figure 4.3: Eigenvalues of the Jacobian matrix at the steady state for $\epsilon = 0$.

matrix of its right hand side. The first several eigenvalues of the Jacobian matrix are plotted in Figure 4.3. We can see that the eigenvalues have negative real part, which demonstrates the stability of the travelling wave self-similar singularity.

Note that the critical value of ϵ for the dynamic rescaling equations to converge, (4.4.2), is slightly different to the critical value for finite-time singularity that we obtain from direct numerical simulation (4.3.2). The reason is that in the dynamic rescaling formulation, we need to truncate the computational domain and use an artificial boundary condition for ψ_1 in (4.1.3c), which introduces additional error.

For different ϵ, the self-similar profiles for the 3D inviscid models (4.1.3) restricted on the symmetric axis are plotted in Figure 4.4, and the scaling exponents c_l are listed in Table 4.1. Recall that the inviscid models enjoy the conversation of energy (4.2.4), and based on the self-similar ansatz that we made (4.3.3), the energy functional (4.2.5) on a local region for the self-similar variable ξ scales as

$$E_\epsilon = O((T-t)^{5c_l/2-1}).$$

Thus we have the following constraint for c_l,

$$5c_l/2 - 1 > 0, \quad c_l > 0.4.$$

From the table, we can see that for larger ϵ, the scaling exponent c_l becomes smaller, which means that the solutions blowup slower.

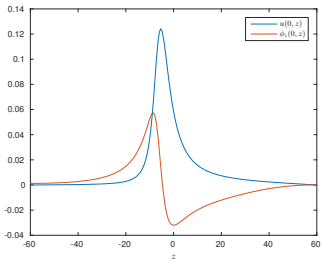

(a) $\epsilon = 0.025$.

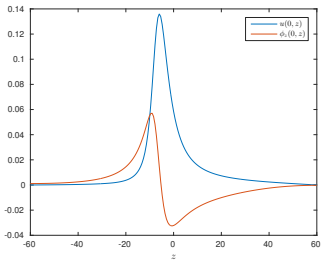

(b) $\epsilon = 0.100$.

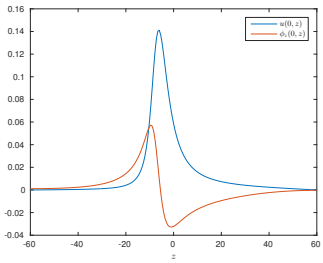

(c) $\epsilon = 0.125$.

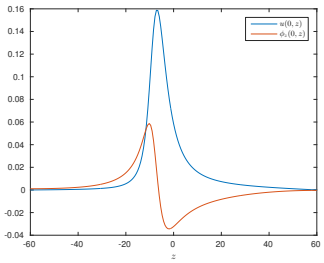

(d) $\epsilon = 0.185$.

Figure 4.4: Self-similar profiles restricted on the symmetric axis.

ϵ	0.025	0.1000	0.125	0.185
c_l	1.009	0.908	0.880	0.830

Table 4.1: The scaling exponents in the self-similar singularity for different ϵ.

Chapter 5

CONCLUDING DISCUSSIONS

Self-similarity plays an important role in the singularity formation of nonlinear PDEs, and in this thesis, the second kind self-similar singularity of the 3D axisymmetric Euler equations and simplified models, including two 1D models and a family of 3D models, are studied both analytically and numerically.

The 1D CKY model and the HL model are motivated by the numerical computation of Luo and Hou in [58], and approximate the dynamics of the axisymmetric Euler equations on the solid boundary of a cylindrical domain. Employing the special local structure of the Biot-Savart law in the CKY model, we prove that there exists a family of self-similar profiles, corresponding to different leading orders of the solution at the origin. Then we introduce a dynamic rescaling formation, which governs the evolution of the spatial profiles in the singular solutions of the two 1D models. Using the dynamic rescaling formulation, we demonstrate that the self-similar singularity for the two 1D models are actually stable.

For the 3D axisymmetric Euler equations, we prove that with suitable local analytic boundary conditions, there exist local analytic solutions to the self-similar equations. However, due to the 2D nature of the problem, we cannot extend the local analytic solutions to the whole domain as we did for the 1D CKY model. Using the dynamic rescaling formulation and initial data similar to that considered in [58], we reproduced the finite-time singularity scenario observed in [58], and demonstrated that this self-similar singularity scenario is actually stable. Then we consider another set of initial data with different leading order properties from that in [58], and observe that the solutions to 2D Boussinesq system develop finite-time singularity at multiple spatial scales. To be specific, the profiles in the singular solutions develop singularity themselves, and thus there is a smaller scale generated. Such a Euler singularity scenario has not been observed before in the literature.

We also study a family of 3D models for the 3D axisymmetric Euler and Navier-Stokes equations. The family of models are obtained by changing the amplitude of the convection terms in the axisymmetric Euler and Navier-Stokes equations in the cylindrical coordinates. This family of models share several regularity properties with the original Euler and Navier-Stokes equations, including an energy identity, a

Prodi-Serrin type nonblowup criterion and the partial regularity result. We observe that for small convection terms, the inviscid models develop finite-time singularity, and the solutions have self-similar structure with the center of the singular region travelling. For large convection terms, this self-similar singularity scenario is destroyed. Using the dynamic rescaling formulation, we also demonstrated that the travelling wave self-similar singularity scenario is stable for small convection. This result reveals the potential stabilizing effect of the convection terms.

In our future work, we seek to rigorously establish the existence of self-similar profiles for the 3D axisymmetric Euler equations. Due to the nonlocal nature of the Biot-Savart law in the self-similar equations,

$$\begin{aligned} W + c_l \xi \cdot \nabla W + V \cdot \nabla W &= \Theta_{\xi_1}, \\ (2 - c_l)\Theta + c_l \xi \cdot \nabla \Theta + V \cdot \nabla \Theta &= 0, \\ V &= \nabla^{\perp}(-\Delta)^{-1} W, \end{aligned}$$

we plan to use an iterative method to construct the self-similar profiles.

With the vorticity field W^n at the n-th step, one can construct V^n using

$$V^n = \nabla^{\perp}(-\Delta)^{-1} W^n.$$

With V^n, we can solve the following equation along characteristics to get Θ^{n+1},

$$(2 - cl)\Theta^{n+1} + c_l \xi \cdot \nabla \Theta^{n+1} + V^n \cdot \nabla \Theta^{n+1} = 0.$$

Then using Θ^{n+1}, we can get the updated W^{n+1} by solving the following equation

$$W^{n+1} + c_l \xi \cdot \nabla W^{n+1} + V^n \cdot \nabla W^{n+1} = \Theta_{\xi_1}^{n+1},$$

along characteristics.

By integrating along characteristics, W gains one order of regularity in each iteration step. Then by chosen suitable function space, one might get some compactness result for the iteration scheme, and prove the existence of a fixed point for the iteration, which is the solutions to the self-similar equations.

We also seek to rigorously prove the stability of the self-similar profiles. Recall that the axisymmetric Euler equations can be viewed as a perturbation to the 2D Boussinesq with the perturbation converging to zero exponentially fast in the dynamic rescaling formulation. Due to the existence of the perturbation terms, the

stability of the profiles is necessary for the singularity formation of the axisymmetric Euler equations. Our numerical results for the steady state of the discretized ODE system reveals that the self-similar profiles enjoy certain stability with respect to low frequency perturbations. And one needs to establish the stability of the self-similar profiles with high frequency perturbations in suitable function space.

BIBLIOGRAPHY

[1] K Appel and W Haken. “Proof of 4-color theorem”. In: *Discrete Mathematics* 16.2 (1976), pp. 179–180.

[2] MS Baouendi and C Goulaouic. “Singular nonlinear Cauchy problems”. In: *Journal of Differential Equations* 22.2 (1976), pp. 268–291.

[3] MS Baouendi and Ch Goulaouic. “Cauchy problems with characteristic initial hypersurface”. In: *Communications on Pure and Applied Mathematics* 26.4 (1973), pp. 455–475.

[4] GI Barenblatt. *Scaling, self-similarity, and intermediate asymptotics: dimensional analysis and intermediate asymptotics*. Vol. 14. Cambridge University Press, 1996.

[5] GI Barenblatt and YB Zel’Dovich. “Self-similar solutions as intermediate asymptotics”. In: *Annual Review of Fluid Mechanics* 4.1 (1972), pp. 285–312.

[6] JT Beale, T Kato, and A Majda. “Remarks on the breakdown of smooth solutions for the 3-D Euler equations”. In: *Communications in Mathematical Physics* 94.1 (1984), pp. 61–66.

[7] J Becker and G Grün. “The thin-film equation: recent advances and some new perspectives”. In: *Journal of Physics: Condensed Matter* 17.9 (2005), S291.

[8] Oluş N Boratav and Richard B Pelz. “Direct numerical simulation of transition to turbulence from a high-symmetry initial condition”. In: *Physics of Fluids (1994-present)* 6.8 (1994), pp. 2757–2784.

[9] L Caffarelli, R Kohn, and L Nirenberg. “Partial regularity of suitable weak solutions of the Navier-Stokes equations”. In: *Communications on Pure and Applied Mathematics* 35.6 (1982), pp. 771–831.

[10] RE Caflisch. “Singularity formation for complex solutions of the 3D incompressible Euler equations”. In: *Physica D: Nonlinear Phenomena* 67.1-3 (1993), pp. 1–18.

[11] D Chae. “Nonexistence of asymptotically self-similar singularities in the Euler and the Navier–Stokes equations”. In: *Mathematische Annalen* 338.2 (2007), pp. 435–449.

[12] D Chae. “Nonexistence of self-similar singularities for the 3D incompressible Euler equations”. In: *Communications in Mathematical Physics* 273.1 (2007), pp. 203–215.

[13] D Chae. “On the self-similar solutions of the 3D Euler and the related equations”. In: *Communications in Mathematical Physics* 305.2 (2011), pp. 333–349.

[14] K Choi, A Kiselev, and Y Yao. “Finite time blow up for a 1D model of 2D Boussinesq system”. In: *Comm. Math. Phys.* 334.3 (2015), pp. 1667–1679.

[15] K Choi et al. “On the Finite-time Blowup Of a 1D Model For the 3D Axisymmetric Euler Equations”. In: *arXiv preprint arXiv:1407.4776* (2014).

[16] EA Coddington and N Levinson. *Theory of ordinary differential equations*. Tata McGraw-Hill Education, 1955.

[17] P Constantin. “On the Euler equations of incompressible fluids”. In: *Bulletin of the American Mathematical Society* 44.4 (2007), pp. 603–621.

[18] P Constantin, C Fefferman, and AJ Majda. “Geometric constraints on potentially singular solutions for the 3D Euler equations”. In: *Communications in Partial Differential Equations* 21.3-4 (1996).

[19] J Deng, TY Hou, and X Yu. “Geometric properties and nonblowup of 3D incompressible Euler flow”. In: *Communications in Partial Difference Equations* 30.1-2 (2005), pp. 225–243.

[20] J Deng, TY Hou, and X Yu. “Improved geometric conditions for non-blowup of the 3D incompressible Euler equation”. In: *Communications in Partial Differential Equations* 31.2 (2006), pp. 293–306.

[21] S Dyachenko et al. “Optical turbulence: weak turbulence, condensates and collapsing filaments in the nonlinear Schrödinger equation”. In: *Physica D: Nonlinear Phenomena* 57.1 (1992), pp. 96–160.

[22] W E and CW Shu. “Small-scale structures in Boussinesq convection”. In: *Physics of Fluids (1994-present)* 6.1 (1994), pp. 49–58.

[23] J Eggers and MA Fontelos. “The role of self-similarity in singularities of partial differential equations”. In: *Nonlinearity* 22.1 (2009), R1.

[24] L Escauriaza, GA Seregin, and V Sverak. “L3,∞-solutions of the Navier-Stokes equations and backward uniqueness”. In: *Russian Mathematical Surveys* 58.2 (2003), p. 211.

[25] CL Fefferman and LA Seco. “Interval arithmetic in quantum mechanics”. In: *Applications of Interval Computations*. Springer, 1996, pp. 145–167.

[26] AB Ferrari. “On the blow-up of solutions of the 3D Euler equations in a bounded domain”. In: *Communications in Mathematical Physics* 155.2 (1993), pp. 277–294.

[27] G Fibich, N Gavish, and XP Wang. “Singular ring solutions of critical and supercritical nonlinear Schrödinger equations”. In: *Physica D: Nonlinear Phenomena* 231.1 (2007), pp. 55–86.

[28] GB Folland. *Introduction to Partial Differential Equations*. Princeton University Press, 1995.

[29] VA Galaktionov and JL Vázquez. "The problem of blow-up in nonlinear parabolic equations". In: *Discrete and continuous dynamical systems* 8.2 (2002), pp. 399–434.

[30] DJH Garling. *Inequalities: a journey into linear analysis*. Vol. 19. Cambridge University Press Cambridge, 2007.

[31] JD Gibbon. "The three-dimensional Euler equations: Where do we stand?" In: *Physica D: Nonlinear Phenomena* 237.14 (2008), pp. 1894–1904.

[32] Y Giga and RV Kohn. "Asymptotically self-similar blow-up of semilinear heat equations". In: *Communications on Pure and Applied Mathematics* 38.3 (1985), pp. 297–319.

[33] R Grauer and TC Sideris. "Numerical computation of 3D incompressible ideal fluids with swirl". In: *Physical Review Letters* 67.25 (1991), p. 3511.

[34] TC Hales. "A proof of the Kepler conjecture". In: *Annals of Mathematics* (2005), pp. 1065–1185.

[35] MA Herrero and JJL Velázquez. "Blow-up behaviour of one-dimensional semilinear parabolic equations". In: *Annales de l'IHP Analyse non linéaire*. Vol. 10. 2. 1993, pp. 131–189.

[36] TY Hou and Z Lei. "On the partial regularity of a 3D model of the Navier-Stokes equations". In: *Communications in Mathematical Physics* 287.2 (2009), pp. 589–612.

[37] TY Hou and Z Lei. "On the stabilizing effect of convection in three-dimensional incompressible flows". In: *Communications on Pure and Applied Mathematics* 62.4 (2009), pp. 501–564.

[38] TY Hou and C Li. "Dynamic stability of the three-dimensional axisymmetric Navier-Stokes equations with swirl". In: *Communications on Pure and Applied Mathematics* 61.5 (2008), pp. 661–697.

[39] TY Hou and R Li. "Dynamic depletion of vortex stretching and non-blowup of the 3D incompressible Euler equations". In: *Journal of Nonlinear Science* 16.6 (2006), pp. 639–664.

[40] TY Hou and P Liu. "Self-similar singularity of a 1D model for the 3D axisymmetric Euler equations". In: *Research in the Mathematical Sciences* 2.1 (2015), pp. 1–26.

[41] TY Hou and G Luo. "On the finite-time blowup of a 1D model for the 3D incompressible Euler equations". In: *arXiv preprint arXiv:1311.2613* (2013).

[42] TY Hou, Z Shi, and S Wang. "On singularity formation of a 3D model for incompressible Navier-Stokes equations". In: *Advances in Mathematics* 230.2 (2012), pp. 607–641.

[43] TY Hou et al. “On finite time singularity and global regularity of an axisymmetric model for the 3D Euler equations”. In: *Archive for Rational Mechanics and Analysis* 212.2 (2014), pp. 683–706.

[44] T Kato. “Nonstationary flows of viscous and ideal fluids in R 3”. In: *Journal of functional Analysis* 9.3 (1972), pp. 296–305.

[45] RB Kearfott and V Kreinovich. *Applications of interval computations*. Vol. 3. Kluwer Academic Dordrecht, 1996.

[46] RM Kerr. “Bounds for Euler from vorticity moments and line divergence”. In: *Journal of Fluid Mechanics* 729 (2013), R2.

[47] RM Kerr. “Evidence for a singularity of the three-dimensional, incompressible Euler equations”. In: *Physics of Fluids A: Fluid Dynamics* 5.7 (1993), pp. 1725–1746.

[48] A Kiselev and V Sverak. “Small scale creation for solutions of the incompressible two dimensional Euler equation”. In: *Annals of Mathematics* 180 (2014), pp. 1205–1220.

[49] H Koch and D Tataru. “Well-posedness for the Navier-Stokes equations”. In: *Advances in Mathematics* 157.1 (2001), pp. 22–35.

[50] S Kowalevski. “Zur Theorie der Partiellen Differentialgleichungen”. In: (1874).

[51] MJ Landman et al. “Rate of blowup for solutions of the nonlinear Schrödinger equation at critical dimension”. In: *Physical Review A* 38.8 (1988), p. 3837.

[52] M Landman et al. “Stability of isotropic self-similar dynamics for scalar-wave collapse”. In: *Physical Review A* 46.12 (1992), p. 7869.

[53] OE Lanford III. “A computer-assisted proof of the Feigenbaum conjectures”. In: *Bulletin of the American Mathematical Society* 6.3 (1982), pp. 427–434.

[54] BJ LeMesurier et al. “Focusing and multi-focusing solutions of the nonlinear Schrödinger equation”. In: *Physica D: Nonlinear Phenomena* 31.1 (1988), pp. 78–102.

[55] J Leray. “Sur le mouvement d’un liquide visqueux emplissant l’espace”. In: *Acta mathematica* 63.1 (1934), pp. 193–248.

[56] RJ LeVeque. *Finite difference methods for ordinary and partial differential equations: steady-state and time-dependent problems*. Vol. 98. Siam, 2007.

[57] F Lin. “A new proof of the Caffarelli-Kohn-Nirenberg theorem”. In: *Communications on Pure and Applied Mathematics* 51.3 (1998), pp. 241–257.

[58] G Luo and TY Hou. “Toward the finite-time blowup of the 3D incompressible Euler equations: a numerical investigation”. In: *SIAM Multiscale Modeling and Simulation* 12.4 (2014), pp. 1722–1776.

[59] AJ Majda and AL Bertozzi. *Vorticity and incompressible flow*. Vol. 27. Cambridge University Press, 2002.

[60] DW McLaughlin et al. “Focusing singularity of the cubic Schrödinger equation”. In: *Physical Review A* 34.2 (1986), p. 1200.

[61] F Merle and P Raphael. “On a sharp lower bound on the blow-up rate for the L^2 critical nonlinear Schrödinger equation”. In: *Journal of the American Mathematical Society* 19.1 (2006), pp. 37–90.

[62] F Merle and P Raphael. “On universality of blow-up profile for L^2 critical nonlinear Schrödinger equation”. In: *Inventiones mathematicae* 156.3 (2004), pp. 565–672.

[63] F Merle and H Zaag. “Optimal estimates for blowup rate and behavior for nonlinear heat equations”. In: *Communications on pure and applied mathematics* 51.2 (1998), pp. 139–196.

[64] GC Papanicolaou et al. “The focusing singularity of the Davey-Stewartson equations for gravity-capillary surface waves”. In: *Physica D: Nonlinear Phenomena* 72.1 (1994), pp. 61–86.

[65] G Perelman. “On the formation of singularities in solutions of the critical nonlinear Schrödinger equation”. In: *Annales Henri Poincaré*. Vol. 2. 4. Springer. 2001, pp. 605–673.

[66] L Perko. *Differential equations and dynamical systems*. Vol. 7. Springer Science & Business Media, 2001.

[67] G Prodi. “Un teorema di unicita per le equazioni di Navier-Stokes”. In: *Annali di Matematica pura ed applicata* 48.1 (1959), pp. 173–182.

[68] A Pumir and ED Siggia. “Development of singular solutions to the axisymmetric Euler equations”. In: *Physics of Fluids A: Fluid Dynamics (1989-1993)* 4.7 (1992), pp. 1472–1491.

[69] V Scheffer. “Turbulence and Hausdorff dimension”. In: *Turbulence and Navier Stokes Equations*. Springer, 1976, pp. 174–183.

[70] LI Sedov. *Similarity and dimensional methods in mechanics*. CRC press, 1993.

[71] J Serrin. “The initial value problem for the Navier-Stokes equations”. In: *Nonlinear problems* 9 (1963), 69ff.

[72] M Siegel and RE Caflisch. “Calculation of complex singular solutions to the 3D incompressible Euler equations”. In: *Physica D: Nonlinear Phenomena* 238.23 (2009), pp. 2368–2379.

[73] T Tao. “Finite time blowup for an averaged three-dimensional Navier-Stokes equation”. In: *Journal of the American Mathematical Society* 29.3 (2016), pp. 601–674.

[74] T Tao. *Structure and randomness: pages from year one of a mathematical blog*. American Mathematical Soc.

[75] TP Witelski and AJ Bernoff. “Dynamics of three-dimensional thin film rupture”. In: *Physica D: Nonlinear Phenomena* 147.1 (2000), pp. 155–176.

[76] WW Zhang and JR Lister. “Similarity solutions for van der Waals rupture of a thin film on a solid substrate”. In: *Physics of Fluids (1994-present)* 11.9 (1999), pp. 2454–2462.

[77] D Zuras et al. “IEEE Standard for Floating-Point Arithmetic”. In: *IEEE Std 754-2008* (2008), pp. 1–70.